University of Liège - Faculty of Applied Sciences

Graduation studies conducted for obtaining a Master's degree in Civil Engineering

Modelling of the Shear Behaviour of Coupling Beams with Fibre Reinforced Concrete

Author:
Rémy Lobet

Jury Members:
Boyan Mihaylov
Vincent Denoël
Thomas Gernay
Luc Demortier

Academic year 2016-2017

Abstract

Coupling beams are essential for transmitting shear forces from a shear wall to another in order to create a coupled-wall system. This system is used to resist both monotonic and cyclic lateral loads due to wind or earthquake. When coupling beams fail, the whole system fails and therefore, their behaviour needs to be analysed in order to design safe structures. In general, such beams have a low span-to-depth ratio and undergo a shear failure. Since these beams are subjected to high shear forces, fibre reinforced concrete can be used to enhance their strength. This thesis focuses on the shear behaviour of coupling beams made of fibre reinforced concrete.

The aim of this thesis is to propose an extension of the 3PKT model developed by Mihaylov et al. (2015) in order to predict the shear behaviour of reinforced concrete deep beams. The 3PKT theory uses 3 degrees of freedom to find the shear strength of members made of conventional concrete. In order to find the total force-displacement response of the member, the extension of the 2PKT for fibre reinforced concrete deep beam proposed by Tvrznikova (2017) is used. This model captures the effect of steel fibres embedded in concrete in three ways: 1)tension in the fibres bridging cracks; 2)enhanced ductility of the critical compressed zones in deep beams and 3)tension stiffening effect on the longitudinal reinforcement. The extension of this model to account for coupling beams provides different modifications: 1)softening of concrete in highly compressed zones; 2)averaging of the crack width and 3)effect of bar pull-out. To account for these effects, existing models from the literature are studied and used. Each model is implemented in a Matlab code.

An additional method based on non-linear finite element analysis is performed in order to be able to compare the extended 3PKT model to results from a more complex and general method. General assumptions are made in order to find accurate results. It is shown that the shear strength estimated by this method matches closely measured valued from experimental data.

The extended 3PKT model is validated against a database of tests performed on FRC coupling beams collected from the literature. It is shown that the predicted shear strengths agree well with values found from experimental studies. It is also shown that while FEM analysis provides very accurate results, they are as accurate as results found from extended 3PKT analysis although the latter is much less time consuming. The validated model is then used to perform a parametric study which analyses the effects of the span-to-depth (a/d) ratio, longitudinal reinforcement ratio, fibre volume ratio, concrete compressive strength, transverse reinforcement ratio and size effect.

Résumé

Les poutres de couplage sont essentielles pour transmettre les efforts de cisaillement d'un mur de cisaillement à un autre créant ainsi un système de murs couplés. Ce système est utilisé pour résister aux charges monotones et cycliques du vent ou bien des séismes. Quand ces poutres de couplage cèdent, tout le système s'effondre et donc il est important d'analyser leur comportement pour dimensionner des structures de manière adéquate. En général, de telles poutres ont un rapport longueur sur hauteur assez faible et elles subissent une rupture en cisaillement. Comme ces poutres sont soumises à d'intenses forces, le béton fibré peut être utilisé pour augmenter leur résistance. Cette thèse se concentre sur l'étude du comportement en cisaillement de poutres de couplage faites de béton fibré.

Le but de cette thèse est de proposer une extension au modèle 3PKT développé par Mihaylov et al. (2015) qui permet de prédire le comportement en cisaillement de poutres-voiles en béton armé. La méthode du 3PKT utilise 3 degrés de liberté permettant de trouver la résistance en cisaillement de membrures faites de béton conventionnel. Dans le but de trouver la réponse complète de type force-déplacement de la poutre, une extension au modèle 2PKT permettant de prendre en compte le béton fibré (Tvrznikova, 2017) est utilisée. Ce modèle capture l'effet des fibres d'acier de trois manières: 1)la tension dans les fibres qui lient les fissures du béton; 2)une ductilité améliorée dans les zones critiques hautement comprimées et 3)l'effet de raidissement en tension sur les armatures longitudinales. L'extension de ce modèle permettant de prendre en compte les poutres de couplage se fait en plusieurs modifications: 1)adoucissement du béton dans les zones hautement comprimées; 2)prise en compte d'une largeur de fissure moyenne et 3)l'effet du glissement des armatures longitudinales dans le béton. Pour prendre en compte ces effets, des modèles existants sélectionnés dans la littérature scientifique sont étudiés et utilisés. Un code Matlab est développé à chaque étape.

Une méthode additionnelle basée sur une étude par éléments finis non linéaire est utilisée pour apporté une méthode de comparaison supplémentaire plus complexe et générale à l'extension du 3PKT. Des hypothèses générales sont énoncées. Il résulte de l'analyse par éléments finis que la résistance en cisaillement des éléments étudiés se rapproche assez bien des valeurs expérimentales.

L'extension du modèle 3PKT est ensuite validée en comparaison avec les données expérimentales. Il est montré que les valeurs de résistance en cisaillement sont proches des valeurs expérimentales. Il est également montré que tandis que l'analyse par éléments finis produit des résultats assez précis, l'extension du modèle 3PKT fournit des résultats tout aussi précis mais en un moindre temps. Le modèle validé est ensuite utilisé pour faire une étude paramétrique qui analyse les effets du rapport longueur sur hauteur (a/d), de l'armature longitudinale, du volume de fibres, de la résistance en compression du béton, des étriers et enfin de l'effet d'échelle.

Acknowledgements

First of all, I would like to thank all the members of the jury and everyone who will take their time to read this thesis.

I would like to thank Professor Boyan Mihaylov for his great guidance and advice throughout the development of this thesis. He provided tremendous help through regular consultations and questions during the whole semester. Working with him helped me developed a critical mind and helped me question myself. This experience was truly rewarding. I owe him a lot.

Moreover, I would like to give special thanks to my office colleagues Jian Liu, Nikola Tatar and Renaud Franssen who always answered my questions. It was a real pleasure to work in such a friendly environment.

I would like to thank Mr. Luc Demortier as well who helped me question my results in term of design procedure.

Finally, I would like to thank my family and friends who were very supportive during this semester.

Contents

List of Figures

List of Tables

List of annotations

2PKT	Two-parameter kinematic theory
3PKT	Three-parameter kinematic theory
a	Shear span
a/d	Span-to-depth ratio
a_g	Maximum aggregate size
A_s	Area of longitudinal reinforcement bars
$A_{c,eff}$	Area of concrete providing tension stiffening for bottom reinforcement
b	Width of cross section
c	Coefficient for tension stiffening effect of concrete or mortar
C	Compression force in section with maximum moment
c_f	Coefficient to consider the effect of steel fibres on tension stiffening
CLZ	Critical loading zone
CMOD	Crack mouth opening displacement
CTOD	Crack top opening displacement
d	Effective depth of section
d_1	Effective depth of section with respect to bottom longitudinal reinforcement
d_2	Effective depth of section with respect to top longitudinal reinforcement
d_b	diameter of longitudinal bars
DEM	Diverse Embedment Model
d_f	fibre diameter
DOF	Degree of freedom
dx	Element length for FEM analysis of bar pull-out
E_c	Elastic modulus of concrete
E_s	Elastic modulus of steel
F	Force vector
f'_c	Concrete cylinder strength
f_c	Local stress of concrete
$f_{c,TS}$	Tensile stress due to tension stiffening
$f_{c,soft}$	Tensile stress in concrete due to tension softening
f_{con}	Tensile stress in concrete
F_{con}	Tensile force of concrete
f_{cr}	Cracking strength of concrete or mortar matrix
f_{ct}	Tensile stress due to concrete/mortar tension softening at given crack width
f_{eh}	Tensile stress due to mechanical anchorage effect of hook-ended steel fibres
FEM	Finite Element Method
f_f	Tensile stress at crack due to steel fibres
F_f	Force provided by the fibres
$f_{f,avg}$	Average tensile stress in fibres with crack averaging
f_{fib}	Tensile stress in fibres
F_{fib}	Tensile force of fibres
f_{R1k}	Stress at serviceability limit state
f_{R3k}	Stress at ultimate limit state
FRC	Fibre reinforced concrete
f_{reb}	Tensile stress in reinforcing bar
F_{reb}	Tensile force of reinforcing bar
f_{SFRC}	Total tensile stress of SFRC member
f_{st}	Tensile stress due to frictional bond behaviour of steel fibres

f_t	Tensile strength of concrete
f_{uf}	Tensile strength of fibres
f_{yv}	Yielding strength of stirrups
h	Height of the member
HSC	High strength concrete
k	Factor influencing post-peak decay
K	Stiffness matrix of bar pull-out system
K_{el}	Elastic stiffness matrix for bar elongation
$k_{el,i}$	Elastic stiffness of element i
K_b	Stiffness matrix for bond behaviour between rebar and concrete
$k_{b,i}$	Bond stiffness of node i
l_0	Length of heavily cracked zone at bottom of critical diagonal crack
l_b	Bond length
l_{b1e}	Effective loaded length of the critical loading zone
l_f	Fibre length
l_i	Inner length of hook-ended fibres
l_k	Length of dowels provided by bottom longitudinal reinforcement
l_p	Length between crushed zone and opposite layer of longitudinal reinforcement
l_t	Length of bottom reinforcement within the cracked part of the shear span
m	Bending moment ratio
M	Moment applied to both sides of a symmetric coupling beam
M_1	Absolute value of moment causing tension in bottom reinforcement
M_2	Absolute value of moment causing tension in top reinforcement
n	Curve fitting factor
M_b	Bond parameter
n_b	Number of bottom longitudinal bars
n_{b1}	Number of bottom longitudinal bars for 3PKT
n_{b2}	Number of top longitudinal bars
NSC	Normal strength concrete
P	Applied concentrated load
RC	Reinforced concrete
RI_V	Fibre reinforcing index based on fibre volume ratio
s	Slip displacement
s_1	Bar slip at maximum bond stress between rebar and concrete
s_2	Bar slip before pull-out failure
s_3	Bar slip at the beginning of residual bond stress between rebar and concrete
s_{cr}	Distance between the radial cracks along bottom longitudinal reinforcement
$SDEM$	Simplified Diverse Embedment Model
s_{eh}	Slip at maximum tensile force due to mechanical anchorage of a hook-ended fibre
s_f	Slip at frictional bond strength for a straight fibre
$SFRC$	Steel fibre reinforced concrete
T	Tensile force in bottom reinforcement
T_f	Tensile force in bottom reinforcement including fibre action
V	Shear force
u_1	Maximum bond stress between rebar and concrete
u_f	Residual bond stress between rebar and concrete
V_{3PKT}	Shear strength estimated by the extended 3PKT
V_{ci}	Shear resisted by aggregate interlock
V_{CLZ}	Shear resisted by the critical loading zone

V_{exp}	Measured shear strength
V_f	Fibre volume ratio
V_F	Shear resisted by fibres
V_s	Shear resisted by stirrups
w_{cr}	Average crack width
$w_{cr,T}$	Width of the crack applied in the SDEM to define tensile stress in fibres
w_m	Crack width halfway along the crack
α	Angle of the line extending from inner edge of support plate to far edge of tributary area of loading plate responsible for shear force in deep beams or angle of diagonal in coupling beams
α_1	Angle of critical diagonal crack
α_f	Fibre orientation factor
α_p	Angle of rotation due to pull-out
β	Angle between the force provided by the fibres F_f and the vertical component of the force V_F
β_{eh}	Coefficient to consider the effect of fibre slip on the longer embedment side on frictional behaviour
β_f	Coefficient to consider the effect of fibre slip on the monger embedment side on mechanical anchorage effect
Δ	Total transverse displacement
Δ_c	Transverse vertical displacement of the critical loading zone
Δ^p	Displacement vector
Δ_t	Deflection of the shear span due to elongation of bottom longitudinal reinforcement
ϵ'_c	Strain of concrete at peak strength
ϵ_{c0}	Strain at peak for plain concrete
ϵ_{cf}	Steain at peak for FRC
ϵ_{max}	Maximum diagonal compressive strain in the critical loading zone
$\epsilon_{t,avg}$	Average strain in longitudinal reinforcement
$\epsilon_{t1,avg}$	Average strain in bottom longitudinal reinforcement
$\epsilon_{t2,avg}$	Average strain in top longitudinal reinforcement
ϵ_v	Strain in transverse reinforcement in critical diagonal crack halfway along the crack
ϕ_l	Diameter of longitudinal reinforcement bars
ϕ_v	Diameter of stirrups
θ	Angle of diagonal cracks in a uniform stress field
θ_d	Drift angle
ρ_l	Ratio of longitudinal reinforcement
ρ_{l1}	Ratio of bottom longitudinal reinforcement
ρ_{l2}	Ratio of top longitudinal reinforcement
ρ_v	Ratio of transverse reinforcement
σ_{avg}	Average diagonal stress in critical loading zone
σ_v	Stress in transverse reinforcement
$\tau_{eh,max}$	Pull-out strength due to mechanical anchorage of hook-ended fibre
$\tau_{f,max}$	Frictional bond strength
ν_{ci}	Aggregate interlock shear stress
Ω	Area under stress-strain curve
Ω_m	Area under stress-crack width curve between 0 and $w = w_m$

1 Introduction

1.1 General information

The aim of coupling beams in high-rise buildings is to connect shear walls which resist, in addition to gravity loads, lateral loads induced by seismic events or wind loading. When subjected to lateral ground acceleration the loads need to be transferred to the foundation system through the coupled-wall system. Therefore, the link between those walls needs to be strong enough to resist such effects because it will be a critical zone of the system. Indeed, the connecting zone will generally be the first one to fail and it will lead to the collapse of the building if the transfer of forces can no longer be ensured. Since then, it is also necessary for the system to be able to redistribute forces even when one or more coupling beams fail. The extent of such force redistribution depends on displacement capacity and post-peak behaviour of the transfer beam which is in this case the coupling beam (Mihaylov et al., 2015). The deformation of coupled wall systems is shown in Figure 1. It can be seen that the coupling beams suffer from double curvature due to lateral loading (seismic loading in this example).

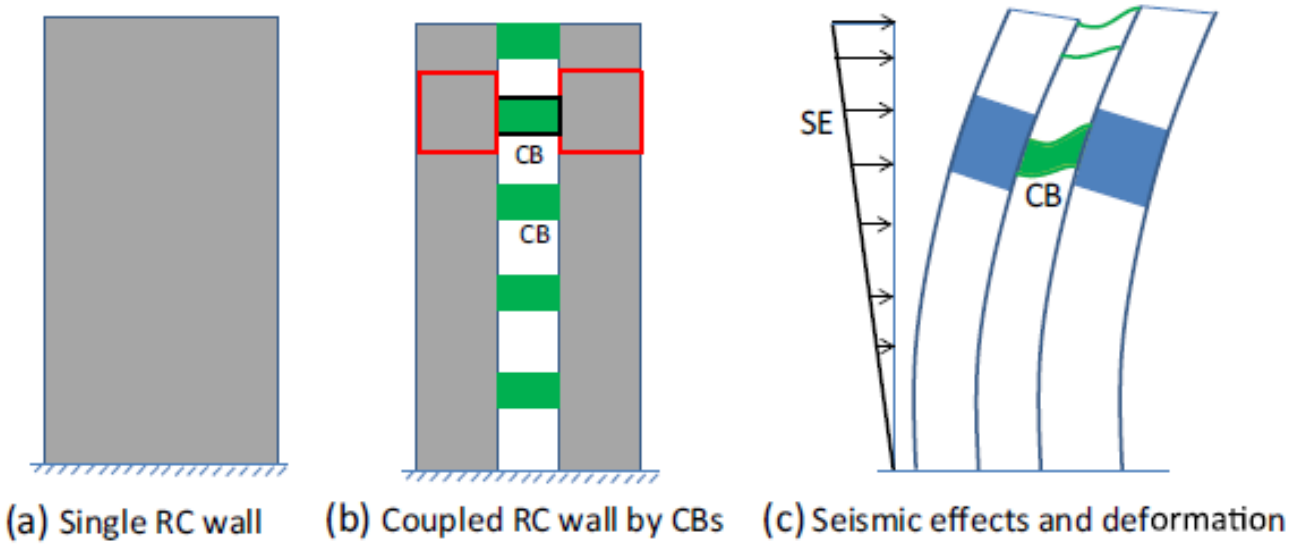

Figure 1: Reinforce concrete (RC) wall, Coupled RC wall by coupling beams (CB) and deformation due to seismic effects (SE) (Gaochuang et al., 2016)

Coupling beams are used typically in high-rise buildings to connect shear walls which usually surround elevator shafts. These beams must therefore be long enough to leave space for a lift door. In spite of this length, coupling beams must have a rather large depth in order to be able to transfer high loads due to external loads. Therefore, they are characterised by a relatively small span-to-depth ratio. In general, this ratio can go up to 2.5 or 3. Such proportions imply that the mechanism of load resistance is not the same as for slender beams for which the plane sections remain plane assumption is valid. This hypothesis first demonstrated by Robert Hooke in 1678 is the basis for the flexural and axial load procedures of general codes such as ACI (ACI Committee 318, 2011). This assumption can be taken into account for the analysis of the effects of shear when it is valid. However, in the case of coupling beams, since the span-to-depth ratio is small, plane sections do not remain plane. While shear strains become dominant, the pattern of deformations becomes more complex and needs to be analysed with a different approach (Mihaylov et al., 2013). This effect is shown in Figure 2 for deep beams where the same conclusions can be considered for coupling beams since their span-to-depth ratio is equivalent to deep beams.

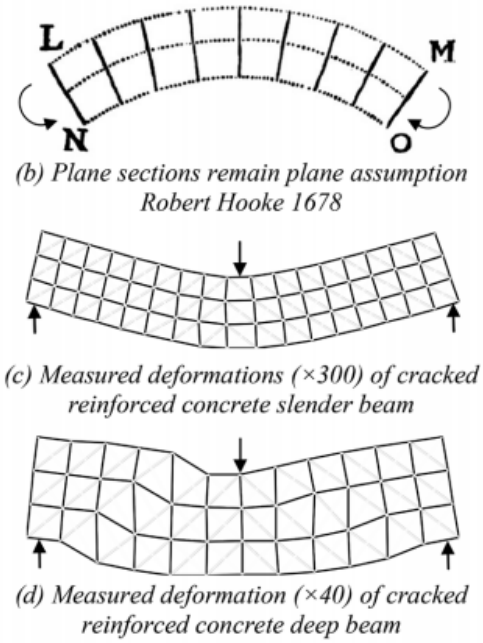

Figure 2: Deformation patterns of slender beams and deep beams (Mihaylov et al., 2013)

In coupling beams, a relatively important portion of the shear is carried by strut action, where compressive stresses flow directly from the load to the support (Mihaylov et al., 2013). Most particularly in this case, the force is transferred from one corner of the coupling beam to the opposite and therefore, strut-and-tie models were developed. However, these models are not able to predict the shear behaviour of coupling beams because of the large amount of parameters that influence the shear behaviour. Mihaylov et al. (2013) proposed a model that could take into account more parameters. The model is called 2-Parameter Kinematic Theory (2PKT). This model works with 2 degrees of freedom and uses equations of equilibrium, compatibility and stress-strain relationships. An improvement of the model was proposed by Mihaylov et al. (2015) in order to account for more parameters. This model which is called 3PKT uses 3 degrees of freedom and the same equations as for the 2PKT. This model is useful in the case of coupling beams since it can deal with double curvature deformations while the 2PKT can only consider members under single curvature. However, 2PKT and 3PKT models only give information about the ultimate shear strength of the member and cannot generate the whole behaviour of the latter. Hence, the extended 2PKT was developed by Mihaylov et al. (2015) in order to obtain the whole force-displacement curve. This model, based on the 2PKT is able to predict the post-peak behaviour of the beam which is important for the safety of structures because the ability of the structures to remain standing depends on their capacity to redistribute forces (Mihaylov et al., 2015). However, in the case of coupling beams, the 2PKT method is not adapted for the reasons mentioned above and an extent to the extended 2PKT which involves 3 degrees of freedom needs to be derived.

Moreover, the post-peak behaviour and the displacement capacity can be enhanced with the addition of fibres in the concrete mixture. The utilisation of fibres (steel for example) provides higher ductility to concrete and improves the post-peak behaviour. Fibres also have other positive impacts on concrete such as higher tensile strength, reduced crack width and crack spacing. The main goal of fibres is not to increase the strength of concrete since there are other cheaper ways of doing so. The real contribution of fibres is to increase the toughness of concrete under any type of loading, that is to increase the strain at peak load and provide greater energy absorption in the post-peak domain (Van Chanh, 2004). The effect of the fibres vary on the material used, their shape, fibre volume ratio, fibre aspect ratio and fibre

length. Materials used can be steel, several polymers or glass while their shape can be straight, hook-ended, crimped and flattened-end. In this study, only steel fibres are considered and their shape are either straight or hook-ended.

1.2 Reinforcement layout in coupling beams

In coupling beams, there are several ways to place the reinforcement. The first method is the most common and is called the conventional layout. As shown in Figure 3, this method consists of heavily reinforced and well anchored top and bottom layers with the help of stirrups placed on the whole length of the beam. Another method proposed by Paulay and Binney (1974) is also shown in Figure 3. This layout is called diagonally reinforced coupling beam. Experimental studies proved that this kind of coupling beam was able to resist higher shear loads and larger deformations as well as to dissipate more earthquake energy compared to conventional ones (Shiu et al., 1978). However, this method leads to a high congestion of reinforcement in the coupling beam and becomes worse when the depth-width ratio increases. In order to solve the problem, fibre concrete was used to replace partially the reinforcement of coupling beams and resulted in an equal distribution of forces and higher energy dissipation than conventional coupling beams as shown from experiments by Chaallal et al. (1996). It was also reported that fibre reinforced concrete can reduce the required area of diagonal reinforcement by 70 % relative to a code based design (Lequesne et al., 2012). Moreover, steel fibres can significantly reduce the amount of shear reinforcement while maintaining the required shear resistance (Casanova et al., 1997).

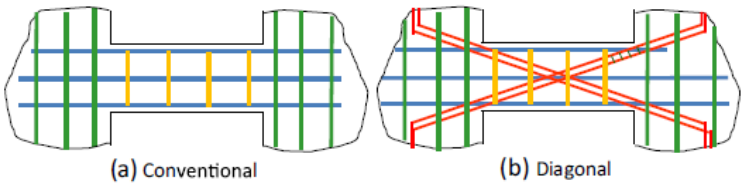

Figure 3: Reinforcement layouts (Gaochuang et al., 2016)

1.3 Scope of the thesis

This thesis is a continuation of the work developed by Mihaylov et al. (2015) and by Tvrznikova (2017). The 2PKT and 3PKT methods are capable of predicting shear resistance and deformation patterns at ultimate load for reinforced concrete members. An extension was applied to the 2PKT by Mihaylov et al. (2015) in order to find the pre- and post-peak behaviour of beams subjected to high shear forces. This extension is called the extended 2PKT. Later, this extension allowed to consider steel fibre reinforced concrete thanks to the work of Tvrznikova (2017).

As mentioned above, coupling beams are subjected to double curvature and the extended 2PKT which is based on the 2PKT is not capable of accounting for such a deformed shape. The aim of this thesis is to modify the extended 2PKT by using equations derived in the 3PKT model and to account for the effect of steel fibres. In addition, improvements to the Matlab code developed by Tvrznikova are provided.

First of all, the extended 2PKT for FRC (Tvrznikova, 2017) and 3PKT (Mihaylov et al., 2015) are analysed. Then, modifications brought to the extended 2PKT for FRC model to account for the effect of double curvature in coupling beams are explained. Additional modifications are then proposed and implemented into the general code. The model is validated against experimental data provided by researchers and non-linear finite element analysis performed with the program VecTor2 developed at the university of Toronto, Canada. Afterwards, a parametric study is performed to analyse the effects of the transverse and

longitudinal reinforcement, fibre volume ratio, size effect, concrete compressive strength and span-to-depth ratio. Finally, a discussion is provided with propositions for future development.

1.4 Thesis outline

The thesis consists of 6 chapters, including Chapter 1.

Chapter 2 provides general information about relevant topics used in this thesis. These include an overview of the utilisation of fibres in concrete and current code specifications for the design of steel fibre reinforced concrete (SFRC) members. Chapter 2 gives a short list of different approaches that can be used for the analysis of coupling beams. This chapter also provides information about test setups used for experiments on coupling beams.

Chapter 3 explains two general methods of analysis. First, the extended 2PKT is presented and its modifications to account for the effect of fibres on deep beams are explained. Then, the 3PKT theory is explained.

Chapter 4 develops an extension of the 3PKT model in order to account for the effect of fibres in coupling beams. Proposed modifications are explained and results on the load-displacement curves are shown. The impact of each modification is evaluated.

Chapter 5 consists of a non-linear finite element study. It consists of modelling tests found in the literature and comparing the results to experimental data and proposed extended 3PKT analysis.

Chapter 6 provides a validation of the proposed model and a parametric study of the latter. Several parameters are evaluated such as the span-to-depth ratio, the fibre volume ratio or the transverse reinforcement ratio.

Chapter 7 gives a general conclusion of the thesis and a discussion of the results.

2 Observed behaviour of FRC coupling beams

2.1 Fibre reinforced concrete (FRC)

Fibre reinforced concrete consists of a mixture of a cement matrix and discrete discontinuous fibres. The material used for fibres varies from steel to polymers or even glass. Thousands of small fibres are randomly dispersed in the matrix to improve concrete properties. The role of the randomly distributed fibres is to bridge across the cracks that develop in the concrete, providing post-cracking ductility (Sahoo et al., 2015). Historically, the use of fibres in the cement matrix is not totally new since the first reported construction which used a composite material goes back to approximately 3500 years ago near present-day Baghdad where a 57 m high hill was built with sun-baked bricks reinforced with straw (Bentur and Mindess, 1990). The first widely manufactured composite in modern time was asbestos cement developed in about 1900 (Bentur and Mindess, 1990). However, primarily due to health hazard associated with asbestos, alternate fibres were introduced throughout the 1960s and 1970s (ACI Committee 544, 1982). However, research focused on structural response of FRC has mainly developed over the last 15 years (Di Prisco et al., 2013). Therefore, there is a lack of information in international building codes for structural design and a lack of guidelines which lead the practitioners to hardly accept to use of FRC only based on voluntary guidelines or research papers (Di Prisco et al., 2013).

2.1.1 Properties of FRC

Tensile behaviour

The first important property enhancement of FRC compared to reinforced concrete (RC) in the tensile strength. Fibres are able to bridge cracks in the matrix and therefore transmit stresses across the cracks. This will result in a reduction of crack width. Moreover, with an increasing fibre content, the post-peak behaviour is enhanced due to increased toughness. As a consequence, the material becomes more ductile as opposed to the very brittle behaviour of concrete. Depending on fibre orientation, SFRC members in uniaxial tension exhibit either a softening or hardening post-peak behaviour. This effect was observed by Susetyo (2009) who described 3 different regions of the stress-strain curves obtained from tests (see Figure 4). The three regions are named as follows:

- I - Linear elastic region
- II - Strain hardening region
- III - Tension softening region

Region I is the case in which no cracking has occurred and the stiffness of the concrete can be assumed to be constant. In region II, although the concrete can sustain additional stresses, a significant decrease of the stiffness is observed indicating a processing damage in the matrix. This region only appears if the fibre volume ratio is higher than the critical fibre volume ratio. Finally, region III occurs after all cracks have been developed. The deformation is localised in one crack and the stiffness gradually decreases (Susetyo, 2009). The critical fibre volume ratio is the volume of fibres which after matrix cracking will carry the load that the composite material sustained before cracking (Newman and Choo, 2003). There are 3 different fibre volume contents to consider:

- $v_{f,min}$ - Minimum fibre volume fraction
- $v_{f,crit}$ - Critical fibre volume fraction
- $v_{f,max}$ - Maximum fibre volume fraction

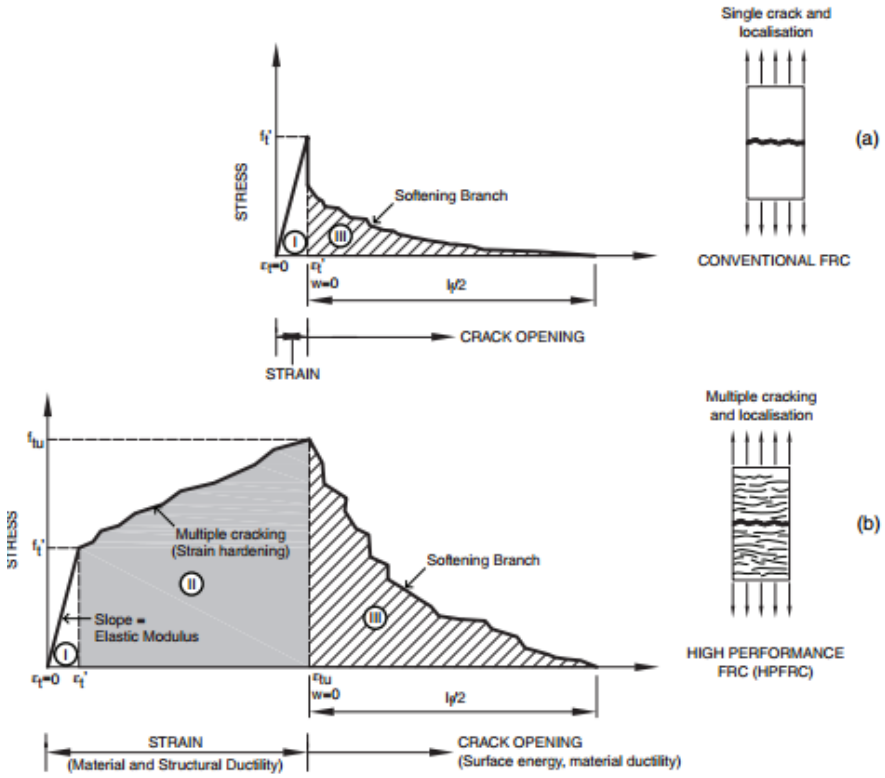

Figure 4: Comparison of typical tensile stress-strain response of fibre reinforced concrete containing (a) low fibre volume content (b) high fibre volume content (Susetyo, 2009)

The minimum fibre volume fraction stands for the amount of fibres necessary to increase the strength of the matrix. Indeed, if there are not enough fibres, stresses on a composite may be high enough to break the fibres. When broken, fibres will carry no load and can be regarded as several aligned holes. This effect will result in a weaker matrix than if it was without fibres. The critical fibre volume fraction is therefore the volume below which the fibres weaken the material (Shah et al., 2012). The maximum fibre volume fraction is a practical, observed limit above which composite properties deteriorate and/or porosity increases drastically.

To determine the tension behaviour of FRC, uniaxial tests are not advised for standard testing due to difficulty to carry out the tests. Instead, three- or four-point bending tests are performed. Then, a reverse analysis is carried out to derive the relationship between tensile stress and crack width. An example is shown in Figure 5 (Di Prisco et al., 2013). On the vertical axis is the applied force and on the horizontal axis is the crack mouth opening displacement (CMOD) measured at a notch cut in the specimen. CMOD is thus defined as the opening of the notch at the bottom face of the beam for three-point bending tests. The bold black curve is for a FRC specimen and the grey curve is for plain concrete. When using four-point loading, the measured parameter is the crack top opening displacement (CTOD).

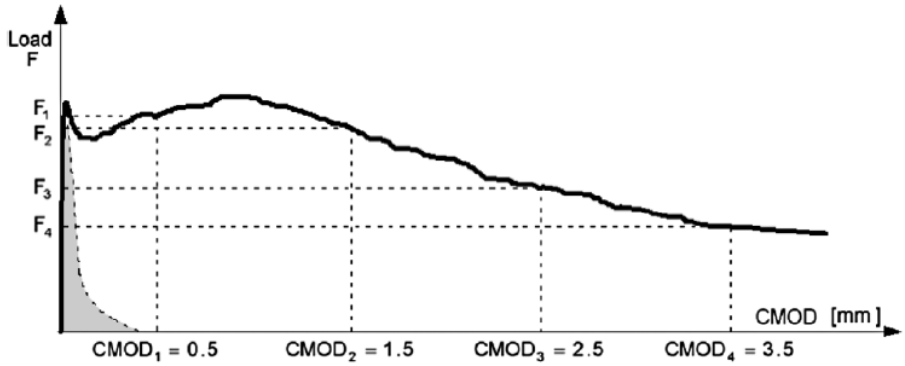

Figure 5: Typical load F-CMOD curve for plain concrete and FRC from fib MC 2010 (Di Prisco et al., 2013)

Based on the results from Figure 5, FRC can be classified. From this curve, 2 important post-cracking stresses are taken: f_{R1k} at $CMOD = 0.5\ mm$ which characterises the material behaviour at serviceability limit state and f_{R3k} at $CMOD = 2.5\ mm$ at ultimate limit state. Two parameters are then used to classify the material: one number denoting the f_{R1k} class and a letter denoting the ratio $\frac{f_{R3k}}{f_{R1k}}$. f_{R1k} strength values are taken from the following classes: $[1.0, 1.5, 2.0, 2.5, 3.0, 4.0, 5.0, 6.0, 7.0, 8.0]$ whereas the letter is derived from the following values:

- a. if $0.5 < \frac{f_{R3k}}{f_{R1k}} \leq 0.7$
- b. if $0.7 < \frac{f_{R3k}}{f_{R1k}} \leq 0.9$
- c. if $0.9 < \frac{f_{R3k}}{f_{R1k}} \leq 1.1$
- d. if $1.1 < \frac{f_{R3k}}{f_{R1k}} \leq 1.3$
- e. if $1.3 < \frac{f_{R3k}}{f_{R1k}}$

Compressive behaviour

The compressive behaviour of FRC is not considered in the fib Model Code 2010. However, it is stated that unless a high volume of fibre is added to the concrete mixture, fibres do not have a significant effect on the compressive strength of concrete. Nonetheless, for fibre volume ratio higher than 1% the ascending part of the compressive stress-strain relationship becomes less steep with increasing amount of fibres. The effect on the post-peak behaviour is discussed later in this thesis.

2.1.2 Parameters influencing FRC

The behaviour of fibre reinforced concrete is mostly influenced by the fibres that it contains. Therefore, the parameters that influence FRC are the fibre volume ratio, fibre length, fibre aspect ratio and fibre tensile strength. Additionally, FRC is necessarily influenced by the concrete used for the matrix and thus its strength.

Fibre volume ratio modifies the properties of concrete rather significantly. The higher the fibre content, the higher the strength of concrete. For example, an increase in fibre volume content from 0.5 to 1.0 % increases the direct tensile strength from 1.1 to 1.3 times that of plain concrete and the toughness from 1.8 to 2.7 times that of plain concrete (Shah and Rangan, 1971). However, the fibre volume ratio also affects

the workability of freshly mixed concrete and when this ratio is high enough, special mixing and placing methods are required (Zollo, 1997). The range of fibre volume ratio suggested by the ACI Committee is from 0.25 % to 2 % for conventional SFRC.

As described by Deluce and Vecchio (2013), fibre length does not play a significant role in post-cracking behaviour of SFRC containing reinforcing bars. However, in order to be able to transfer the stresses through the fibres, their length must be bigger than crack spacing otherwise they will not bridge cracks. It should also be noted that longer fibres can bridge more cracks.

Fibre aspect ratio is defined as the ratio of fibre length over fibre diameter. A higher aspect ratio leads to a higher surface area and improves the bond between fibres and concrete. Also, even though an increase in the aspect ratio does not enhance the cracking strength of concrete, it improves the post-cracking tensile strength and toughness of the composite material (Shah and Rangan, 1971). However, despite using fibres with a high aspect ratio leads to a more efficient use of the material, it should be ensured that the ultimate strength of the fibres is sufficient to avoid rupture (Deluce and Vecchio, 2013). Similarly to the effect of fibre volume ratio, an increasing aspect ratio decreases the workability of concrete (Johnston, 2010).

The tensile strength of a fibre is the stress at which there is a rupture of the fibre. This tensile strength can go up to 2000 MPa. If the tensile strength is high enough to avoid rupture, the tensile strength of FRC will depend on the bond strength between the fibres and concrete (Susetyo, 2009).

2.2 FRC coupling beams

2.2.1 Test setups

Since one goal of the thesis is to validate a theory against experimental data, the first step of the research is to find and collect multiple tests performed on SFRC coupling beams. Typically, the tests are performed on a SFRC beam connected to two strong RC or SFRC blocks which should be stiff enough to be considered rigid compared to the modelled coupling beam. These rigid blocks represent the shear walls. Since laboratory machines are limited in term of power, tests are usually performed on smaller specimens than in reality (40 cm to 1 m in length). However, their height is also reduced so that the span-to-depth ratio is the same as in reality. Figure 6 shows an example of the tests performed in laboratory. Also, tests can focus on the behaviour of the whole coupled wall system. In this case, the specimen is made of 2 walls connected by coupling beams as shown in Figure 7. In this study, only single beam specimens will be used.

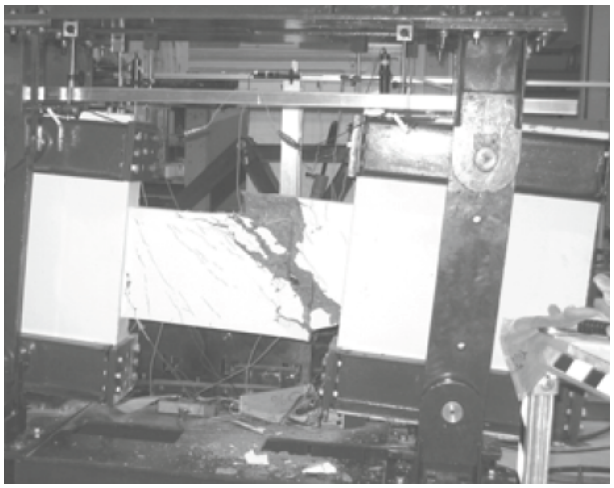

Figure 6: Test specimen for coupling beams (Kuang and Baczkowski, 2006)

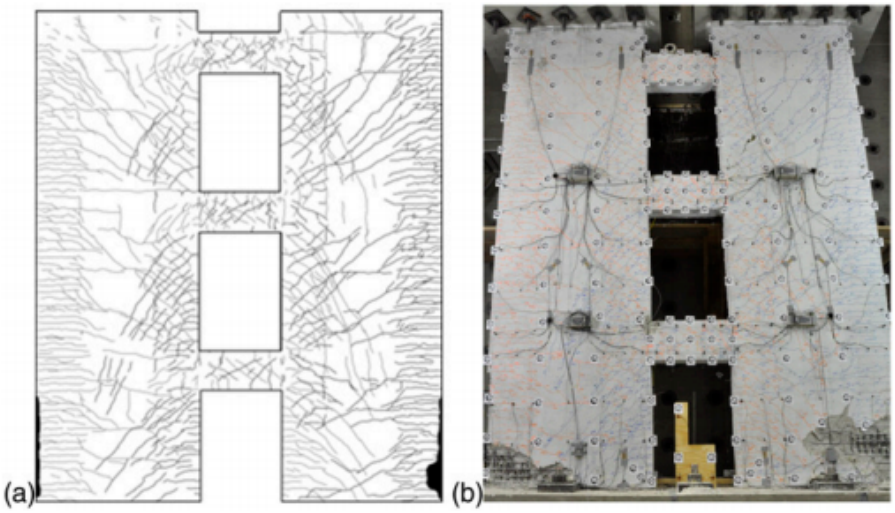

Figure 7: Test specimen for a coupled-wall system (Lehman et al., 2013)

2.2.2 Selected tests

Since this thesis studies the validation on a theory based on the 3PKT model, it must follow the theory's rules and hypotheses. In this regard, criteria must be respected for the purpose of the study. Hypothesis of the 3PKT model will be explained later in this thesis. The restrictions are as follows:

- Beams under double curvature
- Span-to-depth ratio smaller or equal to 2.5
- Beams under monotonic or cyclic loading
- No diagonal reinforcement
- No axial restraint of the specimen

Collected database

The database is shown in Table 1 and Table 2 where values highlighted in blue are guessed values that were not referenced by the authors. Concerning the tests from Kuang and Baczkowski (2006 and 2009), the concrete compressive strength was given as the cube strength of concrete. Since this thesis uses the cylinder compressive strength of concrete, cube values are multiplied by 0.8 to have the cylinder values. Concerning the tensile strength of these specimens, they are taken as $f_t = 0.33\sqrt{f'_c}$.

Authors	Year	Beam name	a/d	b [mm]	d_1 [mm]	d_2 [mm]	h [mm]	a [mm]	m	ρ_{l1} [%]	n_{b1} [bars]	ρ_{l2} [%]	n_{b2} [bars]	f_y [MPa]	ρ_v [%]	f_{yv} [MPa]
Gaochuang et al.	2016	CCB3-30-2-1FS	2.32	150	345	345	400	800	0.5	1.21	2	1.21	2	363.4	0.56	295.6
		CCB3-40-2-1FS	2.32	150	345	345	400	800	0.5	1.21	2	1.21	2	363.4	0.56	295.6
		CCB3-50-2-1FS	2.32	150	345	345	400	800	0.5	1.21	2	1.21	2	363.4	0.56	295.6
		CCB3-60-2-1FS	2.32	150	345	345	400	800	0.5	1.21	2	1.21	2	363.4	0.56	295.6
		CCB3-70-2-1FS	2.32	150	345	345	400	800	0.5	1.21	2	1.21	2	363.4	0.56	295.6
		CCB3-80-2-1FS	2.32	150	345	345	400	800	0.5	1.21	2	1.21	2	363.4	0.56	295.6
		CCB3-40-1-1FS	1.16	150	345	345	400	400	0.5	1.21	2	1.21	2	363.4	0.56	295.6
		CCB3-40-1.5-1FS	1.74	150	345	345	400	600	0.5	1.21	2	1.21	2	363.4	0.56	295.6
		CCB3-50-2-0FS	2.32	150	345	345	400	800	0.5	1.21	2	1.21	2	363.4	0.56	295.6
		CCB3-50-2-0.5FS	2.32	150	345	345	400	800	0.5	1.21	2	1.21	2	363.4	0.56	295.6
		CCB3-50-2-1FS	2.32	150	345	345	400	800	0.5	1.21	2	1.21	2	363.4	0.56	295.6
		CCB3-50-2-1.5FS	2.32	150	345	345	400	800	0.5	1.21	2	1.21	2	363.4	0.56	295.6
		CCB3-50-2-2FS	2.32	150	345	345	400	800	0.5	1.21	2	1.21	2	363.4	0.56	295.6
Kuang and Baczkowski	2006, 2009	S-10/M	1.11	100	360	360	400	400	0.5	2.06	3	2.06	3	469	1	384
		S-15/M	1.67	100	360	360	400	600	0.5	2.06	3	2.06	3	469	1	384
		S-20/M	2.22	100	360	360	400	800	0.5	2.06	3	2.06	3	469	1	384
		S-15/W	1.67	100	360	360	400	600	0.5	2.06	3	2.06	3	469	0	384
		S-15/S	1.67	100	360	360	400	600	0.5	2.06	3	2.06	3	469	2	384

Table 1: Collected database

Authors	Year	Beam name	l_b [mm]	a_g [mm]	f'_c [MPa]	f_t [MPa]	*Fibre type*	V_f [%]	l_f [mm]	d_f [mm]	f_{uf} [MPa]	V_{exp} [kN]
Gaochuang et al.	2016	CCB3-30-2-1FS	575	10	40.5	2.62	Straight	1	32	0.76	380	227
		CCB3-40-2-1FS	575	10	43.1	3.26	Straight	1	32	0.76	380	238
		CCB3-50-2-1FS	575	10	52.9	3.63	Straight	1	32	0.76	380	243
		CCB3-60-2-1FS	575	10	66.7	4.27	Straight	1	32	0.76	380	250
		CCB3-70-2-1FS	575	10	70.1	4.54	Straight	1	32	0.76	380	253
		CCB3-80-2-1FS	575	10	80.7	5.44	Straight	1	32	0.76	380	255
		CCB3-40-1-1FS	575	10	43.1	3.26	Straight	1	32	0.76	380	295
		CCB3-40-1.5-1FS	575	10	43.1	3.26	Straight	1	32	0.76	380	292
		CCB3-50-2-0FS	575	10	55.63	3.4	Straight	0	32	0.76	380	202.5
		CCB3-50-2-0.5FS	575	10	54.49	3.82	Straight	0.5	32	0.76	380	238
		CCB3-50-2-1FS	575	10	54.8	4.64	Straight	1	32	0.76	380	244
		CCB3-50-2-1.5FS	575	10	55.92	5.51	Straight	1.5	32	0.76	380	249.5
		CCB3-50-2-2FS	575	10	55.31	5.96	Straight	2	32	0.76	380	255.5
Kuang and Baczkowski	2006, 2009	S-10/M	700	10	37.52	2.04	Hook-ended	1	50	1.05	1000	298.6
		S-15/M	700	10	38.16	2.02	Hook-ended	1	50	1.05	1000	281.5
		S-20/M	700	10	38.72	2.05	Hook-ended	1	50	1.05	1000	262.2
		S-15/W	700	10	44.96	2.21	Hook-ended	1	50	1.05	1000	130.0
		S-15/S	700	10	45.2	2.22	Hook-ended	1	50	1.05	1000	357.7

Table 2: Collected database (continued)

Gaochuang et al. (2016)

This experimental program was performed to validate an analytical method for designing coupling beams against seismic events. In this regard, they tested 17 SFRC coupling beams under cyclic loading. Their tests were also meant to study the effect of three parameters influencing the shear resistance of the specimens. These parameters were the compressive strength of fibre reinforced concrete, span-to-depth ratio and fibre volume fraction. Each of these specimens were of an approximately 1/3 scale with a constant depth of 400 mm and two rigid RC blocks. The span-to-depth ratio varied from 1.16 to 4.06 and most of them were designed as 2.32 to ensure a shear-dominant failure. The compressive strength of coupling beams varied from 40 MPa to 80 MPa and the fibre volume fraction from 0 % to 2.5 %. However, the compressive strength of the two end blocks was not specified. It is assumed in this thesis that the strength of these blocks was the same as the tested coupling beams. The steel fibres used were straight with a yielding strength of 380 MPa, a length of 32 mm and an aspect ratio of 42. Since no information was given about the ultimate strength of the fibres, it was considered to be equal to their yielding strength for the purpose of this study. Results from their experiments showed that for increasing fibre volume ratio and concrete compressive strength, the shear strength of the members increased. Concerning the span-to-depth ratio, it was observed that an increase of this ratio resulted in a decrease of the shear strength.

The test setup is shown in Figure 8. The system is rotated by 90°. The yellow jack, which pushes and pulls at mid height of the total specimen to induce an anti-symmetrical moment pattern to these coupling beams, is attached to a strong RC wall. The bottom rigid block is fixed to a strong steel floor while the upper block is connected to a system of steel frame. This frame is composed of bars with high stiffness to ensure the stability and safety of the system. The steel frame is used to allow vertical displacement of the coupling beam (no axial restraint) and horizontal displacement while blocking rotation of the upper rigid block to force a double curvature of the coupling beam. Displacements are measured horizontally at the top of the specimen.

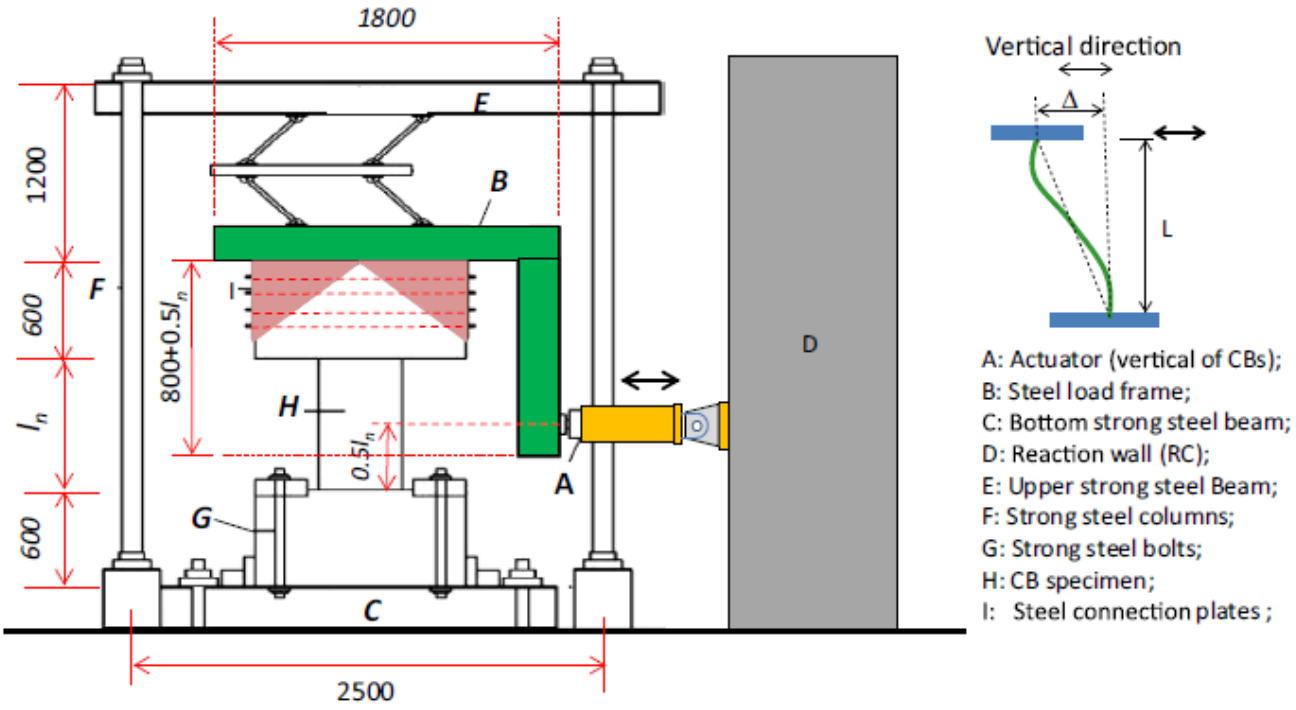

Figure 8: Test setup (Gaochuang et al., 2016)

Kuang and Baczkowski (2006 and 2009)

This experimental program was performed to analyse the effect of three parameters in the resistance of coupling beams: span-to-depth ratio, fibre content and transverse reinforcement. In this regard, 7 specimens were tested in laboratory. The geometric properties of the specimens are shown in Figure 9. The compressive cube strength of the specimens used varies from 45 to 56 MPa, the span-to-depth ratio varied from 1.11 to 2.22 and the transverse reinforcement ratio could have three different values: 0 %, 1% or 2%. The longitudinal reinforcement ratio was the same for all specimens and was equal to 2 %. Five of the specimens had hook-ended fibres included in the concrete matrix with a volume ratio of 1 % and an ultimate tensile strength of 1000 MPa. From these tests, Kuang and Baczkowski concluded that the addition of fibres resulted in an increase of the shear strength. Moreover, they concluded that an increase of the transverse reinforcement ratio also resulted in an increase of the shear strength. However, it was observed that for increasing span-to-depth ratio, the shear strength of coupling beams decreased.

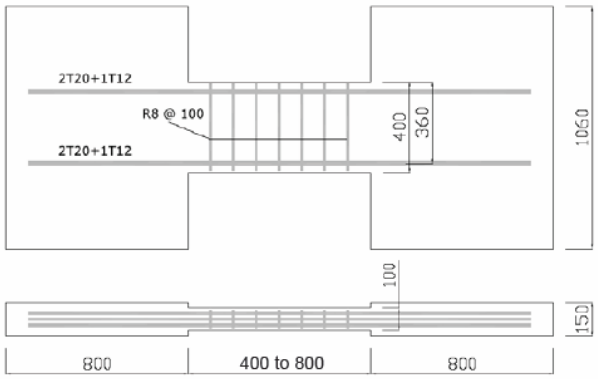

Figure 9: Test specimen (Kuang and Baczkowski, 2006)

Another goal of the experimental program was to provide a new system to test coupling beams. The test setup is shown in Figure 10. It consists of a rotating system whose movement is induced by a hydraulic actuator. This movement creates a rotation of the two rigid end blocks which rotate by the same amount. This creates a double curvature of the coupling beam. Displacements are measured as the relative vertical displacement of the two ends of the coupling beam. Although this system does not seem to allow free elongation of the coupling beam, this test was selected because of the few amount of tests available in the literature. This will require modifications to apply to the model developed later in this thesis.

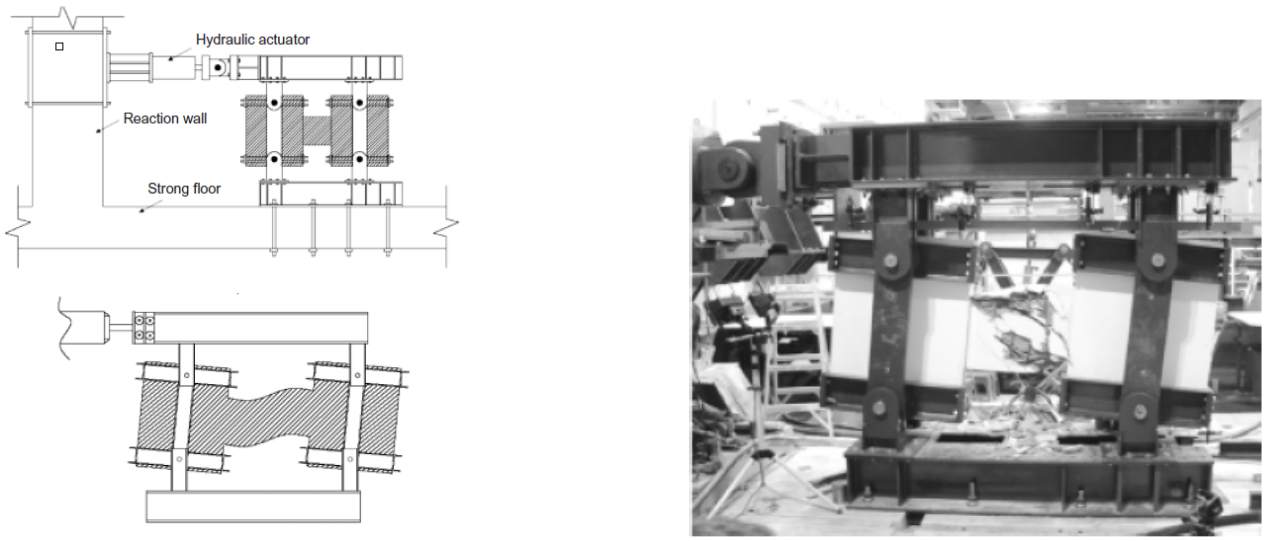

(a) Scheme of test setup

(b) Coupling beam at failure

Figure 10: Test setup (Kuang and Baczkowski,2009)

3 Modelling approaches for RC and FRC deep beams

There are current available ways to model the shear behaviour and find the shear strength of coupling beams. The first method is the strut-and-tie model. The second method is a finite element analysis and finally 2PKT and 3PKT methods proposed by Mihaylov et al. (2013 and 2015).

3.1 Strut-and-tie models

Strut-and-tie models are simple to use and appropriate for the analysis of coupling beams since a relatively important portion of the shear is carried by strut action, where compressive stresses flow directly from the load to the support (Mihaylov et al., 2013). Nonetheless, this method might be too simple in this case because it is not capable of handling all the numerous parameters that influence the shear behaviour. However, this can be a good method in the pre-design process. EC2 does not specify the strut-and-tie model that should be used in each situation and it is up to the designer to make a reasonable and suitable choice depending on the geometry. Figure 11 shows an example of a strut-and-tie model. The model is decomposed into a truss action and an arch action.

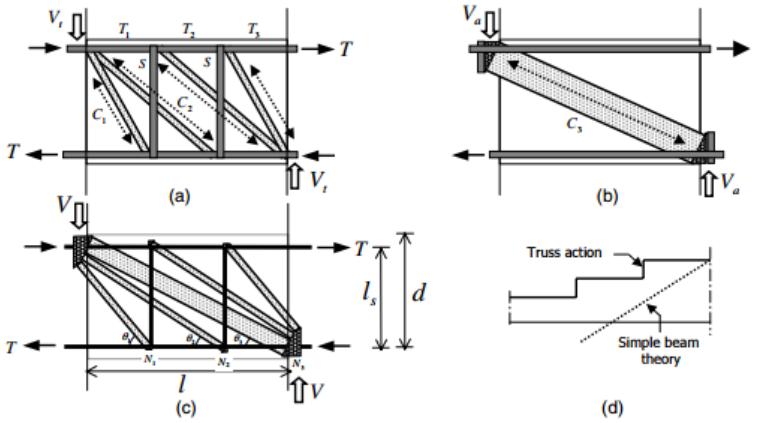

Figure 11: Strut-and-tie models for coupling beams (a) Truss action (b) Arch action (c) Strut-and-tie model (d) Tensile force of top steel (Jang and Hong, 2004)

Despite their simplicity, such models are able to take into account diagonal reinforcement and axial restraint as shown in Figures 12a and 12b. In general, strut-and-tie models represent rather well the disturbed regions but they differ slightly from one model to another.

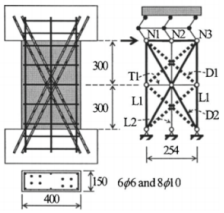

(a) Strut-and-tie model for diagonally reinforced coupling beam (Park and Eom, 2007)

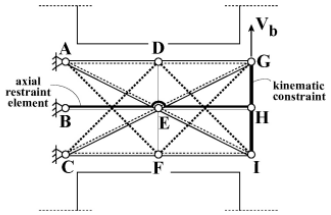

(b) Strut-and-tie model accounting for axial restraint (Barbachyn et al., 2011)

Figure 12: Strut-and-tie models for other types of coupling beams

3.2 Finite element modelling

Finite element method is a particularly complex method which involves the use and understanding of finite element softwares which require additional skills for the designer. Thanks to this complexity, this method is assumed to be more accurate than the strut-and-tie method if the model is correctly input by the designer. The most important part of the work when using this solution is the definition of boundary conditions which must be as close to the reality as possible.

In this thesis, the program VecTor2 developed at the university of Toronto is used. It is a non-linear finite element software which can deal with the presence of fibres either straight or hook-ended, steel or polymer made. It is based on the "Modified Compression Field Theory" developed by Vecchio and Collins (1986). The program is in 2D and is able to apply cyclic loading. Models for the behaviour of concrete (or FRC) are already input into the program and must be carefully chosen when using the software.

The modelling of specimens is rather simple to do and is done with linear, triangular and/or rectangular shapes. Reinforcement can be modelled with linear elements or can be smeared in the concrete. This allows simplicity of utilisation. Although the program was made as easy to use as possible, it still takes time to perform calculations and there is therefore a need for a faster method whose accuracy is not too far from this numerical method.

3.3 Extended 2PKT for FRC simply supported deep beams

3.3.1 Introduction

This method developed by Tvrznikova (2017) is based on the 2PKT proposed by Mihaylov et al. (2013), which is a good compromise between accuracy of results and ease of application. The 2PKT theory is a kinematic model based on equations of equilibrium, compatibility and stress-strain relationships. It is assumed that the shear failure of deep beams, and similarly, coupling beams occurs along a straight critical shear crack that extends from one corner to the opposite near the applied load. The concrete in the highly compressed zone is called the critical loading zone (CLZ) and is supposed to reach a strain of 3.5×10^{-3} at failure (crushing of concrete).

The concrete below the crack is modelled with radial struts flowing to the loading point that connect bottom longitudinal reinforcement. The basic assumption behind the theory is that the motion of the concrete block above the critical crack can be described as a rotation of a rigid block about the top of the crack and a vertical translation. Since the rotation is proportional to the average strain in the bottom reinforcement, $\epsilon_{t,avg}$ while the translation is equal to the vertical displacement of the zone located in the upper corner under compression, Δ_c (Mihaylov et al., 2013), these two parameters represent the degrees of freedom (DOFs) of the model. Δ_c is due to both widening and slip displacement of the critical diagonal crack. The main assumptions for the kinematic model can be seen in Figure 13.

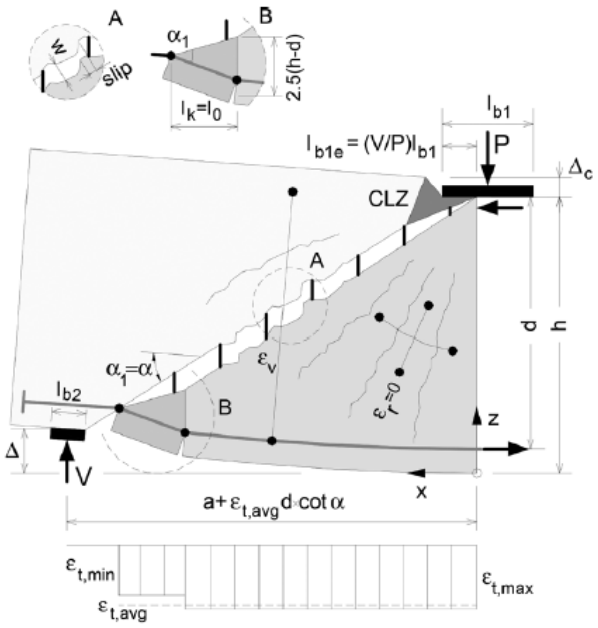

Figure 13: 2PKT kinematic model (Mihaylov et al., 2013)

The two DOFs of the model both have an influence on the rotation of the rigid block about the top of the crack as can be seen in Figure 14. Moreover, it is clear from that figure that both DOFs contribute to an elongation of the transverse reinforcement.

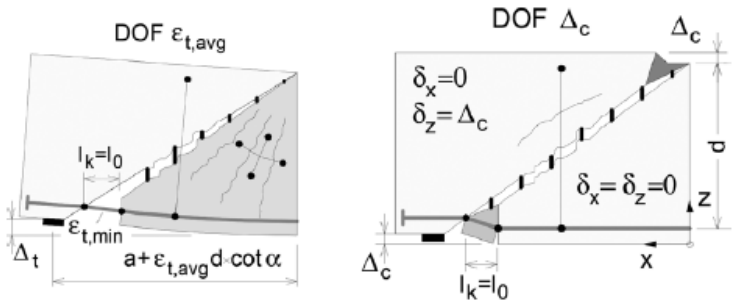

Figure 14: 2PKT degrees of freedom (Mihaylov et al., 2013)

Finally, the angle of the critical crack α_1 should not be taken smaller than the angle θ of the cracks that develop in a uniform stress field. The angle θ can be calculated from the Modified Compression Field Theory or simply be taken as 35° (Mihaylov et al., 2013). This effect occurs in longer coupling beams in which the angle of the straight line joining two opposite corners is too small as shown in Figure 15.

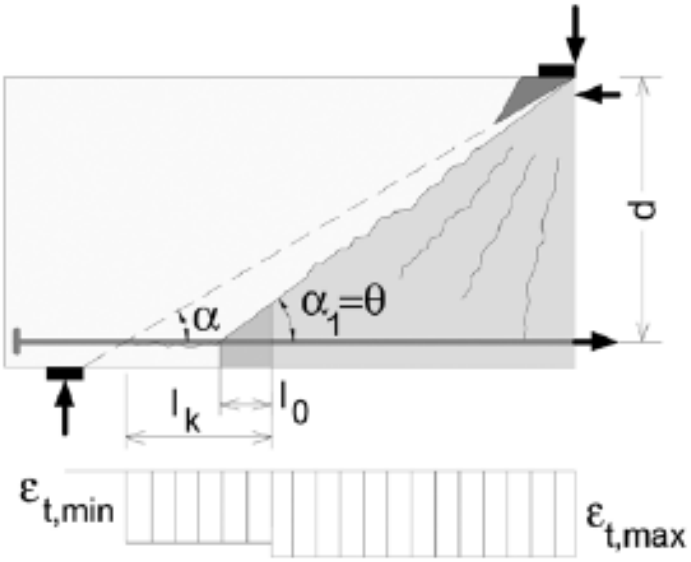

Figure 15: 2PKT - Modification of the angle of the diagonal crack (Mihaylov et al., 2013)

3.3.2 Extended 2PKT

The extended 2PKT is an extension of the 2PKT developed by Mihaylov (2015) in order to predict the whole force-displacement response of a deep beam under high shear forces. As it is based on the 2PKT, it follows the same hypothesis as the latter. The extended 2PKT, estimates 4 distinct shear resistant forces of the deep beam similarly to the 2PKT:

- V_{CLZ} - Shear carried by the critical loading zone (CLZ)
- V_{ci} - Shear carried by the aggregate interlock
- V_d - Shear carried by the dowel effect
- V_s - Shear carried by transverse reinforcement (stirrups)

All parameters are described in Figure 16. All 4 shear resistant parameters are calculated as a function of Δ_c and when summed up, they provide the total shear resisted by the member. In the case of Figure 16, the member considered is a deep beam subjected to rotational moment at one end. Therefore, from moment equilibrium, V can be calculated as follows:

$$V = \frac{T0.9d}{a} \tag{1}$$

where T is the tension in the bottom longitudinal reinforcement, $0.9d$ is the assumed lever arm between the compression force C and T, and a is the shear span.

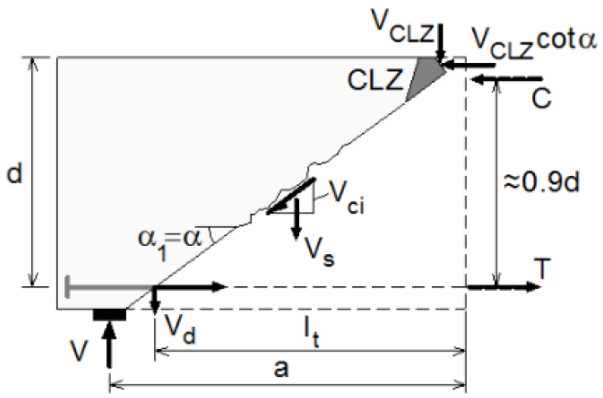

Figure 16: Free-body diagram of the rigid block (Mihaylov, 2015)

Since V needs to be resisted by the 4 parameters mentioned above, the following equation must be respected:

$$\frac{T0.9d}{a} = V_{CLZ} + V_{ci} + V_s + V_d \tag{2}$$

The tension T in the longitudinal reinforcement can be expressed as a function of the average strain in this reinforcement layer. More accuracy can be obtained when accounting for the tension stiffening effect as well. Therefore, T is determined by Mihaylov (2015):

$$T = E_s A_s \epsilon_{t,avg} + \frac{0.33\sqrt{f'_c}}{1+\sqrt{200\epsilon_{t,avg}}} A_{c,eff} \leq A_s f_y \tag{3}$$

where

- E_s - Young's modulus of steel
- A_s - Cross-sectional area of reinforcement
- $A_{c,eff}$ - Effective area of concrete involved in the tension stiffening effect

The limit $A_s f_y$ accounts for the yielding of the reinforcement which occurs in case of flexural failure. $A_{c,eff}$ can be determined by (Eurocode 2, 2004):

$$A_{c,eff} = min\left[2.5(h-b), \frac{h}{2}\right] b \tag{4}$$

Since this theory aims to predict the shear resistance for any value of displacement, all 4 shear resistant parameters have to be calculated as a function of the DOF's. The shear carried by the critical loading zone is defined as a function of the transverse vertical displacement Δ_c of the CLZ. The CLZ has a width that depends on the effective width of the loading plate in case there is such a plate. The concrete in this zone suffers from high compressive stresses and fails when the maximum strain ϵ_{max} reaches the crushing limit of 3.5×10^{-3}. The strain profile in the CLZ is assumed to vary linearly from zero to ϵ_{max} as shown in Figure 17. Diagonal stresses are calculated based on an appropriate stress-strain relationship (Popovics, 1970). From the profile of stresses, an average stress σ_{avg} can be estimated from geometry of the triangle (Figure 17).

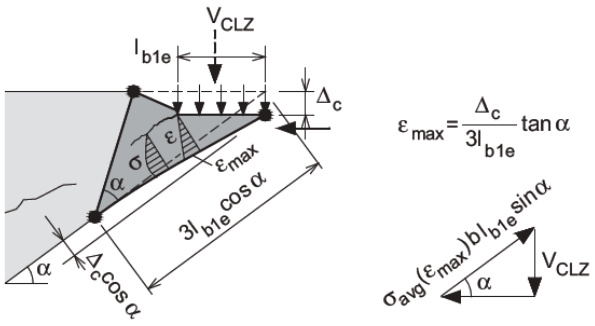

Figure 17: Critical loading zone (Mihaylov, 2015)

Based on the previous hypotheses, the shear carried by the critical loading zone is calculated as:

$$V_{CLZ} = k\sigma_{avg}[\epsilon_{max}(\Delta_c)]bl_{b1e}\sin^2\alpha \tag{5}$$

where k is the crack shape coefficient.

The shear carried by aggregate interlock is obtained by calculating the average shear stress ν_{ci} transferred across the critical crack by interlocking of the rough crack surfaces (Mihaylov, 2015):

$$V_{ci} = 0.18\nu_{ci}bd \tag{6}$$

The relationship between ν_{ci}, crack spacing s and crack width w is computed according to the contact density model developed by Li et al. (1989) where the factor 0.18 is adopted from Vecchio and Collins (1986). The crack slip s is taken from geometry and is given by:

$$s = \Delta_c \sin\alpha_1 \tag{7}$$

The shear carried by the stirrups is expressed using both degrees of freedom. The strain in the transverse reinforcement is calculated based on the hypothesis that the length of stirrups is about $0.9d$. It is given by:

$$\epsilon_v = \frac{\Delta_c + 0.25\epsilon_{t1,avg}d\cot^2\alpha_1}{0.9d} \tag{8}$$

and the stress is the stirrups is calculated by:

$$\sigma_v = min(\epsilon_v E_s, f_{yv}) \tag{9}$$

where f_{yv} is the yielding strength of the transverse reinforcement. Therefore, based on the area of stirrups A_v considered in Figure 31, the force resisted by the stirrups is given by:

$$V_s = \sigma_v A_v = \sigma_v\rho_v b(d\cot\alpha_1 - l_0 - 1.5l_{b1e}) \tag{10}$$

where ρ_v is the ratio of transverse reinforcement and should not be greater than $0.15f'_c/f_y$. The value in brackets should not be smaller than $0.5d\cot\alpha_1$.

Finally, the shear resisted by the dowel effect is calculated based on the transverse displacement Δ_c which creates the dowel effect as shown in Figure 14. The dowel effect becomes more significant by increasing the number of longitudinal bars n_b and their diameter d_b. If the dowel length l_k increases, the dowel effect will be less important. The equation is then as follows:

$$V_d = n_b \frac{12 E_s \pi d_b^4}{64 l_k^3} \Delta_c \leq n_b f_y \frac{d_b^3}{3 l_k} \left[1 - \left(\frac{T}{A_s f_y} \right)^2 \right] \tag{11}$$

where the second part accounts for the formation of plastic hinges at the ends of the dowels.

In the end, the extended 2PKT is solved by increasing Δ_c with steps that are small enough to obtain the full curve with sufficient accuracy. The total displacement Δ consists of two terms: Δ_c and Δ_t. The former has already been explained and the latter comes from the elongation of the bottom reinforcement. As shown in Figure 14, the total displacement is given by:

$$\Delta = \Delta_t + \Delta_c = \frac{\epsilon_{t,avg} l_t}{d} a + \Delta_c \tag{12}$$

where l_t is the length of bottom reinforcement within the cracked part of shear span as illustrated in Figure 16. For each increasing step of Δ_c, the equation (2) must be verified and V is calculated. As of example, a specimen has been taken here. The beam properties have been taken from literature and are described in Table 3.

a/d	b [mm]	d [mm]	h [mm]	V/P	ρ_l [%]	ϕ_l [mm]	*No. bars*	f_y [MPa]	a_g [mm]	f'_c [MPa]	f_{yv} [MPa]	ρ_v [%]	ϕ_v [mm]
1.55	400	1095	1200	0.5	0.70	25.5	6	652	20	33.0	490	0.10	9.5

Table 3: Sample specimen properties - S1M (from Mihaylov et al., 2010)

Figure 18 shows how for a given value of Δ_c, the shear resistant parameters evolve as a function of the bottom longitudinal reinforcement strain $\epsilon_{t,avg}$. The horizontal axis shows the shear force for each parameter while the horizontal axis shows $\epsilon_{t,avg}$. The value of Δ_c taken for this example is equal to 5 mm. The first component to be analysed is the critical loading zone (CLZ). As can be seen from Figure 18, this force is constant. This is because the force in the CLZ is only dependent of Δ_c which is constant, and thus it does not vary with $\epsilon_{t,avg}$. The shear resisted by the stirrups is here constant. This is because the transverse reinforcement is assumed to have yielded and therefore it does not depend on the stirrup strain. It is then calculated considering the area of stirrups in the shear span and their yielding strength. Considering the aggregate interlock, it is affected by the strain in the bottom reinforcement. Because increasing strain $\epsilon_{t,avg}$ leads to wider crack (see Figure 14), it will also lead to less aggregate interlock force since the aggregates will interact less if the crack widens. Therefore, the curve representing the aggregate interlock decreases with increasing strain. Finally, the force resisted by the dowels also decreases with increasing $\epsilon_{t,avg}$. The longer the bars, the longer the lever arm of the dowels and the less the dowel effect is. At one point, the dowel action will have no effect when the bars have yielded. The yielding strain can be easily calculated and is given by:

$$\epsilon_y = \frac{f_y}{E_s} = 3.26 \times 10^{-3} \tag{13}$$

At this strain, the dowel effect is no longer able to transfer stresses.

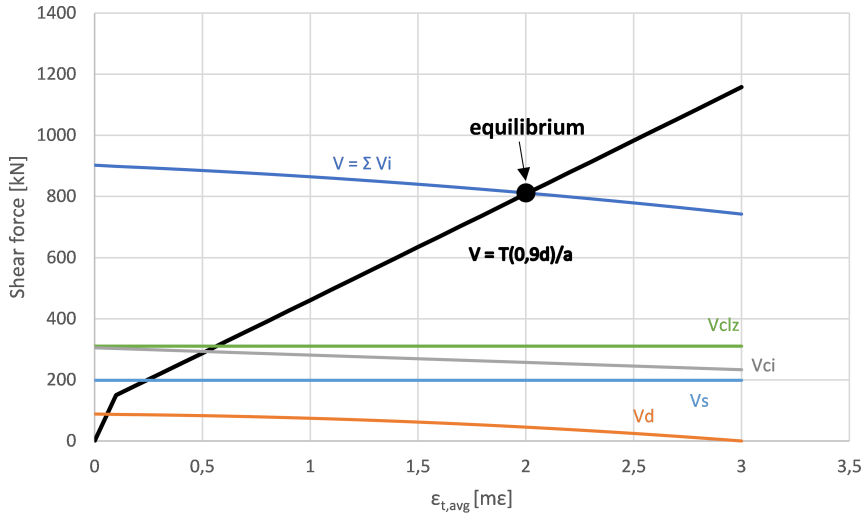

Figure 18: Shear forces in the test specimen for $\Delta_c = 5\ mm$

The thick black line represent the shear obtained from moment equilibrium as derived in equation (2). The curve is bilinear because of the effect of tension stiffening effect already mentioned in this section. The first part of this curve is stiffer because of the contribution of the concrete matrix around the bars which resists tensile forces. The second part represents the contribution of the reinforcement only since the concrete around the bars has reached its tensile strength. To be more accurate, this curve should be trilinear with a flat straight line after the bars have reached the yielding strain ϵ_y. In this example, the bars are assumed to not yield in the domain that we study since this thesis focuses only on the shear failures in which the longitudinal reinforcement does not yield.

The intersection of the thick black line and the blue line representing the sum of all the shear resistant parameters allows to find the strain $\epsilon_{t,avg}$ and the shear force V at equilibrium. The intersection is found iteratively using the bisection method and is shown in Figure 18 wih a big black dot.

Finally, the final curve representing the shear behaviour of the member is found by repeating the previous method for different values of Δ_c. These values of Δ_c will be associated with values of $\epsilon_{t,avg}$ after equilibrium has been found for each one of them. Therefore, the total displacement can also be computed based on equation (12). Figure 19 shows the final curve for the tested specimen. Values have been computed for Δ_c going from 0 to 15 mm with an increment step of 0.1 mm. The horizontal axis represents the total deflection (at mid-span in the test considered) while the horizontal axis shows the shear force resisted by the member. The blue curve represents the sum of all components of the shear forces. All the other curves represent each parameter of the extended 2PKT.

As can be seen from Figure 19, the CLZ provides the most shear resistance. The value of shear force provided by the CLZ increases up to a deflection of 7.5 mm and decreases after that peak. The peak of the CLZ component is found for the same deflection as for the total shear force. This means that failure of the member is driven by the failure of the CLZ. This is the basic hypothesis for the 2PKT, extended 2PKT and 3PKT. It means that the concrete in the critical loading zone crushes. The aggregate interlock, which reaches its peak a bit after the CLZ is the second most important shear resisting component. It reaches zero at for large displacement. This is because with an increasing displacement comes an increasing crack width. When the crack is to wide, the aggregates do not interact with each other. It could be less than

the stirrups component however if the member was even more transversely reinforced. The contribution of stirrups itself increases linearly until the stirrups reach their yielding strength. Afterwards, it no longer depends on the DOF's. Finally, the contribution of the dowel effect is the least significant and reaches its maximum early is the displacement range but it does not vary much throughout the loading.

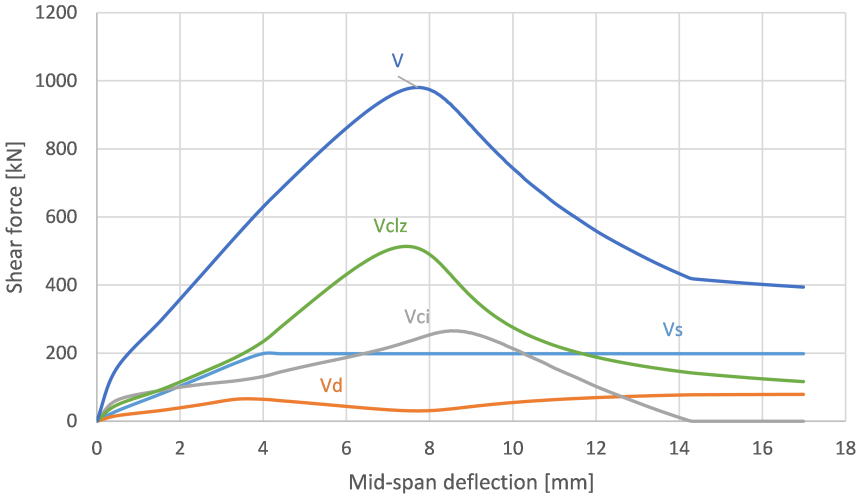

Figure 19: Predicted load-displacement response

The extended 2PKT developed by Mihaylov et al. (2015) is only capable of predicting the shear response for concrete members in single curvature and without fibres. While the 3PKT theory accounts for members in double curvature, it only indicates the peak strength of the member and not the total response. This thesis' objectives are to include the effect of double curvature and fibres in the extended 2PKT.

3.3.3 Extended 2PKT for FRC

This section explains the modifications applied to the extended 2PKT in order to account for the behaviour of FRC deep beams. These modifications, proposed by Tvrznikova (2017) are fully explained in this section. First, a simple model is used to account for the bridging effect of the fibres across the cracks in the concrete and in particular, the diagonal crack. The second adjustment accounts for the effect of fibres on the tension stiffening as described by Lee et al. (2013). Finally, a model for the compressive behaviour of FRC is selected among papers from literature.

3.3.4 Tension in fibres across the main diagonal crack

The main effect of fibres on the concrete is their ability to bridge cracks that occur in the concrete matrix since the latter has a weak tensile strength. Fibres used in concrete generally have an ultimate strength of about 1000 Mpa up to 2000 MPa. The behaviour of fibre reinforced concrete (FRC) in uniaxial tension is therefore widely improved. While for regular concrete, the tensile stress drops after it reaches its peak, the fibres allow for the FRC to have significantly larger displacements. In this way, the tensile stress in the FRC member decreases more gently and bring ductility to the material.

This effect was studied by Voo and Foster (2003) and it is clear from Figure 20 that the behaviour of concrete with the inclusion of fibres is improved. The dash-dotted line represents the tensile response of regular concrete. After the peak stress, the tensile stress decreases rapidly although it is slightly slowed down by the effect of tension softening. This tension softening effect comes from the interaction of the aggregates from both sides of the member at the zone of the crack. However, once the crack width becomes

large enough, aggregates can no longer interact and the tensile stress reaches 0. In FRC however, fibres crossing the crack interface significantly contribute to the load-carrying mechanism so that a higher tensile stress, which is the sum of the tensile resistance provided by the fibres and the tension softening, can be obtained even at large crack widths (Lee et al., 2011).

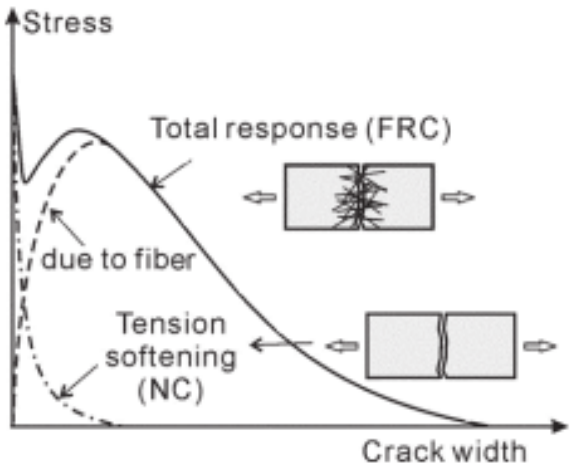

Figure 20: Tensile behaviour of FRC vs. Normal concrete (NC) (Voo and Foster, 2003)

In the case of coupling beams, the crack will be diagonal and thus the fibres will have an effect on the total vertical shear force that can be resisted by the member. It means that an additional force V_f has to be considered and added to the 4 shear resistant parameters. This addition of force will result in an increased shear resistance of the member.

In terms of stresses, the tensile stress f_f from the action of fibres can be estimated using the Simplified Diverse Embedment Model (or SDEM) developed by Lee et al. (2013).. This model describes how stresses are transferred through the crack considering the concrete matrix and the fibres. However, in this thesis, only the contribution of fibres will be considered and the tensile resistance from the concrete matrix will be neglected. This method will be used to find the force F_f which is perpendicular to the diagonal crack. From geometry, the vertical component of this force V_f is calculated by using the angle of the diagonal crack α_1.

An example is shown in Figure 21 to demonstrate the evolution of the tensile stress f_f in the fibres with respect to the crack width in the concrete member. It can be seen that the peak is reached for a small crack width and then decreases almost linearly until a it reaches a very low value. This example has been taken for a volume of fibres of 1 % in the concrete matrix with a length of 30 mm and a diameter of 0.7 mm. The concrete used to generate the curve has a compressive strength of 40 MPa.

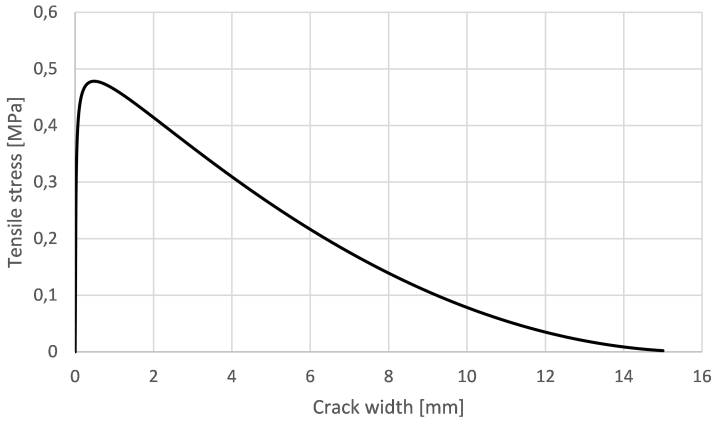

Figure 21: Tensile strength of fibres as a function of crack width

The analysis of fibres in concrete is rather complex and needs to be thoroughly analysed. Lee et al. (2011) proposed a model called the Diverse Embedment Model (DEM) which predicts the tensile stress of the fibres across the cracks. In order to derive this stress, equilibrium and compatibility equations are considered in the analysis of the pull-out behaviour of a single fibre embedded on both sides. The embedment is accounted for by using two main anchorage systems: frictional bond and end-hook anchorage. This condition means that the DEM can account for straight fibres as well as hook-ended fibres. The DEM is also able to consider fibre orientation by using a fibre orientation factor.

However, the calculation of the tensile stress in the fibres with the DEM is rather complex because it involves a double numerical integration (Lee et al., 2013). This is the reason why Lee et al. (2013) developed a simplified method called SDEM which eliminates the integration step by neglecting the slip on the longer embedded side. Anchorages are therefore considered using the same approach as for the DEM but limited by coefficients that prevent the overestimation of the tensile stress attained by the fibres.

In order to use to SDEM in the analysis, several parameters must be known such as the compressive strength of concrete, the volume ratio of fibres, their length and their diameter (or aspect ratio). In the case of hook-ended fibres, the inner length should be given. This length is in general equal to the total length of the fibre minus 8 mm.

Given all this information , the SDEM analysis can be performed. In order to find the tensile stress in SFRC (f_{SFRC}), two parameters must be calculated. They consist of the stress in the fibres (f_f) and the tensile stress in the concrete from tension softening ($f_{c,soft}$). The total stress is equal to the sum of the former and the latter:

$$f_{SFRC} = f_f + f_{c,soft} \tag{14}$$

Estimating $f_{c,soft}$ can be performed using solutions from literature. Voo and Foster (2003) proposed the following relationship:

$$f_{c,soft} = f_{cr} e^{-c w_{cr}} \tag{15}$$

where f_{cr} is the cracking strength of concrete which is estimated as $0.33\sqrt{f'_c}$ (Ramaswamy et al., 1994). The coefficient c is taken as 15 or 30 for concrete or mortar, respectively, and w_{cr} is the average crack width. Thanks to the simplification of the SDEM, the pull-out behaviour of the fibres is evaluated by

two separate terms where the first one represents the bond anchorage and the second one represents the end-hook anchorage. Therefore, the tensile stress in the fibres only can be calculated by:

$$f_f = f_{st} + f_{eh} \tag{16}$$

where f_{st} is the tensile stress due to the frictional behaviour of the fibres and f_{eh} is the tensile stress due to the end-hook anchorage. These two parameters which depend on the crack width can be calculated by:

$$f_{st} = \alpha_f V_f K_{st} \tau_{f,max} \frac{l_f}{d_f} \left(1 - \frac{2w_{cr}}{l_f}\right)^2 \tag{17}$$

$$f_{eh} = \alpha_f V_f K_{eh} \tau_{eh,max} 2 \left(\frac{l_i - 2w_{cr}}{d_f}\right) \tag{18}$$

where $V_f$is the fibre volume ratio, l_f is the fibre total length, l_i is the fibre inner length, d_f is the fibre diameter, α_f is the fibre orientation factor (assumed to be equal to 0.5 (Lee et al. (2013)), K_{st} is the bond modulus and τ is the pull-out strength of a single fibre. The pull-out strength of the fibre can be taken from formulas derived by Voo and Foster (2003). The latter are all shown in Table 4.

Fibre type	Matrix	Pull-out strength [MPa]
Straight	Concrete	$0.396\sqrt{f'_c}$
	Mortar	$0.330\sqrt{f'_c}$
End-Hooked	Concrete	$0.825\sqrt{f'_c}$
	Mortar	$0.660\sqrt{f'_c}$

Table 4: Pull-out strength of a single fibre (Voo and Foster, 2003)

The hypothesis for the fibre orientation ratio to be equal to 0.5 is realistic for members with dimensions that are a lot greater than the fibre length (Lee et al., 2013). If some of the dimensions are too close to l_f, the fibre orientation factor should be modified as shown in Figure 22.

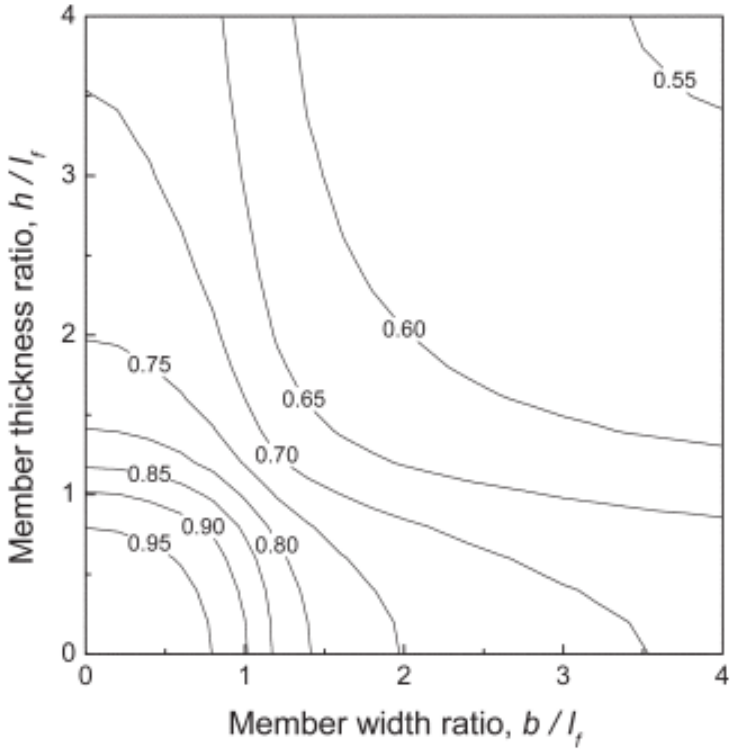

Figure 22: Fibre orientation factor for 3-D elements (Lee et al., 2011)

The evaluation of bond moduli are calculated base on crack width compared with fibre length (Lee et al., 2013):

$$K_{st} = \frac{\beta_f}{3}\frac{w_{cr}}{s_f} \; for \; w_{cr} < s_f \tag{19}$$

$$K_{st} = 1 - \sqrt{\frac{s_f}{w_{cr}}} + \frac{\beta_f}{3}\sqrt{\frac{s_f}{w_{cr}}} \; for \; w_{cr} \geq s_f \tag{20}$$

$$K_{eh} = \beta_{eh}\left[\frac{2}{3}\frac{w_{cr}}{s_{eh}} - \frac{1}{5}\left(\frac{w_{cr}}{s_{eh}}\right)^2\right] \; for \; w_{cr} < s_{eh} \tag{21}$$

$$K_{eh} = 1 + \left(\frac{7\beta_{eh}}{15} - 1\right)\sqrt{\frac{s_{eh}}{w_{cr}}} - \frac{2(\sqrt{w_{cr}} - \sqrt{s_{eh}})^2}{l_f - l_i} \tag{22}$$

$$K_{eh} = \left(\frac{l_i - 2w_{cr}}{2l_i - l_f}\right)K_{eh,i} \; for \; \frac{l_f - l_i}{2} \leq w_{cr} < \frac{l_i}{2} \tag{23}$$

where β_f is a coefficient reflecting the effect of fibre slip on the longer embedded side and has been analytically determined as 0.67. Similarly, β_{eh} is defined as 0.76. These two coefficients prevent the tensile stress to be overestimated due to the hypothesis of neglected fibre slip on the longer embedded side (Lee at al., 2013).

The value of s_f which refers to a slip at maximum tensile force due to mechanical anchorage of a fibre with an inclination angle of 0 degrees with respect to the crack surface and is assumed to be equal to 0.01 mm as showed from experiments by Naaman and Najm (1991). The value of s_{eh} describes the slip at maximum tensile force due to mechanical anchorage of a hook-ended fibre and has been derived from the same experiments to be equal to 0.1 mm.

Finally, the value $K_{eh,i}$ is the value of K_{eh} at $w_{cr} = (l_f - l_i)/2$ calculated from equation (22). A Matlab code was developed by Tvrznikova (2017) and it proved to match closely the reality when compared to laboratory experiments from Susetyo (2009) and Lim et al. (1987).

Since the inclusion of the SDEM in the 3PKT (or extended 2PKT) results in an additional shear resistance, the fraction of the additional force must be accurately calculated. Because the fibres will bridge the main diagonal crack which has an angle α_1 with respect to the horizontal axis, the portion of the total force F_f that resists shear forces is vertical (V_F). The tensile stress in the fibres is given by f_f and acts on the whole length of the diagonal crack. If β is the angle between F_f and V_F, the shear force can be calculated as follows:

$$V_F = \frac{f_f b d}{\sin \alpha_1} \cos \beta \tag{24}$$

Three different methods can be used to define and find the angle β. The first one is the most conservative and assumes that $\beta = \alpha_1$. This scenario assumes that the angle β stays the same throughout the whole loading process. In reality, the diagonal crack keeps widening and the block below the diagonal crack slides along the crack which results in a decreasing angle β. Because of this reason, another scenario is considered in order to account for the effect of the crack width and slip onto the angle β:

$$\beta = \arctan \frac{s}{w} \tag{25}$$

where s is the slip and w is the crack width. They are defined as a function of the DOf's as taken from equation (7) for the slip and the following for the crack width:

$$w = \epsilon_{t,avg} \frac{l_k}{2 \sin \alpha_1} + \Delta_c \cos \alpha_1 \tag{26}$$

The last scenario is to consider the resulting force from the fibres to be vertical and thus set the angle β to 0. The influence of such parameter was tested by Tvrznikova (2017) and proved to be insignificant on the results as shown in Figure 23. Therefore, the most simple relationship for beta has been chosen ($\beta = 0$).

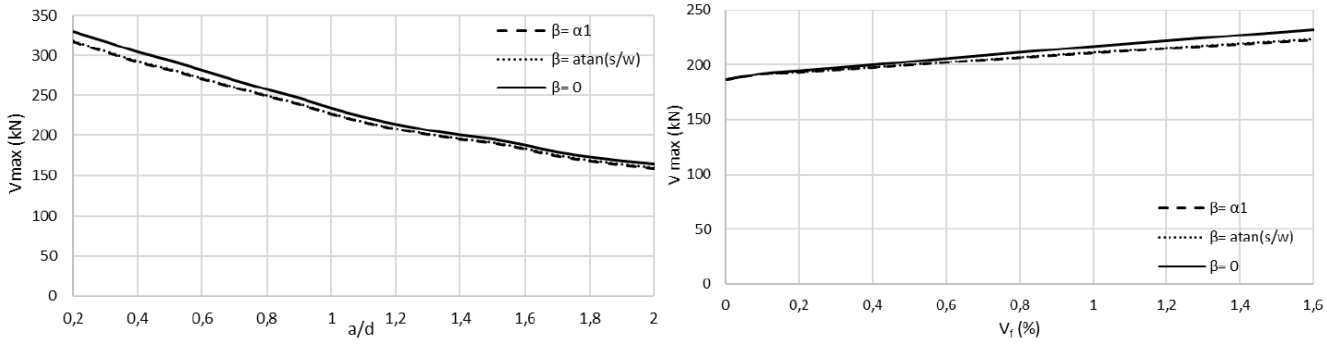

Figure 23: Variation of the angle β given for different a/d ratios and fibre volume ratios (Tvrznikova, 2017)

As of example, the sample specimen can be modelled with an included volume of fibres. If a volume of fibres of 1 % is considered with a fibre length of 30 mm, a diameter of 0.7 mm and a tensile strength of 1115 MPa, results on the shear strength for a given Δ_c is shown in Figure 24 where the effect of fibres is represented in yellow. The value in blue dotted line represents the shear strength without the addition of

fibres. It can be seen that the shear strength is improved by the addition of fibres and that the equilibrium is found for a larger strain in the longitudinal reinforcement. The shear strength provided by the fibres shows a slight decrease with increasing $\epsilon_{t,avg}$ because with increasing longitudinal reinforcement strain comes wider crack.

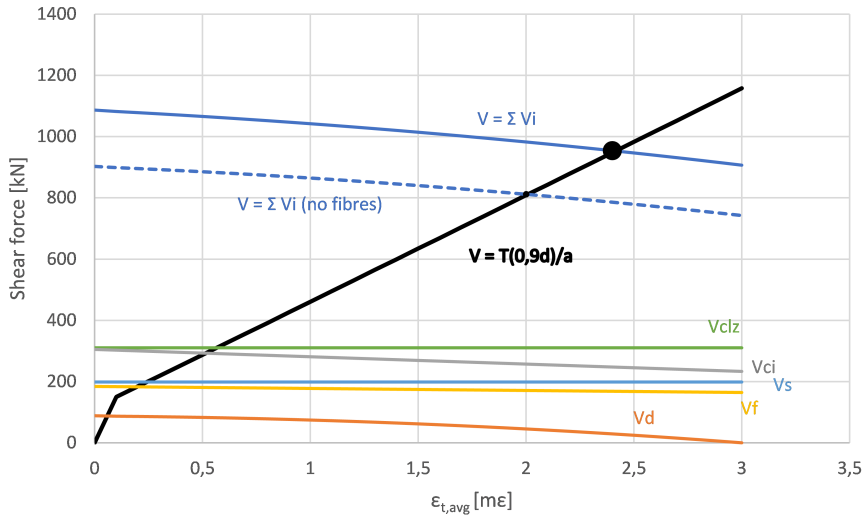

Figure 24: Effect of the fibres for given $\Delta_c = 5\ mm$

Figure 25 shows the effect of the fibres on the total response of the member. It can be seen that the fibres have more effect when the total displacement is relatively small and decreases with increasing deflection. This effect is again due to the widening of the crack caused by the increasing of the total displacement. The inclusion of 1 % fibres in volume increases the maximum shear strength by a value of about 220 kN at the location of the peak load which represents an increase of 22 %.

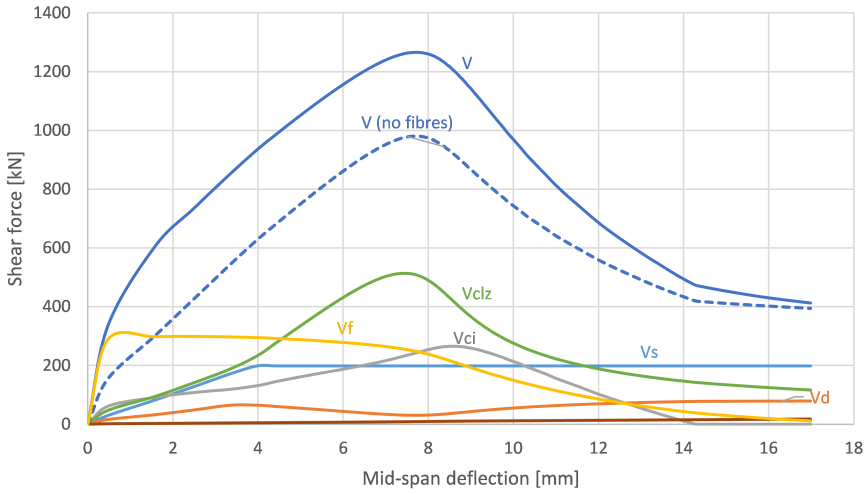

Figure 25: Effect of the fibres on the force-displacement curve

3.3.5 Tension stiffening effect

Considering that the fibres have an effect on the tensile strength of concrete it seems natural to think that they will have an important impact on the tension stiffening effect which relies on the ability of

concrete to transfer tensile stresses. In the extended 2PKT, equation (3) is used to describe the tension stiffening effect. However, fibre reinforced concrete shows a slightly different response when subjected to direct tensile forces. Lee et al. (2013) proposed a relationship for FRC members subjected to tensile forces as shown in Figure 26. It can be seen that there is no influence of the fibres in the initial part of the graph, that is when no crack has been formed yet, and after the first crack has been formed, the FRC member is always able to resist higher tensile stresses.

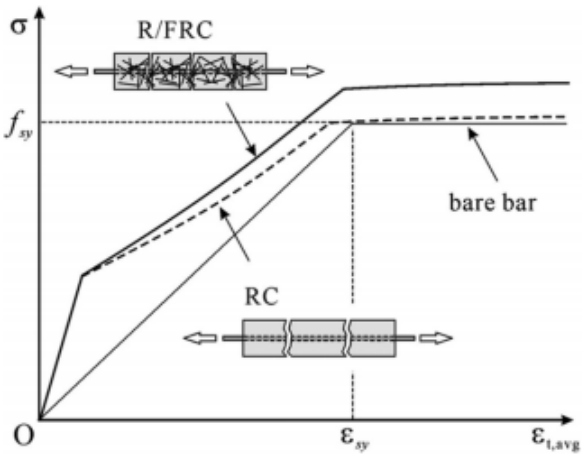

Figure 26: Tensile behaviour of RC and R/FRC members (Lee et al., 2013)

In this model, this effect has an influence on the tensile force T in the longitudinal reinforcement. Therefore, equation (3) can no longer be considered and the model proposed by Lee et al. (2013) is chosen. The formulation from the former is to describe the tensile force as a sum of 3 components which are the tensile force in the rebar (F_{reb}), the tensile force in the fibres (F_{fib}) and the tensile force in the concrete from the tension stiffening effect (F_{con}):

$$T = F_{reb} + F_{fib} + F_{con} \tag{27}$$

The first term of the equation is simply derived from elasto-plastic theory. Given the average tensile strain in the rebar, the force is given by:

$$F_{reb} = E_s A_s \epsilon_{t,avg} \ \leq \ A_s f_y \tag{28}$$

The second term is derived from the SDEM theory which estimates the tensile stress in the fibres. Given $A_{c,eff}$ the area around the bars which contributes to the tension stiffening effect from equation (4), the contribution of the fibres is given by:

$$F_{fib} = f_f A_{c,eff} \tag{29}$$

Since tensile stresses from the SDEM are calculated for given crack widths while the tensile force in the rebar is calculated for a given average tensile strain, a relationship between the two of them needs to be considered. Lee et al (2013) proposed a relationship modified from Deluce (2011) where average crack spacing is given by:

$$s_{cr} = 2\left(c + \frac{s_b}{10}\right) k_3 + \frac{k_1 k_2}{s_{mi}} \tag{30}$$

where s_b is the maximum spacing between reinforcing bars and all the other variables are taken as:

- $c = 1.5a_g$ (a_g: maximum aggregate size)
- $k_1 = 0.4$ (for deformed bars)
- $k_2 = 0.25$ (for uniform strain condition)

$$s_{mi} = \frac{\rho_s}{d_b} + \frac{\alpha_f V_f}{d_f} max\left(\frac{\frac{l_f}{d_f}}{50}, 1\right) \tag{31}$$

$$k_3 = 1 - \frac{min(V_f, 0.015)}{0.015}\left[1 - min\left(\frac{50}{\frac{l_f}{d_f}}, 1\right)\right] \tag{32}$$

where d_b is the bar diameter and ρ_s the ratio of reinforcement within the area $A_{c,eff}$. α_f is the fibre orientation factor taken as 0.5 for simplicity. This hypothesis is valid for an infinite member and should be calculated using the DEM considering member size if the hypothesis is not valid (Lee et al., 2013). With this estimation of crack spacing, the relationship between crack width and average tensile strain is given by:

$$w_{cr,T} = s_{cr}\epsilon_{t,avg} \tag{33}$$

Finally, the force F_{con} is calculated considering the tension stiffening (or softening) effect of the concrete around the bars:

$$F_{con} = f_{ct}A_{c,eff} \tag{34}$$

where f_{ct} is the tension response due to bond mechanism of the reinforcing bar and is described as:

$$f_{ct} = max(f_{c,soft}, f_{c,TS}) \leq E_c\epsilon_{t,avg} \tag{35}$$

where E_c is the elastic modulus of concrete defined as $3300\sqrt{f'_c}+6900$ (from CSA A23.3-04, 2004) and $f_{c,TS}$ is the tension stiffening effect that accounts for steel fibres as described by Lee et al. (2013). This model has been taken from a model made for conventional reinforced concrete (Bentz, 2005) and modified in order to consider the effect of steel fibres:

$$f_{c,TS} = \frac{f_{cr}}{1 + \sqrt{3.6c_f M_b \epsilon_{t,avg}}} \tag{36}$$

where f_{cr} is the cracking strength of concrete taken as $0.33\sqrt{f'_c}$, M_b is the bond parameter defined as $M_b = \frac{A_{c,eff}}{\sum d_b \pi}$ and c_f is the coefficient that accounts for steel fibres. It was defined based on a parametric study conducted by Lee et al. (2013), based on fibre volume ratio, fibre type and reinforcement ratio, and is given by:

$$c_f = 0.6 + \frac{1}{0.058}\left(\frac{l_f}{d_f}\right)^{0.9}\frac{100V_f}{M_b^{0.8}} \text{ for straight fibres} \tag{37}$$

$$c_f = 0.6 + \frac{1}{0.034}\left(\frac{l_f}{d_f}\right)\frac{(100V_f)^{1.5}}{M_b^{0.8}} \text{ for hook-ended fibres} \tag{38}$$

The tension stiffening effect was correctly input in the Matlab code and verified against experimental data from Bischoff (2003) and Deluce and Vecchio (2013). This effect was implemented in the Matlab code by changing the value of T in equation (1). The tension stiffening was studied by Trvznikova (2017) but it showed to not significantly modify the shear behaviour of the member.

3.3.6 Compressive behaviour of the Critical Loading Zone

The fibres do not only affect the behaviour of concrete under tensile stresses but also under compressive stresses. As the concrete material is extremely brittle in tension, it is also rather brittle in compression. The fibres included in the matrix improve the post-peak behaviour of the member under axial compression forces. Because of this, FRC is more ductile in compression than conventional concrete. This positive effect is due to the bridging of the cracks by the fibres caused by the lateral expansion of concrete in compression. The toughness of the member is increased thanks to the pull-out strength of the fibres (Ou et al., 2012). Figure 27 shows how compressive stresss in concrete are modified when accounting for fibres (model from Ou et al., 2012) compared to a case without fibres (model from Popovics, 1970). In that figure, the sample specimen was considered. It can be seen that the peak stress is slightly higher when using FRC but the most important modification is observed in the post-peak region where the material shows more ductility when it has fibre included in its matrix.

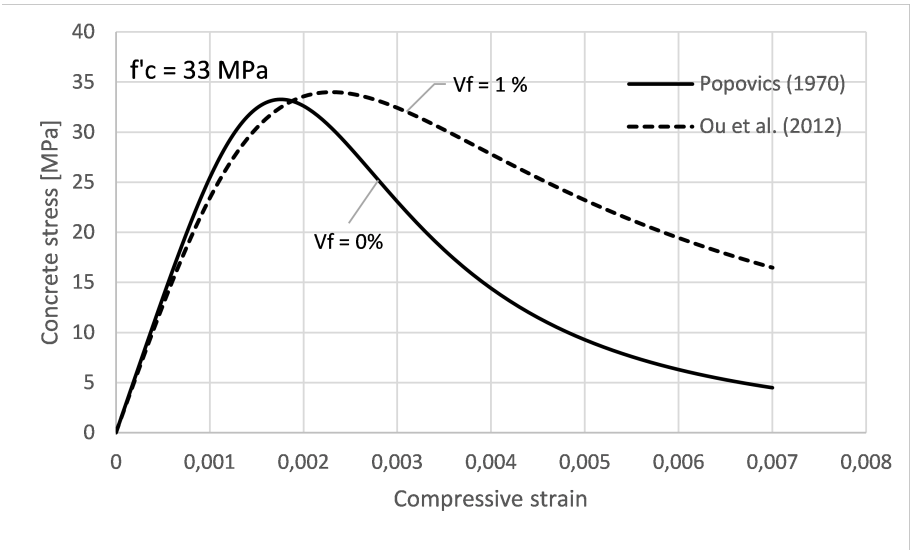

Figure 27: Compressive behaviour of concrete

This effect was studied by Di Prisco et al. (2013) and it was concluded that unless the fibre volume content was greater than 1 %, the compressive strength of FRC is not significantly influenced by the fibres. Since the model developed in this thesis needs to account for fibre volume ratios above 1 %, this effect must be considered. Tvrznikova (2017) analysed different relationships from the literature and found out that for concrete with a compressive strength below 60 MPa, the model proposed by Ou et al. (2012) agreed well with experiments. However, for high strength fibre reinforced concrete, the model from Mansur et al. (1999) was considered. In the case of conventional concrete without fibres, the model proposed by Popovics (1970) was selected. All these considerations are summarised in Table 5.

Concrete type	$f'_c \leq 60MPa$	$f'_c > 60MPa$
RC	Popovics (1970)	Popovics (1970)
FRC	Ou et al. (2012)	Mansur et al. (1999)

Table 5: Models for concrete compression (Tvrznikova, 2017)

In order to be able to include these specifications in the model, the three different models for concrete compression behaviour will be detailed.

Popovics (1970)

This model was proposed for the analysis of conventional concrete under compression and it is well accepted by the scientific community. It defines a stress-strain relationship for concrete as follows:

$$f_c = f'_c \frac{n\left(\frac{\epsilon_{cf}}{\epsilon'_c}\right)}{n - 1 + \left(\frac{\epsilon_{cf}}{\epsilon'_c}\right)^{nk}} \tag{39}$$

where f'_c is the peak stress obtained from a cylinder test, ϵ'_c is the strain at which $f_c = f'_c$ and it is given by:

$$\epsilon'_c = \frac{f'_c}{E_c} \frac{n}{n-1} \tag{40}$$

The factor k is taken as 1 if $\frac{\epsilon_{cf}}{\epsilon'_c} < 1$ and for $\frac{\epsilon_{cf}}{\epsilon'_c} > 1$:

$$k = 0.67 + \frac{f'_c}{62} \geq 1 \tag{41}$$

The curve fitting factor n is defined as:

$$n = 0.8 + \frac{f'_c}{17} \tag{42}$$

The tangent stiffness E_c (when $\epsilon_{cf} = 0$) is defined for two different cases:

$$E_c = 4730\sqrt{f'_c} \text{ for normal strength concrete: } f'_c \leq 40MPa \tag{43}$$

$$E_c = 3320\sqrt{f'_c} + 6900 \text{ for high strength concrete: } f'_c > 40MPa \tag{44}$$

Ou et al. (2012)

Ou et al. tested 40 specimens with variation of fibre diameter, fibre length and fibre volume ratio. The compressive strength of samples was 40 MPa while steel fibres had an ultimate tensile strength of 1000 MPa. All of them were cylindrical with a diameter of 150 mm and a height of 300 mm. Results from the experiments showed that the modulus of elasticity varied with the reinforcing index (amount of fibres) but with low impact. The reinforcing index RI_v is defined as $RI_v = V_f l_f / d_f$. In the case of compressive strength, little correlation with the reinforcing index was observed in the pre-peak zone but fibres proved to significantly influence the post-peak behaviour (Ou et al., 2012). They also observed that the toughness limit was reached for a fibre volume fraction of approximately 2 %. The length of fibres seemed to have an effect on the behaviour as long fibres outperfomed short ones. If ϵ_{c0} is the strain at peak for plain concrete (taken as 0.002 as proposed by Ou et al. (2012)), the model is described as follows:

$$\epsilon'_c = \epsilon_{c0} + 0.0007 RI_v \tag{45}$$

$$\beta = 0.71(RI_v)^2 - 2RI_v + 3.05 \tag{46}$$

$$f'_{cf} = f'_c + 2.35 RI_v \tag{47}$$

$$f_c = f'_{cf} \frac{\beta \left(\frac{\epsilon_{cf}}{\epsilon'_c}\right)}{\beta - 1 + \left(\frac{\epsilon_{cf}}{\epsilon'_c}\right)^{\beta}} \tag{48}$$

Mansur et al. (1999)

Experimental study by Mansur et al. (1999) was conducted on high strength concrete members with hook-ended fibres with a 0.5 mm diameter and 30 mm length. They tested cylindrical specimens with a diameter of 100 mm and a height of 200 mm , 100 mm cubes specimens and 100x100x200 mm prisms for three different fibre volume ratios: 0.5 %, 1.0 % and 1.5 %. Results showed that fibres had an influence on the elastic modulus for vertically cast prisms and cylinders while it did not have much influence for horizontally cast prisms. Concerning the shape effect, it was concluded that the fibre volume ratio had less effect on cylindrical specimens (Mansur et al., 1999). The proposed model for cylinders is the following:

$$f_c = f'_c \frac{\beta \left(\frac{\epsilon_{cf}}{\epsilon'_c}\right)}{\beta - 1 + \left(\frac{\epsilon_{cf}}{\epsilon'_c}\right)^{\beta}} \text{ for } 0 \leq \frac{\epsilon_{cf}}{\epsilon'_c} \leq 1 \tag{49}$$

$$f_c = f'_c \frac{k_1 \beta \left(\frac{\epsilon_{cf}}{\epsilon'_c}\right)}{k_1 \beta - 1 + \left(\frac{\epsilon_{cf}}{\epsilon'_c}\right)^{k_2 \beta}} \text{ for } 1 \leq \frac{\epsilon_{cf}}{\epsilon'_c} \tag{50}$$

$$k_1 = \left(\frac{50}{f'_c}\right)^3 [1 + 2.5(RI_v)^{2.5}] \tag{51}$$

$$k_2 = \left(\frac{50}{f'_c}\right)^3 [1 - 0.11(RI_v)^{-1.1}] \tag{52}$$

$$E_c = (10300 - 400V_f) f_c'^{\frac{1}{3}} \tag{53}$$

$$\epsilon_{c0} = (0.0005 + 0.00000072RI_v) f_c'^{0.35} \tag{54}$$

$$\beta = \frac{1}{1 - \frac{f'_c}{\epsilon_{c0} E_c}} \tag{55}$$

Implementation in the model

In order to be able to input the different models for the compressive behaviour of fibre reinforced concrete in the case of this thesis, an average stress must be calculated. Indeed, for the evaluation of the shear force acting in the critical loading zone for the extended 2PKT, the average stress is used as follows:

$$V_{CLZ} = \sigma_{avg} b l_{b1e} \sin^2 \alpha \tag{56}$$

where σ_{avg} is the average stress in the CLZ. Since the strain in the loading zone is assumed to vary linearly from 0 to the concrete crushing strain, the average strain can be calculated by integrating the stress-strain relationship calculated based on the models previously discussed. In general, the average stress can be calculated for any maximum strain value ϵ in the CLZ. The integration can be calculated by estimating the area under the curve with trapeziums. If this area is called Ω, it is calculated as

$$\Omega(\epsilon) = \int_0^{\epsilon} f_c d\epsilon \approx \sum_i \frac{f_c(\epsilon_i) - f_c(\epsilon_{i-1})}{2(\epsilon_i - \epsilon_{i-1})} \tag{57}$$

The strain axis is divided into increments $\Delta_\epsilon = \epsilon_i - \epsilon_{i-1}$ whose size must be small enough to calculate accurately the area under the curve f_c. Based on this approach, the average compressive stress for a given diagonal strain in the CLZ ϵ is given by:

$$\sigma_{avg} = -\frac{\Omega(\epsilon)}{\epsilon} \tag{58}$$

Based on the previous analysis, the only parameter that will be influenced by this modification is the shear resistance provided by the critical loading zone V_{CLZ}. It can be seen in Figure 28 that for a given Δ_c, V_{CLZ} is increased by the same value for any $\epsilon_{t,avg}$ since it only the shear resistance from the CLZ depends only on Δ_c. The dotted blue line represents the initial total shear resistance without modifications (no fibres, no adjusted stress-strain curve) and the dotted green line is the initial shear resistance provided by the CLZ without modifications.

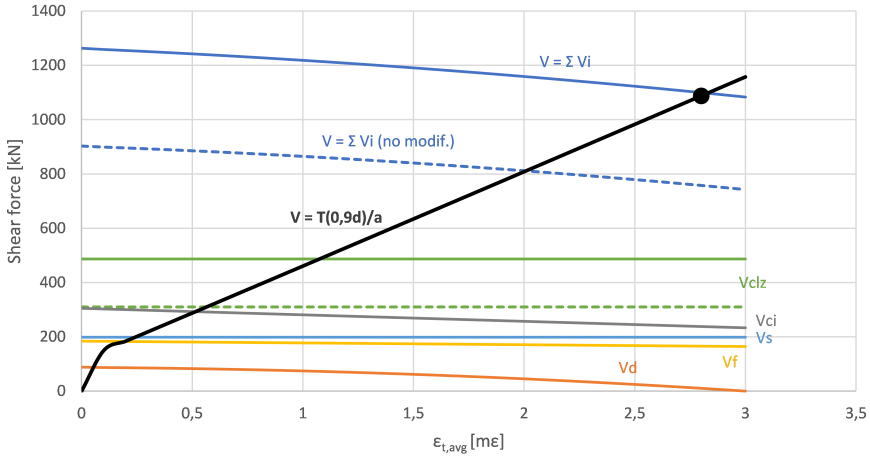

Figure 28: Effect of the adjusted stress-strain curve for given $\Delta_c = 5\ mm$

Figure 29 shows the influence of the modifications on the force-displacement curve. The original V_{CLZ} is drawn with a dotted green line and it can be seen that the effect of the adjusted stress-strain curve happens in the post-peak domain. This results in a more resistant but also more ductile material. It can be observed that overall, the inclusion of fibres increases the strength of the member while increasing its ductility.

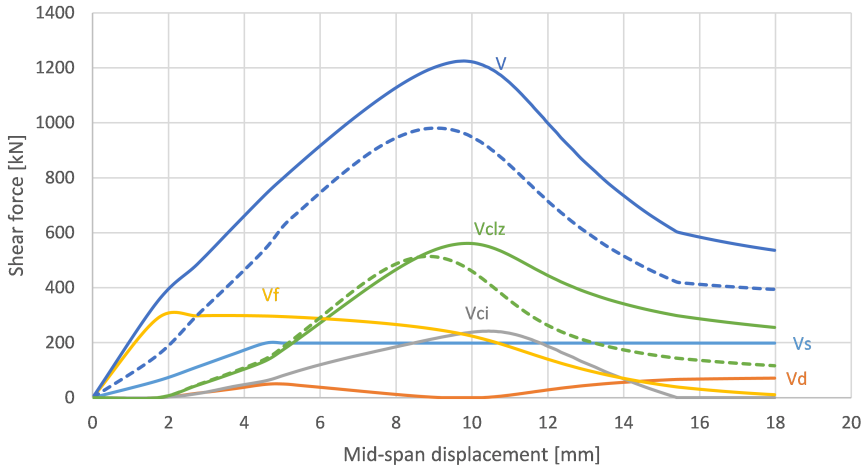

Figure 29: Effect of the adjusted stress-strain curve on the force-displacement curve

3.4 3PKT for RC deep beams

The 3PKT is an extension of the 2PKT proposed by Mihaylov et al. (2015). It is based on the same assumptions as the 2PKT but provides more accuracy because it adds one degree of freedom that accounts for an upper layer of reinforcement in the deep beam. In the 2PKT, the degrees of freedom are the average strain in the bottom reinforcement and the transverse vertical displacement of the critical loading zone (CLZ). It does not consider any influence of potential reinforcement in the upper part of the beam and therefore, it cannot take into account a movement of double curvature but single curvature only. The 3PKT model considers the upper layer of reinforcement and its effect on the field of displacement of the beam. In this theory, the strain in the bottom reinforcement is called $\epsilon_{t1,avg}$, the strain in the top reinforcement is called $\epsilon_{t2,avg}$ while the displacement of the CLZ is still called Δ_c. The three DOFs are shown in Figure 30. In this case, there are two fans of rigid radial struts, one pinned at the loading point and connected to the bottom longitudinal reinforcement for the first pattern ($\epsilon_{t1,avg}$) and the other one pinned at a support point and connected to the top reinforcement for the third pattern ($\epsilon_{t2,avg}$).

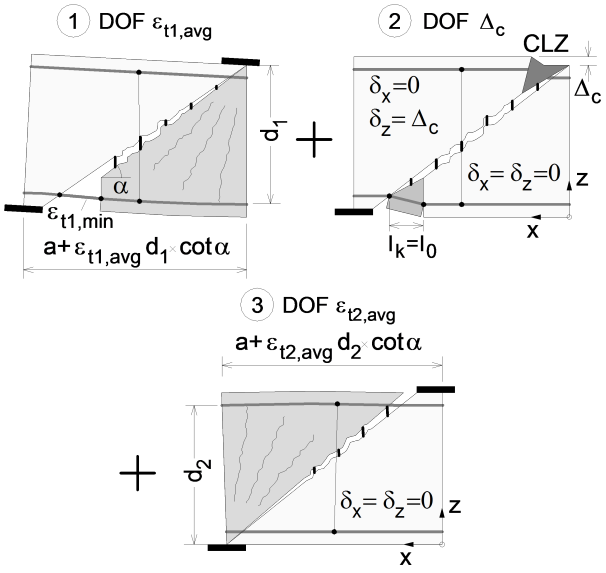

Figure 30: 3PKT degrees of freedom (Mihaylov et al., 2015)

Finally, all three patterns are combined to generate the complete field of displacements of the member based on geometric properties. The results developed by Mihaylov et al. (2015) are shown in Figure 31.

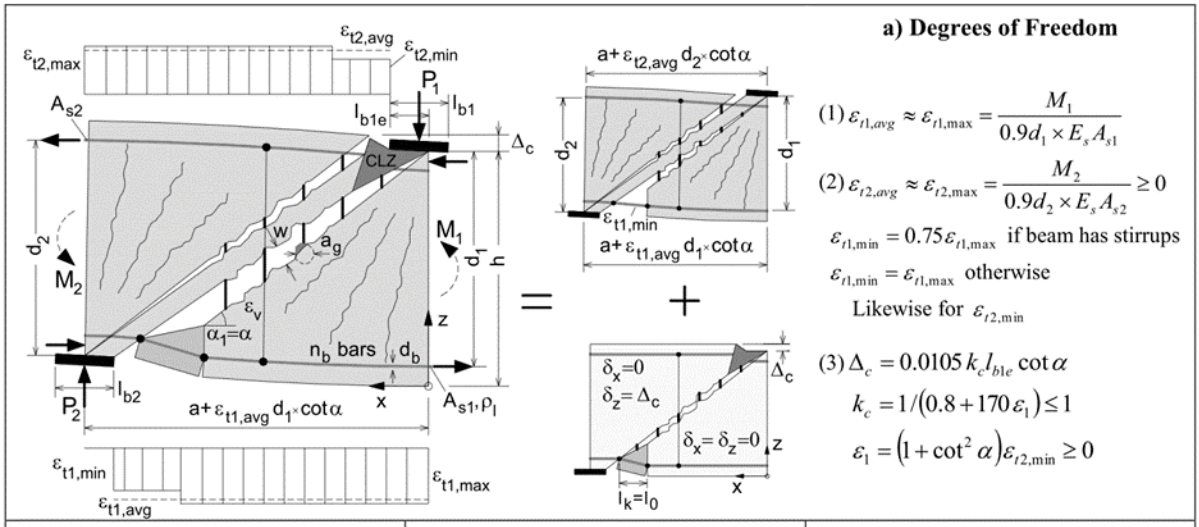

Figure 31: 3PKT for deep beams under single- and double-curvature bending (Mihaylov et al., 2015)

Explanations on the different equations

This section will focus on the explanation of all the parameters if necessary. First, the degrees of freedom related to the reinforcement strains are taken from elastic analysis considering a lever arm equal to $0.9d$ where d is the depth considered (bottom or top reinforcement depth). Therefore, the 2 degrees of freedom are derived as follows:

$$\epsilon_{t1,avg} = \frac{M_1}{d_1 \times E_s A_{s1}} \tag{59}$$

and

$$\epsilon_{t2,avg} = \frac{M_2}{d_2 \times E_s A_{s2}} \tag{60}$$

The minimum strain which is located at the end of the reinforcement is either equal to the average strain if there are no stirrups and $0.75 \times \epsilon_{t,avg}$ if there are stirrups. This effect is due to the fact that the struts formed between each pair of stirrups reduce the forces in the longitudinal reinforcement each time there is a stirrup. In the end, stresses in the longitudinal reinforcement are reduced by about 25 % and so are the strains.

Because of this linear elastic assumption, the model is not able to capture any yielding of the longitudinal reinforcement. However, yielding of the longitudinal reinforcement mostly occurs in flexural failure and not shear failure. The third degree of freedom is derived from the assumption that in the CLZ, the compressive strains vary from zero at the edge of the loading plate to -3.5×10^{-3} just above the critical crack. From Figure 32, it was derived by Mihaylov et al. (2013), considering the previous assumption, that $\Delta_c = 0.0105 l_{b1e} \cot \alpha$.

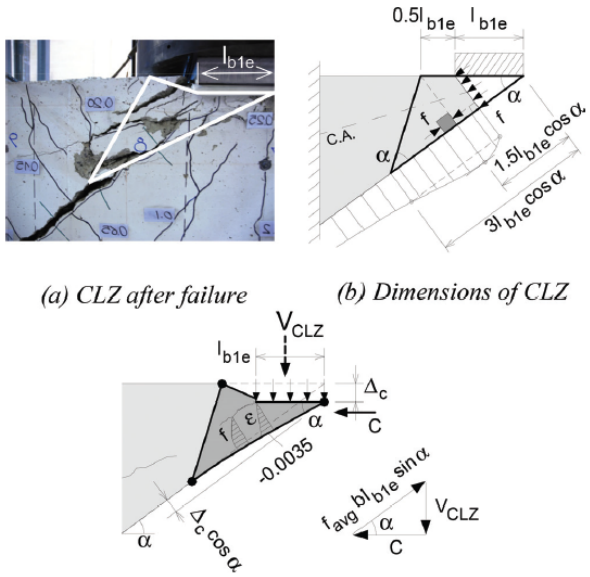

Figure 32: Modelling of CLZ (Mihaylov et al., 2013)

In the 3PKT, there is a compression softening effect of the CLZ because of the tensile stresses induced by the top reinforcement. This effect does not happen in members under single curvature because the top zone remains uncracked in that case. In order to account for the compression softening, a coefficient k_c is included which is based on the top reinforcement strain $\epsilon_{t2,avg}$:

$$\Delta_c = 0.0105 k_c l_{b1e} \cot \alpha \tag{61}$$

Geometry

The length l_{b1e} is the length of the CLZ which is loaded by the applied external force. In deep beams with loading plates, it is a proportion of the plate length (l_{b1}) calculated as the ratio of shear force at the loading plate over the applied load. It is therefore given by:

$$l_{b1e} = \frac{V}{P_1} l_{b1} \geq 3a_g \tag{62}$$

The dowel length l_k is the length of bottom reinforcement whose elongation contributes to the width of the critical crack and is assumed to be equal to the distance between the kinks that develop in the longitudinal bars near the support (Mihaylov et al., 2013) as shown in Figure 15:

$$l_k = l_0 + d(\cot\alpha - \cot\alpha_1) \tag{63}$$

l_0 is the length of the heavily cracked zone at the bottom of the critical crack as shown in Figure 15 (Mihaylov et al., 2013). s_{max} is the spacing of the radial cracks at the bottom of the section and quantity $2.5(h-d)$ is the approximate depth of interaction between the bottom bars and surrounding concrete as shown in Figure 13 (Mihaylov et al., 2013; CEB-FIP Model Code 1990, 1993).

The angle of the critical crack is the same that has been defined for the 2PKT theory and is limited to the angle θ which is modified to 30° in the 3PKT instead of 35°.

The effective area of stirrups is calculated based on the length within the shear span where the critical crack is wide enough to cause important tension in the stirrups (Mihaylov et al., 2013).

Compatibility

The displacement field is calculated based only on geometry and allows to know by how much each point has deformed from its initial position if all three DOF's are known.

The crack width is estimated at mid-depth by the addition of two parameters. The first one accounts for the crack slip due to Δ_c and the second term accounts for the widening due to rotation of the rigid block as shown in Figure 14 (Mihaylov et al., 2013). Finally, the calculation of the stirrup stain is estimated considering that the stirrup length is approximately equal to $0.9d_1$.

Shear strength

The shear resistance of the CLZ is calculated based on the stress-strain curve of concrete under compression. The average stress in the concrete varies from 0 to the crushing strain (-3.5×10^{-3}) and it is calculated as the integral of the curve between these two points and can be approximated by $1.43f_c'^{0.8}$ $[MPa]$ as shown by Popovics (1970). In addition to the factor k_c, it takes into account a factor k which is a crack shape coefficient.

Dowel action is taken into consideration while accounting for the elastic fixed-fixed dowels subjected to relative transverse support displacement Δ_c and for the formation of plastic hinges at the ends of the dowels where the moment capacity is reduced due to the tension force T acting on the bars in the dowel region (Mihaylov et al., 2013). Aggregate interlock is estimated based on a formula taken from literature (Matamoros and Wong, 2003).

The goal of the 3PKT is to find the shear strength of the member. By first estimating V, degrees of freedom can be found based on geometry and finally all parameters for the shear strength can be found and give the updated shear strength. If this new value is equal to the estimated V, then the estimated strength is the actual one. If it is not, V should be modified until the estimation equals the result obtained from 3PKT analysis.

4 Extended 3PKT model for FRC coupling beams

4.1 Introduction

In the previous chapters, a model to describe the behaviour of FRC deep beams was explained. Moreover, a model which considers double curvature of members was described as well. In this section, a new model based on the former and the latter is developed. This model is used for the analysis of FRC coupling beams. Because these coupling beams are made of FRC and are under double curvature, the two previous models are merged to form the new model. A Matlab code is provided in Appendix C.

The case studied by Tvrznikova (2017) is limited to deep beams under single curvature. Therefore, in order to study the case of coupling beams under double curvature, changes have to be made in terms of geometry and analysis.

4.2 Geometry

The geometry of coupling beams is rather simple and implies less parameters than for the general case of deep beams. Indeed, coupling beams have no loading plates as they are placed in between two shear walls. Therefore, there is only 1 shear span that has to be calculated. The shear span in this case corresponds to the whole length of the coupling beam.

Even though there is no loading plate, the critical loading zone of the coupling beam is inserted partially in the wall because the shear force must be transferred from wall to wall by the coupling beam and thus, the length l_{b1e} has to be estimated. Figure 33 illustrates the geometry of the coupling beam that is considered in the analysis.

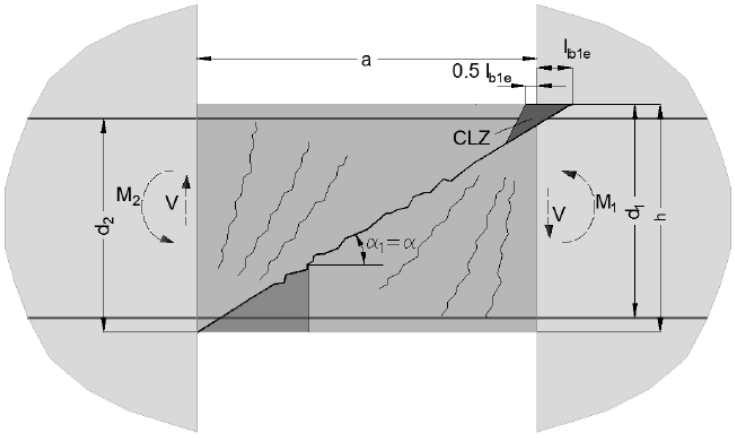

Figure 33: Geometry of the coupling beam (Franssen, 2016)

The value l_{b1e} is described as the length of the loading plate in the original 3PKT and could be explained as the length which transfers shear forces to the member. This role is taken by shear walls in the case of coupling beams. A recent study conducted by Mihaylov et al. (2016) provides an estimation of l_{b1e}:

$$l_{b1e} = 0.11\sqrt{h^2 + a^2} \tag{64}$$

where h is the total height of the coupling beam, a is its length and thus $\sqrt{h^2 + a^2}$ represents the diagonal of the coupling beam. In a general way, l_{b1e} should be calculated as a function of the length of the diagonal crack. However, this length changes when l_{b1e} is modified and therefore, this leads to an

iterative procedure. In order to avoid iteration, the angle α is taken as the angle of the diagonal crack and is fixed to its initial value:

$$\alpha = \arctan\left(\frac{h}{a}\right) \tag{65}$$

and

$$\alpha_1 = \alpha \geq 35^\circ \tag{66}$$

All these modifications have no impact on parameters needed for the 3PKT analysis except for the effective area of stirrups which is modified as follows:

$$A_v = \rho_v \; b \; 0.9d \geq 0 \tag{67}$$

where ρ_v should not be larger than $0.15 f'_c / f_{yv}$.

4.3 Equilibrium

The equilibrium of forces is slightly different from the case of deep beams. Indeed, the support conditions differ from the general case and the internal forces are therefore different. In the case of coupling beams, the two supports are rigid and forces applied are combined shear and bending moment. The bending moment and shear diagrams are shown in Figure 34.

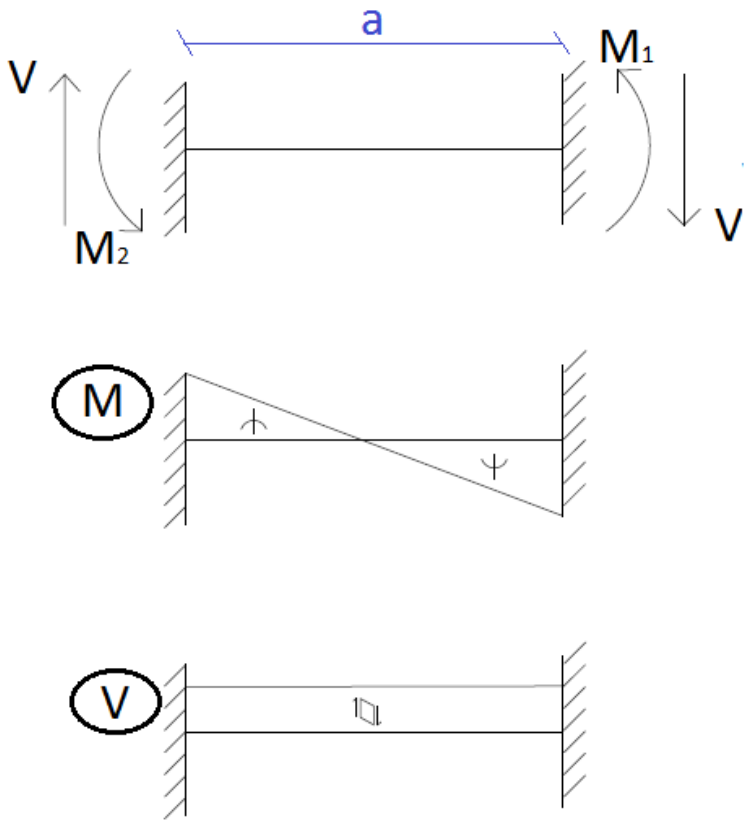

Figure 34: Internal forces in the coupling beam

If the lever arm in the coupling beam is estimated as $0.9d_1$ for M_1 and $0.9d_2$ for M_2 where d_1 and d_2 are the depths of bottom and top layer of reinforcement, respectively. The equilibrium of rotation enables to find the internal shear in the coupling beam:

$$V = \frac{M_1 + M_2}{a} \tag{68}$$

If m is defined as the bending moment ratio such as $m = M_1/(M_1 + M_2)$, then V is given by:

$$V = \frac{T\ 0.9d}{a\ m} \tag{69}$$

This results in a change in equation (2). In order to find the shear resistance of the member, equation (69) must be equal to the sum of all shear resistant parameters: V_{CLZ}, V_{ci}, V_s, V_d and V_F. In order to find these parameters for any displacement value, the extended 2PKT theory is used. However, since the extended 2PKT is based on the 2PKT, modifications need to be introduced to account for the effect of the 3PKT.

4.4 Influence of the symmetry

In the 3PKT, three degrees of freedom are considered. Even though the method for finding the equilibrium of forces in the coupling beam is the same as in the extended 2PKT, the introduction of one additional DOF requires more advanced analysis. Indeed, the calculation requires to find the equilibrium by varying three parameters at the same time. The parameters are the following:

- Δ_c - Transverse vertical displacement of the CLZ
- $\epsilon_{t1,avg}$ - Average tensile strain in the bottom longitudinal reinforcement
- $\epsilon_{t2,avg}$ - Average tensile strain in the top longitudinal reinforcement

However, in the case of coupling beams, the symmetry of the geometry and the symmetry of applied forces implies that $M_1 = M_2 = M$ and thus, $\epsilon_{t1,avg} = \epsilon_{t2,avg} = \epsilon_{t,avg}$. Therefore, the analysis performed to find the total shear remains the same as in the model proposed by Tvrznikova (2017) with two parameters:

- Δ_c - Transverse vertical displacement of the CLZ
- $\epsilon_{t,avg}$ - Average tensile strain in the bottom or top longitudinal reinforcement

The total displacement here is the displacement at the edge of the coupling beam and is the same as defined in equation(12).

4.5 Modification of the critical loading zone

The introduction of consideration of the top reinforcement in the 3PKT induces a softening of the concrete in the critical loading zone. This effect is taken into account in the 3PKT with a use of the factor k_c. This factor has been previously discussed and is equal to:

$$k_c = \frac{1}{0.8 + 170\epsilon_1} \tag{70}$$

where ϵ_1 is the principal tensile strain in critical loading zone and is given by:

$$\epsilon_1 = (1 + \cot^2\alpha)\epsilon_{t2,min} = (1 + \cot^2\alpha)\epsilon_{t,min} \geq 0 \tag{71}$$

Because of this modification, the component V_{CLZ} has to be changed and is now given by:

$$V_{CLZ} = k_c k \sigma_{avg} b l_{b1e} \sin^2 \alpha \tag{72}$$

In order to study the influence of all the modifications applied to the initial model, a sample specimen will be studied. The sample specimen is taken from Gaochuang et al. (2016) and its properties are listed in Table 6.

a/d	b [mm]	d [mm]	h [mm]	m	ρ_l [%]	ϕ_l [mm]	*No. bars*	f_y [MPa]	a_g [mm]	f'_c [MPa]	f_{yv} [MPa]	ρ_v [%]	ϕ_v [mm]	f_{uf} [MPa]	V_f [%]	l_f [mm]	d_f [mm]
2.32	150	345	400	0.5	1.21	20	2	363.4	10	43.1	295.6	0.56	8	380	1.0	32	0.76

Table 6: Sample specimen properties - CCB3-40-2-1FS (from Gaochuang et al., 2016)

It is more convenient for the analysis of coupling beams to show the results in terms of drift instead of displacement. Indeed, the defined measured displacements can vary from one experiment to another. The angle of the drift θ_d is defined for small displacement values as:

$$\theta_d = \frac{\Delta}{a} \tag{73}$$

where Δ is the total transverse displacement calculated with equation (12) and a is the shear span of the coupling beam.

Figure 35 shows the load-drift curve obtained from this analysis. It can be seen that in this example, the transverse reinforcement plays a large role in resisting shear forces.

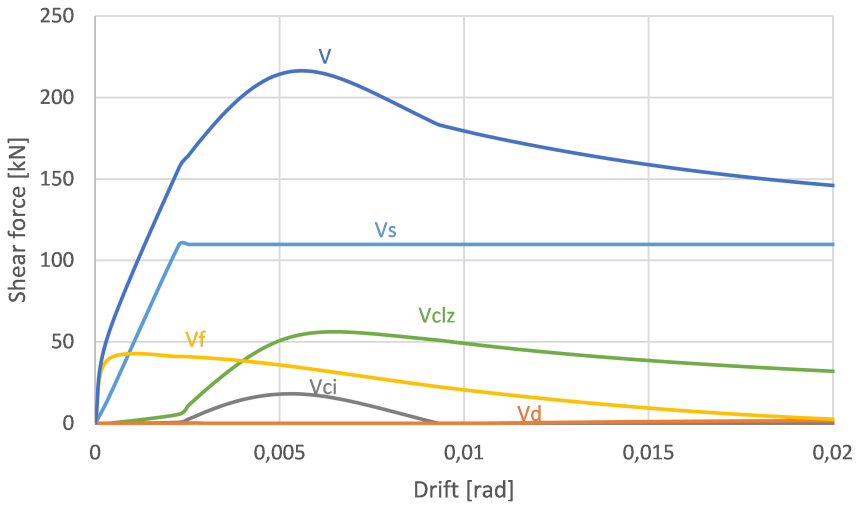

Figure 35: Load-drift curve for the sample coupling beam

However, some hypotheses need to be restrained. First, in this calculation, the coefficient k_c decreases with increasing transverse displacement Δ_c before the peak resistance is obtained and then increases with Δ_c. This means that after the full capacity of the member is obtained, the softened concrete in the CLZ becomes less softened. This is unnatural for the concrete as after crushing it is very unlikely that it will

regain strength. Because of this reason, the coefficient k_c is assumed to remain constant after the peak load is reached. Figure 36 illustrates the variation of k_c as a function of k_c for the considered sample beam.

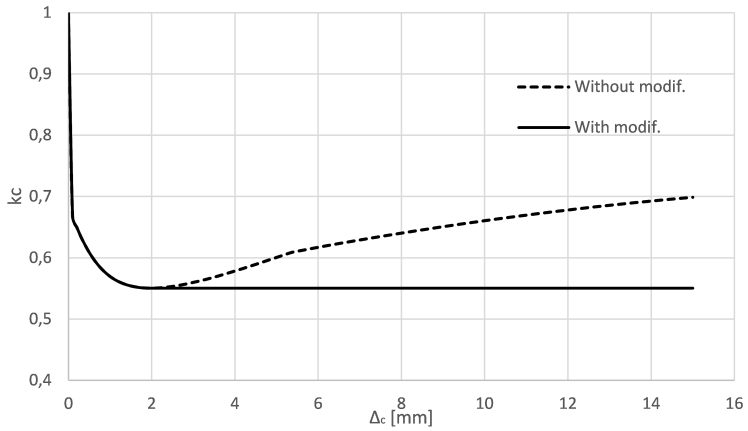

Figure 36: Evolution of k_c as a function of Δ_c

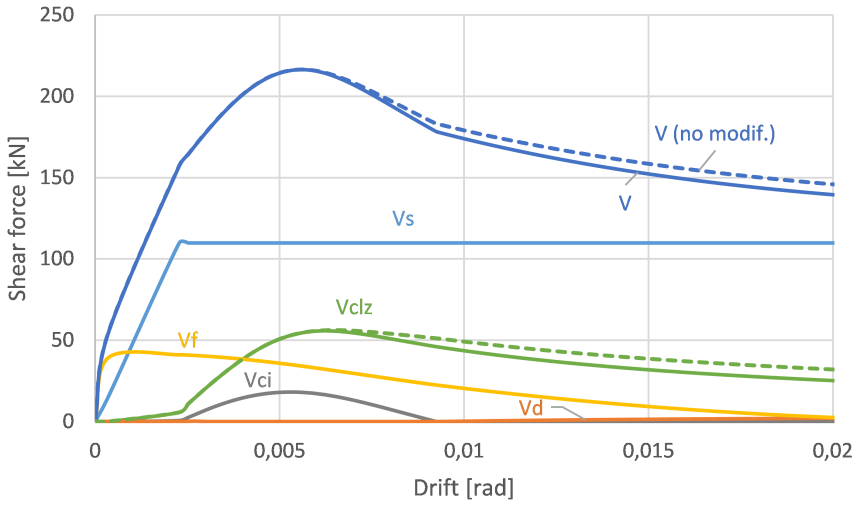

Figure 37: Load-drift curve with modification of k_c

Figure 37 illustrates the load-drift curve in the case of the coupling beam. The dotted blue line represents the total shear force without the modification of k_c and the dark blue line represents the total shear force when accounting for a modification of k_c. It can be seen that the effect only happens in the post-peak region where the shear force is slightly decreased. This modification only affects V_{CLZ} which is depicted in green on the figure (dotted line for the case without modification).

4.6 Averaging of the crack width

In the model developed by Tvrznikova (2017), the component V_F is calculated based on crack width. The crack width considered for this calculation is located at the middle of the diagonal crack. Then, thanks to the SDEM method, the tensile stresses supported by the fibres are estimated and considered constant on the main diagonal crack. However, it is very unlikely for the crack width to be constant on the whole diagonal and therefore, tensile stress in the fibres cannot be constant either. A Matlab code is provided in Appendix A.

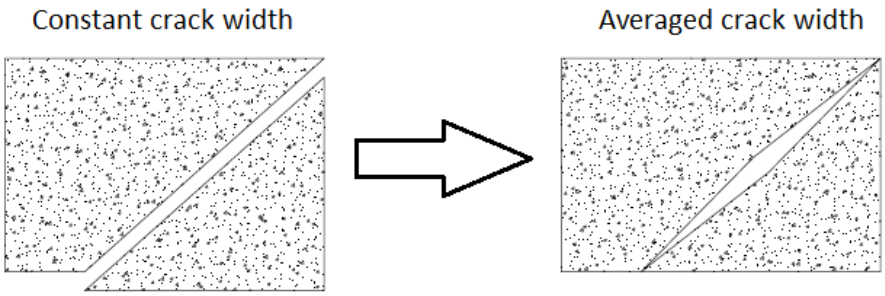

Figure 38: Modification of the crack width

In order to estimate the most accurately possible the total force supported by the fibres, it can be assumed that the crack width at the ends of the diagonal is zero and varies linearly to the middle of the diagonal crack where the crack width is equal to what has been calculated from equation (26) as can be seen in Figure 38. In this case the whole stress-strain relationship from the SDEM is needed to estimate the tensile stress in the fibres at each point of the diagonal crack. Alternatively, a mean tensile stress can be calculated by integrating this stress-strain relationship. This method is similar to what has been done for the evaluation of σ_{avg} in the critical loading zone. For a given crack width at the middle of the shear span w_m, the area under the curve Ω_m is given by:

$$\Omega_m(w_m) = \int_0^{w_m} f_f dw \approx \sum_i \frac{f_f(w_i) + f_f(w_{i-1})}{2(w_i - w_{i-1})} \tag{74}$$

and the average tensile stress in the fibres is given by:

$$f_{f,avg} = \frac{\Omega_m(w_m)}{w_m} \tag{75}$$

Based on this value, the force V_F can be calculated as:

$$V_F = \frac{f_{f,avg} bd}{\sin \alpha_1} \cos \beta \tag{76}$$

Figure 39 illustrates the effect of the averaging of the crack width on the different components of the shear resistance. It can be seen that this modification only impacts the curve V_F depicted in yellow (dotted line without modifications and solid line line with the averaging). This curve is drawn for a given $\Delta_c = 5\ mm$ which corresponds to the post-peak domain. The effect here is positive as the resistance is increased. The dark blue line depicts the total shear resistance (dotted line for the curve without averaging and solid line with averaging). The resistance is simply increased by a constant value. It is also important to note that V_{CLZ}, which is depicted in green, is not constant in Figure 39 although it was the case in the extended 2PKT. This is because of the softening of concrete considered in this model. Indeed, as the average tensile strain in the top reinforcement increases, the concrete becomes more softened and cannot provide as much resistance as for a small tensile strain in the top reinforcement layer. This is the reason why V_{CLZ} decreases with increasing $\epsilon_{t,avg}$.

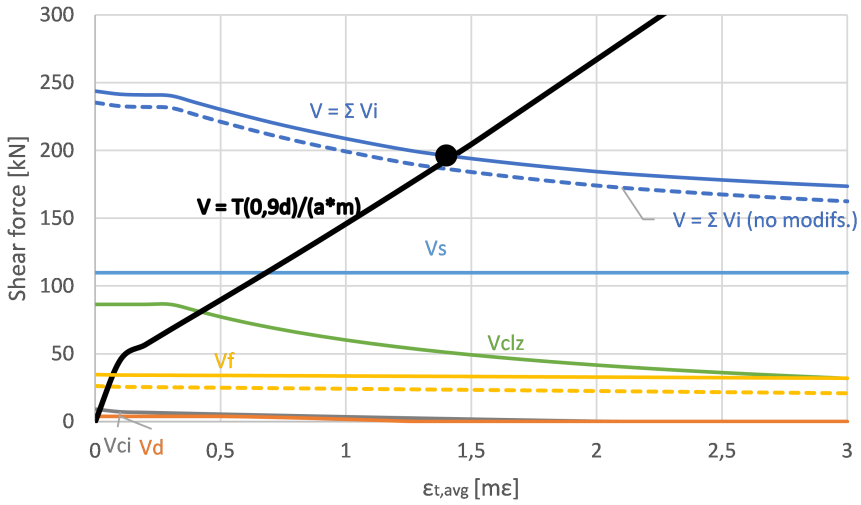

Figure 39: Effect of crack averaging for a given $\Delta_c = 5\ mm$

Figure 40 shows the full load-drift curve for the sample specimen considered. The shear resistance is depicted in dark blue (dotted line for the curve without averaging and solid line with averaging). The resistance in the post-peak domain is increased but the resistance in the pre-peak region is decreased. This is due to the modification of V_F depicted in yellow (dotted line for the curve without averaging and solid line with averaging). With small displacement, the averaging of crack width results in decrease of the resistance provided by the fibres. This is due to the shape of the stress-strain curve for fibres calculated from the SDEM as shown in Figure 21. Since the averaging consists of integrating the stress-strain relationship, it results in lower tensile stress if the crack width calculated from the SDEM in lower than the crack width at which f_f reaches its maximum ($w_{cr,max}$). However, for values of crack width larger than $w_{cr,max}$, the averaging results in an increased tensile stress because of the decreasing behaviour of the stress-strain relationship of the fibres.

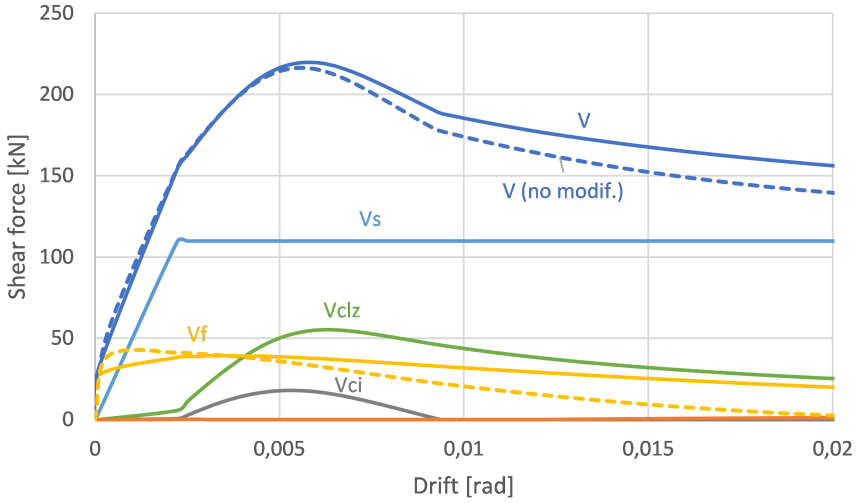

Figure 40: Effect of crack averaging on the full load-drift curve

4.7 Pull-out behaviour of the bars

The pull-out of the bars embedded in the concrete matrix is important when an accurate estimation of the displacement is needed. This effect becomes important in bars subjected to high tension forces in concrete. Since the 3PKT aims to study the effect of both bottom and top layers of reinforcement, it is relevant to study the effect of bar pull-out in the case of coupling beams. This effect has been studied by many researchers and one of the most adapted models for the bar pull-out has been developed by Harajli (2004). The current approach to study the pull-out behaviour is to normalise the bond strength between reinforcing bars and concrete to the square root of the concrete compressive strength f'_c (ACI 1999a,b). Experimental studies conducted by Azizinamini et al. (1993) found out that high strength concrete (HSC) reduces the normalised average bond strength at failure as compared to normal strength concrete (NSC). This effect was attributed to the increased bearing capacity of concrete which increases the resistance of concrete against crushing and thus stiffens the response of the bar slip. This results in the concentration of bond forces in a few lugs at the loaded bar end which increases the concrete tensile stresses and leads to premature splitting failure (Harajli, 2004). Harajli (2004) developed an analytical evaluation of the average bond strength at failure based on experimental studies for both NSC and HSC. The procedure was based on a numerical scheme in order to find a relationship between the bar slip in concrete and the bond stress. Based on several parameters, the bond stress-slip curve can be determined for each case as shown in Figure 41. The horizontal axis represents the bar slip (noted s) while the vertical axis represents the bond stress (noted u). The study performed by Harajli shows two different types of failure: Pull-out failure and Splitting failure. A Matlab code is provided in Appendix B.

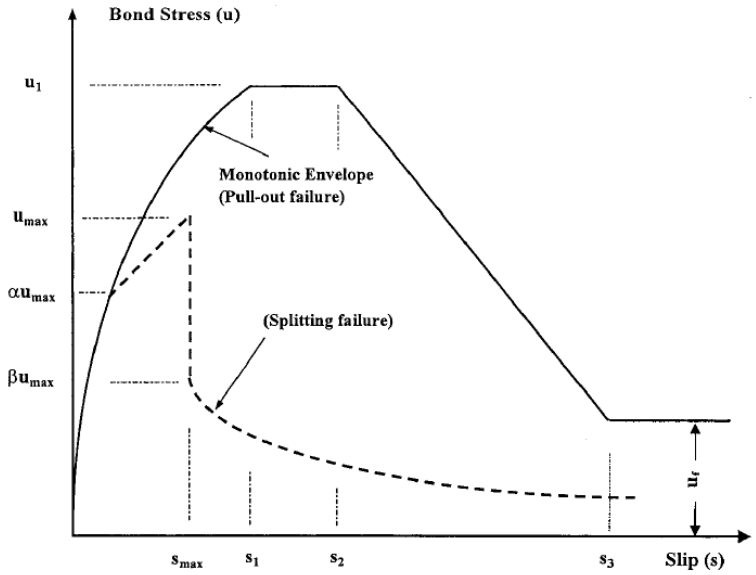

Figure 41: Local bond stress-slip model for plain normal strength concrete and high strength concrete (Harajli, 2004)

The ascending part of the thick black curve (pull-out failure) can be determined by (Harajli et al., 1995):

$$u = u_1 \left(\frac{s}{s_1} \right)^{0.3} \tag{77}$$

where u_1 is the maximum bond stress that can be attained and is given by: $u_1 = 2.57\sqrt{f'_c}$, and s_1 is the bar slip at $u = u_1$ and is taken as 1.5 mm if there is no information is given about the bar deformation properties. After the ascending part, the monotonic envelope remains at constant bond stress until the bar slip reaches s_2 which is equal to 3.5 mm. The descending straight part of that curve is given by:

$$u = \frac{u_1 - u_f}{s_2 - s_3}(s - s_2) + u_1 \tag{78}$$

where u_f is the residual bond stress and is given by $u_f = 0.35u_1$, and $s_3 = 10mm$.

The splitting failure envelope is not be studied in this thesis. Indeed, the model does not provide any way to predict if the failure of any specimen will be a pull-out failure or a splitting failure.

Implementation in the model

In order to implement the pull-out effect in the model, a 1-dimensional finite element model is required. The goal of this implementation is to find the additional displacement due to the pull-out of bars caused by the tension in the reinforcement. The tension in the reinforcement layers is calculated by the extended 3PKT model and is equal to T. Given that force, the slip is calculated thanks to the model proposed by Harajli (2004). The FEM model consists of a bar divided into n-1 elements linked by springs connected in series which represent the elastic behaviour of the bars. Additionally, another spring is associated with each node to represent the bond behaviour between rebar and concrete. The FEM model is shown in Figure 42. The total number of nodes is equal to n.

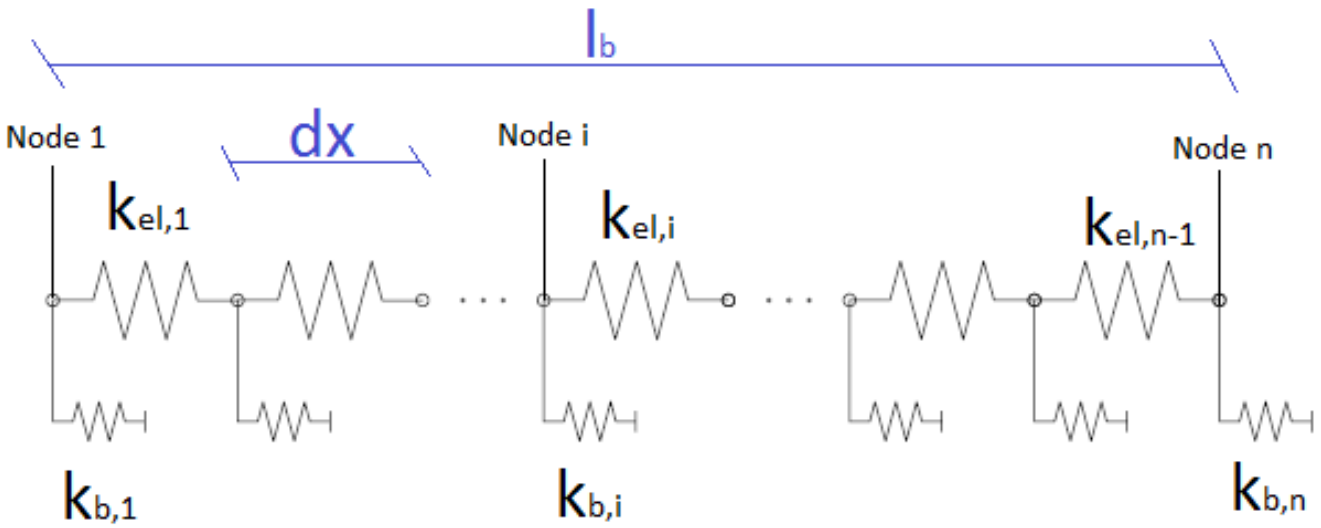

Figure 42: FEM model for the pull-out behaviour

The bond length l_b represents the length of the bar embedded in the shear wall. In order to have sufficient accuracy, the bar must be divided into small linear elements which have a length equal to dx. $k_{el,i}$ represents the stiffness of the spring that models the elastic behaviour of the bar. Therefore, a yielding of the reinforcement cannot be considered in this model. For each element, the elastic stiffness is given by:

$$k_{el,i} = \frac{E_s A_s}{dx} \tag{79}$$

Moreover, each node is restrained by a spring that represents the bond between concrete and bars. The bond stiffness $k_{b,i}$ is calculated based on the bond stress-slip model from Harajli (2004). Since the stiffness depends on the slip s which is given by the displacement of the node, the solution to this problem needs to be iterated. The most simple method to find the bond stiffness from the stress-strain curve is the secant method. By assuming a first stiffness, if the force is known, the corresponding displacement

can be estimated. With this new displacement, an updated stiffness can be calculated and a new value of displacement as well. This procedure is repeated until convergence of the stiffness is reached. It can be seen in Figure 43 that for an applied stress of 14 MPa (which is deduced from the applied force), the final result (black dot) is found with a rather few amount of iterations. The stiffness $k_{b,i}$ is given by the slope of the final secant.

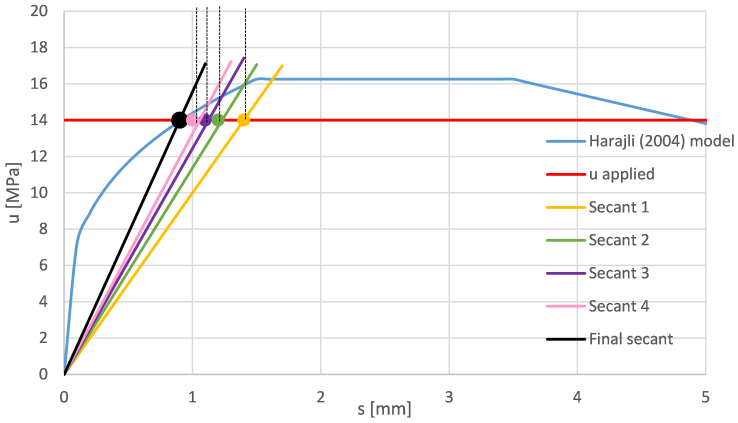

Figure 43: Secant method example

At end nodes, it can be considered that the bond area is equal to half the bond area for other nodes. Indeed, the length on which the tensile force acts at end nodes is equal to $dx/2$. Therefore, we have:

$$k_{b,1} = k_{b,n} = k_{b,i}/2 \tag{80}$$

and the bond stress acting on each node is equal to:

$$u_i = \frac{T}{n_b d_b \pi dx} \text{ for } i \in]1, n[\tag{81}$$

and

$$u_1 = u_n = \frac{T}{n_b d_b \pi dx/2} \tag{82}$$

Since the bond stress-slip curve from Harajli (2004) has an infinite slope for $s \approx 0$, the convergence is not assured for small slip values. Therefore, for values of $s < s_1/1000$ the curve from Harajli is assumed to vary linearly from 0 to $s_1/1000$ between $u(0) = 0$ MPa and $u(s_1/1000) = u_1(1/1000)^{0.3}$ MPa.

Solution of the problem

The problem is solved by the following equation:

$$\{F\} = [K]\{\Delta^p\} \tag{83}$$

where $\{F\}$ is the force vector, $[K]$ is the stiffness matrix and $\{\Delta^p\}$ is the displacement vector which represents the displacement of each node. Considering that the external tension force T is applied at node n, the force vector is given by:

$$\{F\} = \begin{Bmatrix} 0 \\ 0 \\ \vdots \\ 0 \\ \vdots \\ 0 \\ T \end{Bmatrix} \tag{84}$$

The displacement field is unknown and has to be calculated. Concerning the stiffness matrix, it is composed of an elastic part ($[K_{el}]$) and bond part ($[K_b]$). $[K_{el}]$ consists of the stiffness matrix composed by the springs in series. From analysis, it is given by:

$$[K_{el}] = \begin{bmatrix} k_{el,1} & -k_{el,1} & 0 & \dots & & 0 \\ -k_{el,1} & k_{el,1}+k_{el,2} & -k_{el,2} & 0 & \dots & 0 \\ 0 & -k_{el,2} & k_{el,2}+k_{el,3} & -k_{el,3} & 0 & \vdots \\ 0 & 0 & -k_{el,3} & \ddots & \ddots & 0 \\ \vdots & \ddots & 0 & \ddots & k_{el,n-2}+k_{el,n-1} & -k_{el,n-1} \\ 0 & \dots & & 0 & -k_{el,n-1} & k_{el,n-1} \end{bmatrix} \tag{85}$$

The bond stiffness matrix has a simple from as each node has its own spring which acts on one node only. Therefore, $[K_b]$ is diagonal and is given by:

$$[K_b] = \begin{bmatrix} k_{b,1} & 0 & \dots & & 0 \\ 0 & k_{b,2} & 0 & \ddots & \vdots \\ 0 & 0 & k_{b,3} & 0 & \\ \vdots & \ddots & 0 & \ddots & 0 \\ 0 & \dots & & 0 & k_{b,n} \end{bmatrix} \tag{86}$$

Finally, because of the scheme adopted for the FEM analysis, the total stiffness matrix $[K]$ is equal to the sum of the two stiffness matrices:

$$[K] = [K_{el}] + [K_b] \tag{87}$$

The method used to find the pull-out of any bar is to solve the following equation for displacement:

$$\{\Delta^p\} = [K]^{-1}\{F\} \tag{88}$$

For a given value of tension force T, the equation is able to find the displacement field in the bar after convergence of the matrix $[K]$ is reached. The procedure is repeated for several values of T and the tension-slip curve can be generated. Afterwards, the tension-slipt curve for the shear response of the coupling beam is modified thanks to the previous calculations. For any value of shear V is associated a tension force T. From the tension-slip curve of the pull-out mechanism, a bar slip can be associated with T and is added to the total displacement of the coupling beam.

However, because of the bond stress-slip relationship from Harajli (2004), the tension-slip curve that can be determined from the 1D FEM analysis will be incomplete. Indeed, the tension-clip curve will have a post-peak domain which cannot be determined by this method. Moreover, it is impossible to predict for which value of slip this peak will be observed. Therefore, another method can be used.

The other method relies on imposing the last component of the vector $\{\Delta^p\}$. This component is supposed to be the total bar slip that is needed in order to plot the tension-slip curve. By imposing this component, any point of the curve can be determined. All the other components of $\{\Delta^p\}$ are however unknown. This method relies on finding the tension force that corresponds to the bar slip s. In order to use the same equations as before, a simple trick can be used. By writing the last equation of the system (83), we have:

$$T = K_{n1}\Delta_1^p + K_{n2}\Delta_2^p + ... + K_{nn-1}\Delta_{n-1}^p + K_{nn}\Delta_n^p \tag{89}$$

Let us write $T = K_{max}\Delta_n^p$, where $K_{max} = 10^6$ is a fictional stiffness taken sufficiently large and $Delta_n^p$ is unknown by the procedure but should be equal to s. Hence,

$$\Delta_n^p = \frac{K_{max}K_{nn}s - K_{n1}\Delta_1^p - K_{n2}\Delta_2^p - ... + -K_{nn-1}\Delta_{n-1}^p}{K_{max}K_{nn}} \tag{90}$$

and therefore, if $K_{max}K_{nn} >> K_{ni}\Delta_i^p$:

$$\Delta_n^p \approx s \tag{91}$$

This approach allows to find the tension force T for any value of bar slip s provided that in the iteration process on the matrix $[K_b]$, the component K_{nn} is replaced by $K_{max}K_{nn}$. For example, 2 bars with a 20 mm diameter embedded in concrete with a compressive strength $f_c' = 40$ MPa and a bond length of 500 mm, the tension-slip response is given in Figure 44. The curve shows a typical post-peak behaviour that resembles the bond stress-slip relationship from Harajli (2004). However, in this case, only the ascending part of the curve is selected because with one tension force comes only one displacement. It is assumed that in the analysis of coupling beams, the post-peak domain of Figure 44 is never attained.

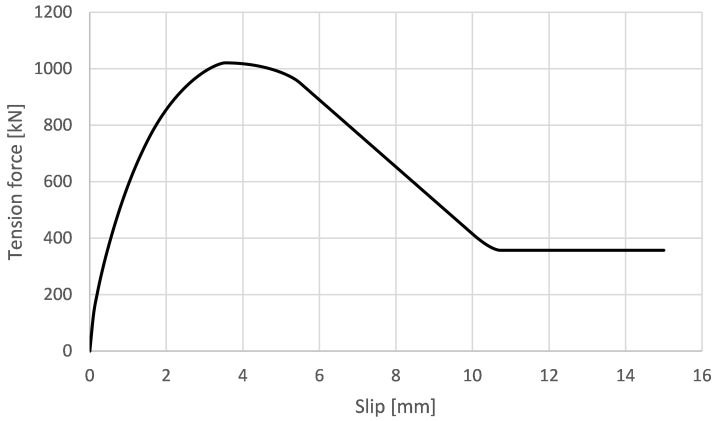

Figure 44: Tension-slip curve (example)

In order to account properly for the effect of pull-out, the additional drift angle α_p must be calculated considering the movement induced by pull-out separately from the rest. Therefore, the coupling beam can be considered as a rigid block rotated by an angle α_p. The movement of the rigid block is shown in Figure 45. The block is considered to rotate as a rigid block but crushed zones of the CLZ are considered. The

length l_p between the end of a crushed zone and the opposite layer of reinforcement is supposed to be a fraction of the reinforcement depth. It is assumed that $l_p \approx 0.8d$. From geometry in Figure 45, the angle of rotation due to the pull-out of the bars can be estimated as:

$$\alpha_p = \arcsin \frac{s}{l_p} \tag{92}$$

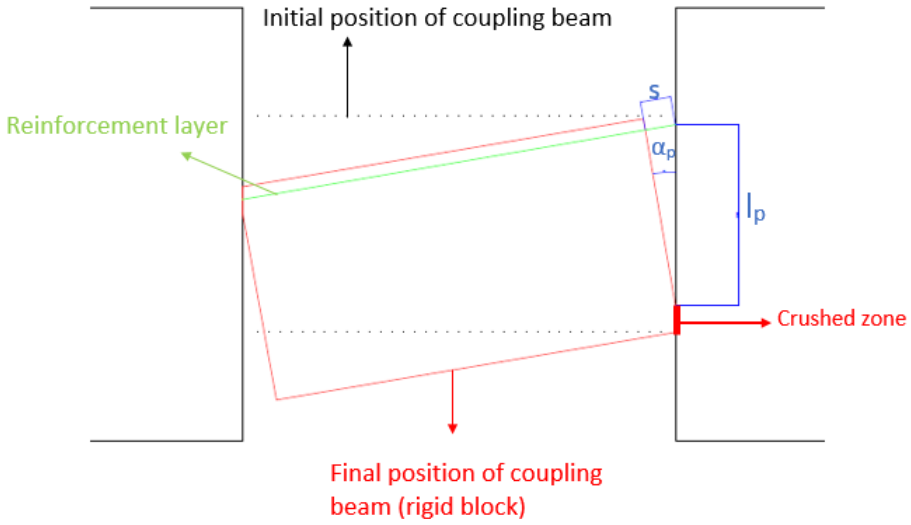

Figure 45: Rotation of the coupling beam due to pull-out (rigid block)

The effect of pull-out is shown in Figure 46 on the full load-drift curve of the sample specimen which has a bond length equal to 575 mm. The difference between the two resulting curves is clear (dotted lines for the case without pull-out and solid lines for the case with pull-out). The effect of pull-out results in a shift of the curves to the right (greater drift) as expected but it does not affect the total resistance although the peak is attained for larger deformations. At peak load, the additional angle α_p is equal to 0.0011 rad which correspond to an increase of the initial drift of 19 %. The pull-out effect is therefore non-negligible.

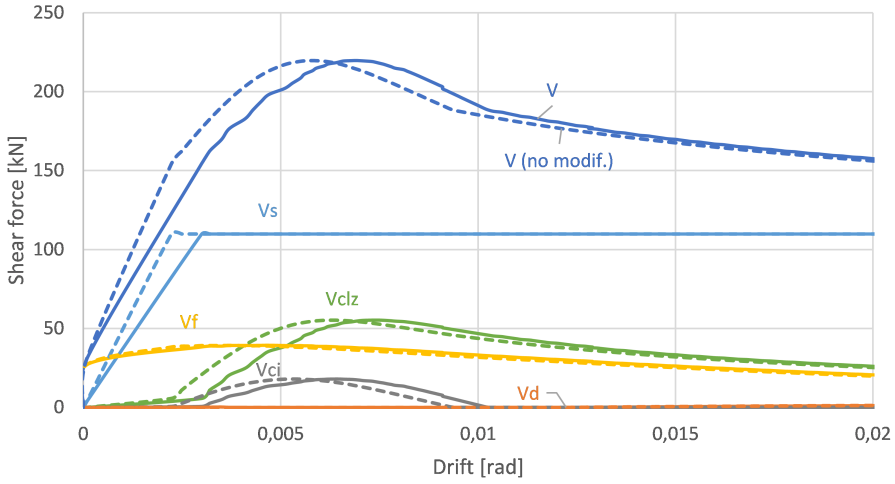

Figure 46: Effect of bar pull-out on the load-drift curve

4.8 Effect of restraint

Although the original 3PKT method is not able to account for an axial restraint of the beam, this effect can be easily modelled. Indeed, a restraint can be modelled by setting the longitudinal reinforcement strain $\epsilon_{t,avg}$ to zero. If the reinforcement does not become longer, the coupling beam does not elongate and it acts as an axial restraint. An easy way to force $\epsilon_{t,avg}$ to be equal to zero is to increase sufficiently the amount or reinforcement in the top and bottom layers.

Therefore, this modification is applied in the code by increasing the area of steel reinforcement except for the dowel effect calculation. Indeed, the dowel effect is not influenced by the axial restraint and increasing the area of steel reinforcement would increase the shear resistance provided by the dowels which is not physically acceptable.

This effect can be studied on the sample beam even if the latter is not axially restrained. Figure 47 shows the contribution of all forces for a given $\Delta_c = 5\ mm$. The solid thick black line represents the shear force calculated from moment equilibrium with the modified area of longitudinal reinforcement while the dotted thick black line represent the same shear force but with the actual area of reinforcement. It can be seen that the new intersection represented by the big black dot is found at $\epsilon_{t,avg} \approx 0$.

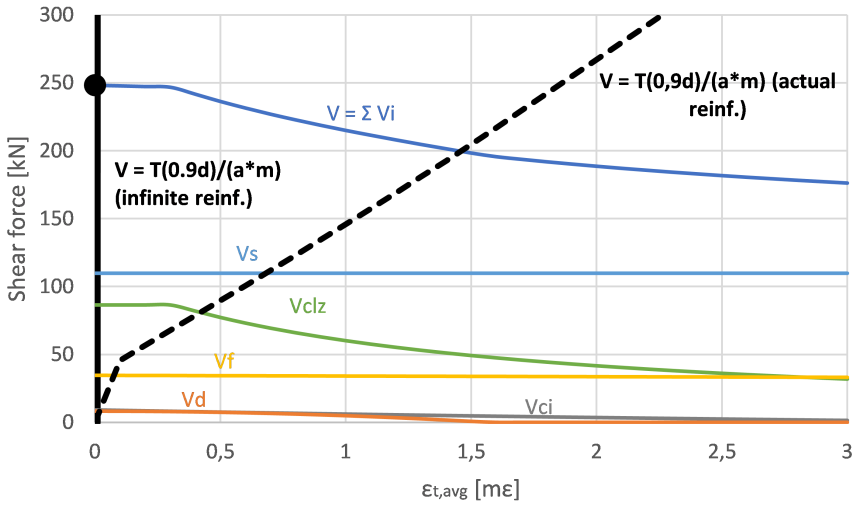

Figure 47: Effect of restraint for a given $\Delta_c = 5\ mm$

Figure 48 shows the full load-drift curve for the sample beam. Solid lines represent the shear forces that account for the restraint effect while dotted lines represent the shear forces without this effect. It can be seen that except for the contribution of fibres, all forces are increased and show an increased stiffness. As a result, the load-drift curve of the restrained sample specimen shows higher resistance and higher stiffness.

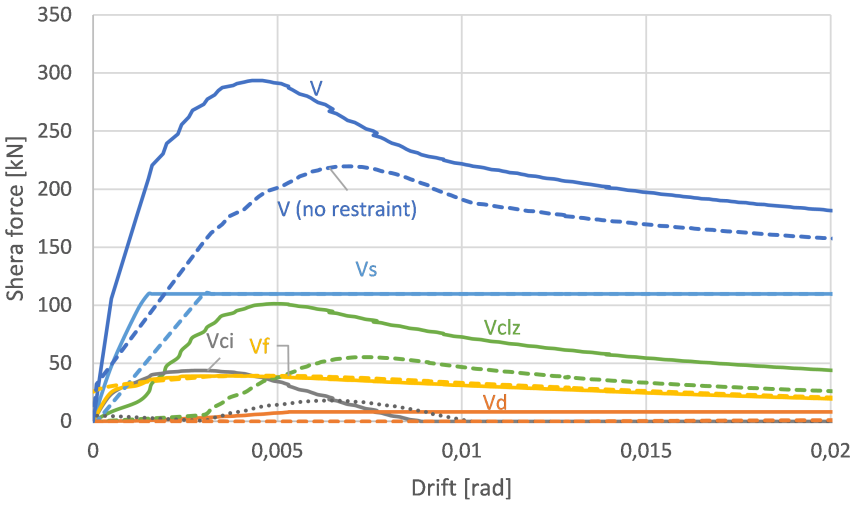

Figure 48: Effect of restraint on the full load-drift curve

5 Finite Element Modelling

This section presents a finite element method (FEM) analysis performed on tests from the database. The selected tests are first described and then results from FEM analysis are discussed in terms of failure load and load-drift curve predictions.

5.1 Selected tests

The FEM analysis is more complex and more time consuming than the extended 3PKT analysis. The test setup must be simple to implement into the finite element software. In this regard, the support conditions must be easy to model.

All test setups from the database can be selected as they are sufficiently simple to model in the software. However, some tests exhibited yielding of the longitudinal reinforcement and thus do not allow for comparison with the extended 3PKT as the latter does not consider yielding of the longitudinal reinforcement.

Table 7 summarises the tests chosen for the finite element analysis and the results from the experiments and numerical tests.

Beam name	a/d	ρ_l [%]	f_y [MPa]	ρ_v [%]	f_{yv} [MPa]	f'_c [MPa]	Fibre type	f_{uf} [MPa]	V_f [%]	l_f [mm]	d_f [mm]	V_{exp} [kN]
CCB3-30-2-1FS	2.32	1.21	363.4	0.56	295.6	40.5	Straight	380	1.0	32	0.76	227
CCB3-40-2-1FS						43.1						238
CCB3-50-2-1FS						52.9						243
CCB3-60-2-1FS						66.7						250
CCB3-70-2-1FS						70.1						253
CCB3-80-2-1FS						80.7						255
CCB3-40-1-1FS	1.16	1.21	363.4	0.56	295.6	43.1	Straight	380	1.0	32	0.76	295
CCB3-40-1.5-1FS	1.74											292
CCB3-50-2-0FS	2.32	1.21	363.4	0.56	295.6	55.63	Straight	380	0	32	0.76	202.5
CCB3-50-2-0.5FS						54.49			0.5			238
CCB3-50-2-1FS						54.8			1.0			244
CCB3-50-2-1.5FS						55.92			1.5			249.5
CCB3-50-2-2FS						55.31			2.0			255.5
S-10/M	1.11	2	469	1	384	37.52	Hook-ended	1000	1.0	50	1.05	298.6
S-15/M	1.67			1		38.16						281.5
S-20/M	2.22			1		38.72						262.2
S-15/W	1.67			0		44.96						130.0
S-15/S	1.67			2		45.2						357.7

Table 7: Selected specimens for finite element modelling

5.2 Description of the finite element models

In order to model the test setups from the different experiments, the same rules are adopted for each of the tests. As of example, a model from Gaochuang et al.'s test series is shown in Figure 49. The model shown in the figure is CCB3-40-2-1FS. Table 8 describes the properties in terms of width, concrete compressive strength, smeared longitudinal and transverse reinforcement and fibre information.

The material 4 shown in Figure 49 is a steel plate connected to the concrete rigid blocks. The imposed horizontal displacement here is to force the upper rigid block to move horizontally but to have no rotation of to and have a free vertical movement of the block. The pin supports represent the steel connection. The lower rigid block can therefore not move if it is sufficiently rigid. The two rigid blocks are highly reinforced in the two main directions in order for them to have sufficient rigidity relative to the coupling beam. The stirrups in the coupling beam are assumed to spread in between the top and bottom layers of longitudinal reinforcement. This modification is done so that the concrete in the corners of the coupling beam does not resist too much shear. Indeed, it would be the case if transverse reinforcement was implemented in that location in the FEM model and it would not be realistic (material 2 in Figure 49).

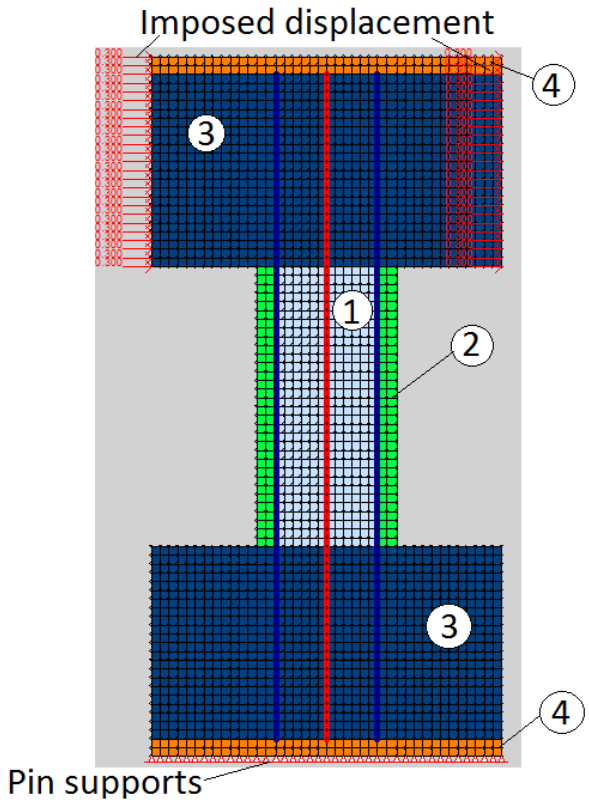

Figure 49: FEM model for Gaochuang et al.'s series

Material number	b [mm]	f'_c [MPa]	ρ_l [%]	ρ_v [%]	V_f [%]
1			0	1	1
2	150	43.1	0	0	1
3			2	2	0

Table 8: Material properties for the FEM model for specimen CCB3-40-2-1FS

5.3 General assumptions

- The first rule adopted in the FEM modelling is the smearing of the transverse reinforcement in the beams. This method is adopted for all specimens and it concerns coupling beams as well as rigid blocks. The program allows to distribute the reinforcement in each element in the transverse

direction. After testing, it has been found that the failure load and the failure mode are not affected by this simplification.

- The rigid blocks have smeared reinforcement in the two principal directions in order for them to be rigid enough in the deformation (or loading) process. They are designed with a reinforcement ratio of 2 % in each direction. Authors from different experiments pointed out that the rigid blocks did not play a role in the failure of coupling beams and this hypothesis can therefore be considered relevant. Results from FEM analysis confirm such a hypothesis.
- The transverse reinforcement of coupling beams is not present beyond the top and bottom layers of reinforcement because it is anchored in those two locations.
- The longitudinal reinforcement is perfectly anchored in the two rigid blocks.
- The strength enhancement of concrete due to confinement is neglected. The confinement of concrete occurs when concrete is under compression in both principal directions which does not happen during any test.
- The tension softening model is considered to be exponential as advised by the VecTor2's user's book for FRC members.
- Cyclic loading is not considered due to the complexity of analysis and thus, only monotonic loading is considered. However, a modified SDEM model that accounts for cyclic effects is considered to model the behaviour of fibres for cases where the experiment was performed with cyclic loading. The displacement increment applied to the specimen corresponds to about 2 % of the final observed displacement.
- The mesh used to model the specimen is composed of elements whose size has been limited to 25x25 mm. This decision is made to obtain results with sufficient precision in a limited time.
- The FEM software is able to use straight or hook-ended fibres. Straight fibres are used for Gaochuang et al.'s series while hook-ended fibres are selected for Kuang and Baczkowski's series.
- Steel plates with very high stiffness are added at each end of the rigid blocks. This allows not to have high concentration of stresses in corner nodes of the rigid blocks.

5.4 Test setup for Gaochuang et al.

The test setup from Gaochuang et al. allows them to have a displacement controlled experiment. Moreover, the two end blocks cannot rotate and there is no axial restraint. Therefore, the upper end block moves laterally (imposed displacement) and vertically (free displacement). These conditions can be easily adopted by the model by applying a horizontal displacement at each node on the right and left sides of the upper end block. The lower end block is supposed to be strongly fixed to the floor. Given the assumption that the latter is sufficiently rigid thanks to additional reinforcement, each node of its lower side is supported by a pin connection. An example for specimen CCB3-40-2-1FS is shown in Figure 49. Another solution to this problem is to model the steel truss from the experiment. However, after testing, results from both tests are extremely close and the first option is selected due to its simplicity of implementation in the program. Figure 50 shows the deformations of the top end block before and after testing. It is clear that the block has not rotated and that it has moved vertically.

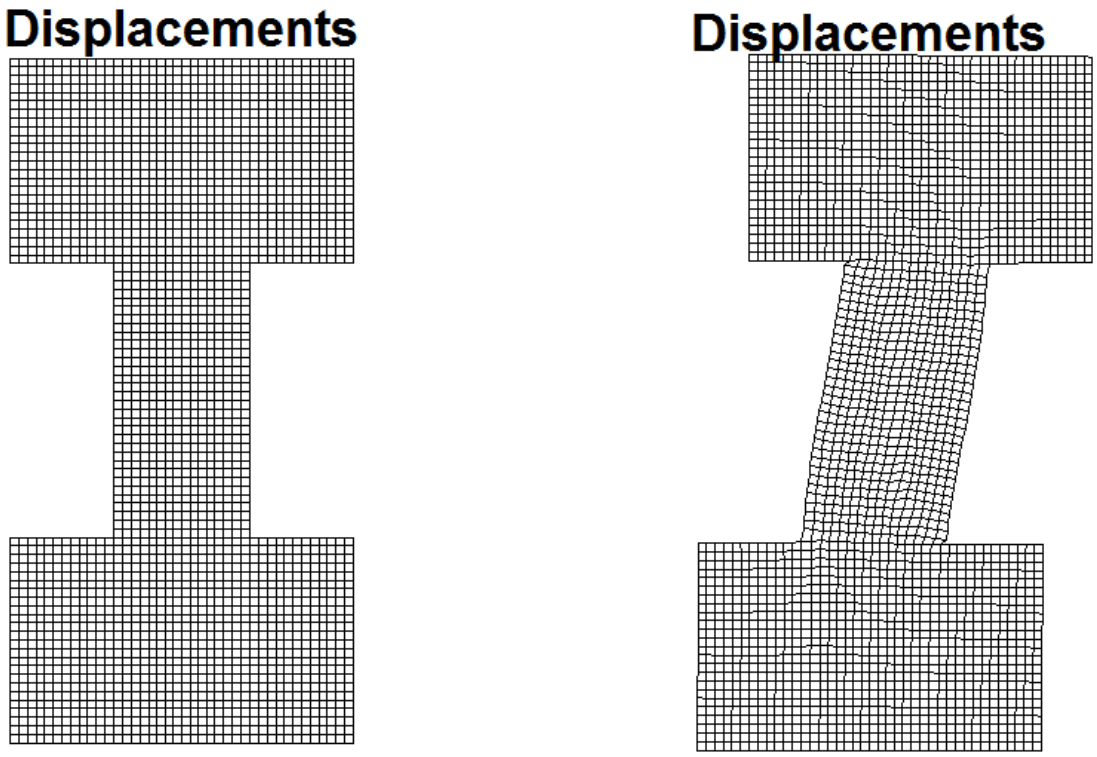

(a) Before loading (b) After loading (at failure)

Figure 50: Effect of support conditions on Gaochuang et al.'s test series

5.5 Test setup for Kuang and Baczkoswki

In their test setup, axial displacement of the coupling beam is restrained but the rotation of the two end blocks is equal. Therefore, considering a rotation of the system 90°, if the lower end block is considered fixed to the floor on its lower face as for Gaochuang et al.'s series, the upper end block cannot rotate either because it has to rotate by the same amount as the lower end block. Therefore, the same test setup as for Gaochaung et al.'s can be used. However, the axial restraint must be implemented. In order to do so, the upper end block is connected to horizontal rollers which allow for horizontal displacement of the end block while preventing free vertical displacement. The idealised boundary conditions for the test setup can be seen in Figure 51. It should be emphasised though that the papers from Kuand and Baczkowski (2006 and 2009) do not mention anything about the axial restraint. Nonetheless, from the test setup shown in Figure 51, it is likely that the axial movement of the coupling beam is not totally free.

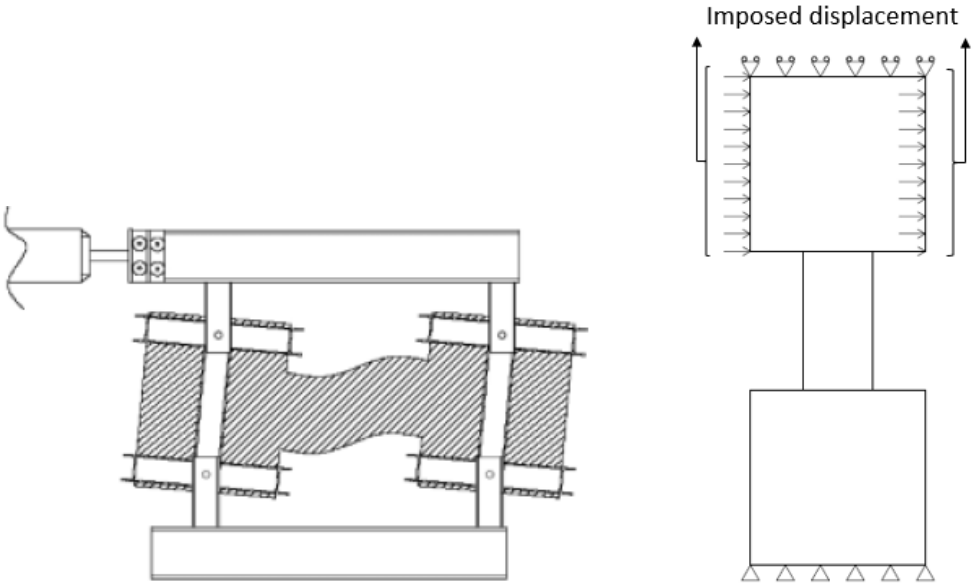

(a) Scheme of test setup (b) Idealised boundary conditions

Figure 51: Test setup by Kuang and Baczkowski

5.6 Discussion of the results

5.6.1 Gaochuang et al.'s series

Test on CCB3-40-2-1FS

The specimens from Gaochuang et al. were tested based on the finite element method with good accuracy for all of them. In order to proceed to a general analysis, only one beam is studied here. The beam is CCB3-40-2-FS has an experimental failure load of 238 kN as reported by the authors of the paper. Analysis from VecTor2 reveals that the predicted failure load is equal to 225.6 kN which marks an error of 5 %.

Moreover, the program is able to represent the crack pattern at each stage of the loading as shown in Figure 52(a) where red lines represents cracks and wider cracks are represented by thicker lines. It looks from that figure that the failure mode is not well estimated. Indeed, the failure mode reported from Gaochuang et al. is a shear-tension failure and therefore, a diagonal crack should be observed from the figure. In this case, wider cracks appear on the edges of the coupling beams and the failure mode is thus not well estimated.

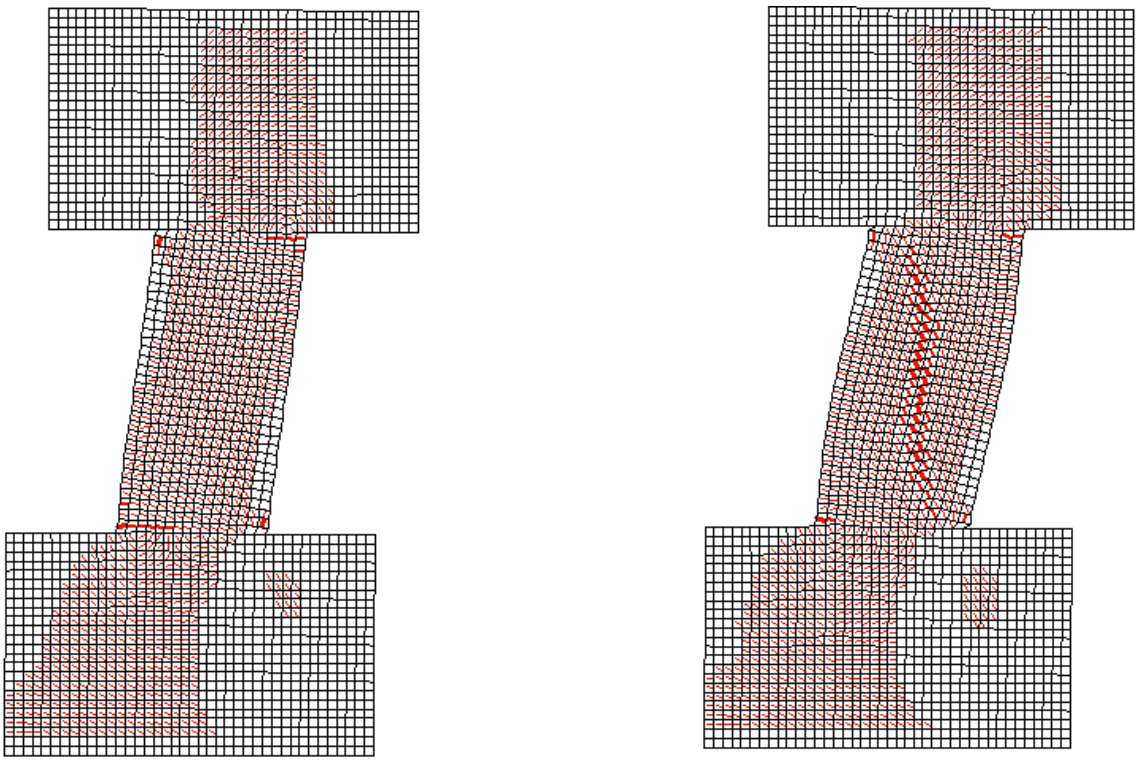

(a) Actual yield strength

(b) Modified yield strength

Figure 52: Crack pattern of beam CCB3-40-2-1FS at failure for different yield strengths of longitudinal reinforcement

In order to force a diagonal tension failure mode in the finite element program, the yield strength of the longitudinal reinforcement can be increased by 100 % for example. The crack pattern shown in Figure 52(b) clearly illustrates a shear-tension failure as wider cracks appear on the main diagonal and thus, the failure mode is well estimated. However, the failure load of the member estimated by this FEM analysis is equal to 253.9 kN which exceeds the experimental shear strength by 7 %. Although this may seem close to the experiment in this case, the procedure from this analysis was performed for all the tests from Gaochuang et al. and it was found that the first method of FEM analysis exhibited better results in terms of shear strength evaluation. Therefore, the actual yield strength of the longitudinal bars was selected. This method was chosen in order to be consistent with the experiments. Figure 53 shows the different FEM methods and compares them to the experimental data. It can be observed that the FEM method that used an increased yield strength (FEM model 2) is more brittle than the other method (FEM model 1).

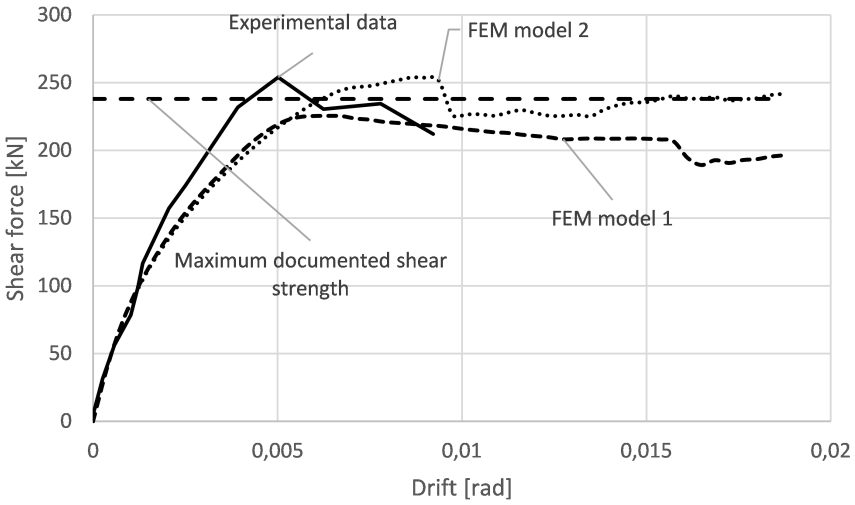

Figure 53: Comparison of different FEM models on the full load-drift curve for beam CCB3-40-2-1FS

Failure Loads

Failure loads from experiments by Gaochuang et al. (2016) are first described. The first series consists of testing the effect of the compressive strength of concrete on the ultimate shear strength. All these beams have a span-to-depth ratio equal to 2.32, a compressive strength ranging from 40.1 MPa to 80.7 MPa and a fibre volume ratio of 1 %. Figure 54 shows the results of the FEM analysis compared to the experimental results where the vertical axis represents the failure load and the horizontal axis represents the concrete compressive strength.

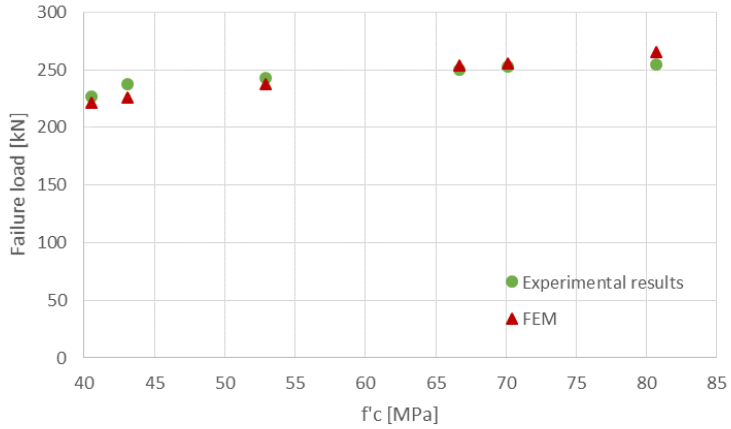

Figure 54: FEM results for Gaochuang et al's first series

It can be observed from Figure 54 that the finite element analysis captures quite well the effect of the concrete compressive strength on the ultimate shear strength of coupling beams. The average error for all tests is equal to 2.7 % which is very low.

The second series of beams evaluated the effect of the span-to-depth ratio. Out of five tested beams, three are selected in this analysis because the other two do not agree with the selection criteria. These specimens had a span-to-depth ratio ranging from 1.16 to 2.32, a compressive strength of 43.1 MPa and a

fibre volume ratio of 1 %. Results from FEM analysis are shown in Figure 55. The vertical axis represents the failure load and the horizontal axis is the span-to-depth ratio which is called a/d.

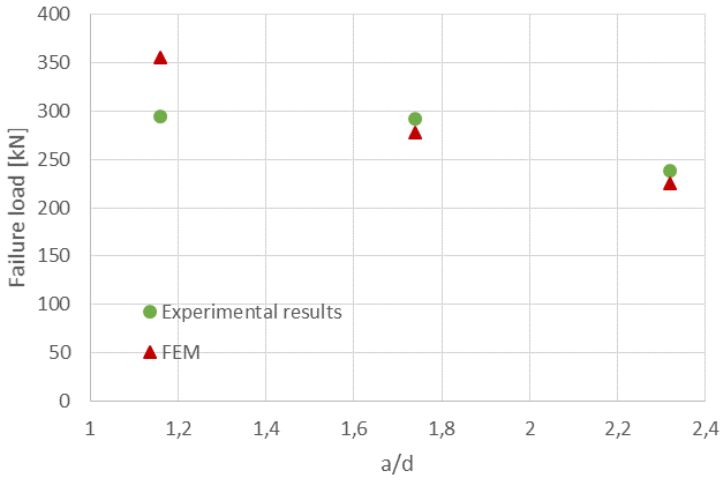

Figure 55: FEM results for Gaochuang et al's second series

Results from this FEM analysis are less good than for the first series since the average error is equal to 10 %. This is mainly due to the first test for which the error of the FEM analysis is equal to 20.4 % while the other two tests exhibit an error of 4.7 % and 5.2 % for $a/d = 1.74$ and $a/d = 2.32$, respectively. Conclusions cannot be made on the ability of the FEM analysis to capture the effect of the span-to-depth ratio because the number of data points is too low.

The last series of beams evaluated the effect of fibre volume ratio. Out of six specimens, 5 were selected and tested. These beams had a fibre volume ratio ranging from 0 % to 2 %, a compressive strength of 55 MPa and a sapn-to-depth ratio equal to 2.32. Figure 56 shows the results from FEM analysis. The vertical axis represents the failure load and the horizontal axis is the fibre volume ratio expressed in %.

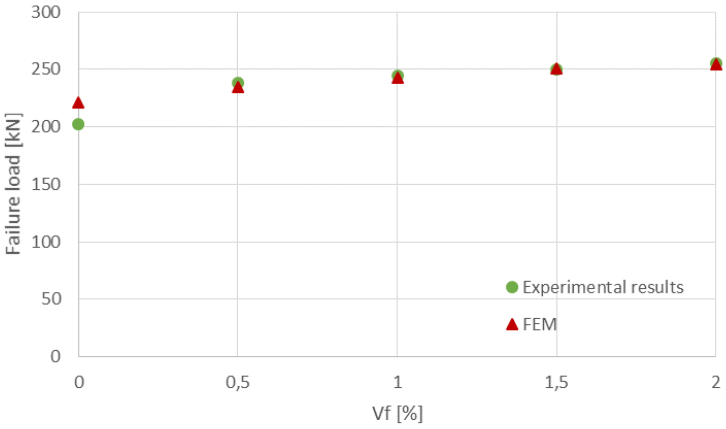

Figure 56: FEM results for Gaochuang et al's third series

Conclusions can be made on the results from FEM analysis that it captures well the influence of the fibre volume ratio on the ultimate shear strength of coupling beams. Indeed, the average error is equal to 2.4 %.

Load-drift curves

Load-drift curves selected from Gaochuang et al.'s experiments are five curves provided by the authors. These five curves are represented in Figure 57 with the FEM curves for comparison. It can be seen that the curves match closely the reality in term of shear strength. However, the initial stiffness of beams CCB3-50-2-0.5FS and CCB3-50-2-1.5FS is overestimated by the FEM analysis. This may be caused by some additional displacement that happened during the experiment. Indeed, all tests from the third series by Gaochuang et al. have a very low stiffness compared to tests from the other series.

It can be observed that the finite element analysis results exhibit a more brittle behaviour for all tests except for test CCB3-40-2-1FS which shows a ductile behaviour while the experimental result was more brittle. However, in their experimental program, Gaochuang et al. stopped the experiment in the post-peak domain after a load below 85 % of the peak load was reached for safety of installation and researchers. Thus, there might be a more ductile response of the member after the peak has been reached. Overall, it can be said however that the load-drift response is rather similar to the experiment in term of behaviour for most of the experiments.

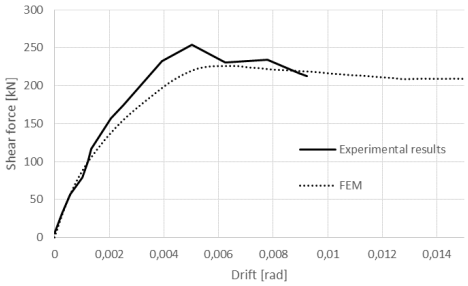

(a) CCB3-40-2-1FS

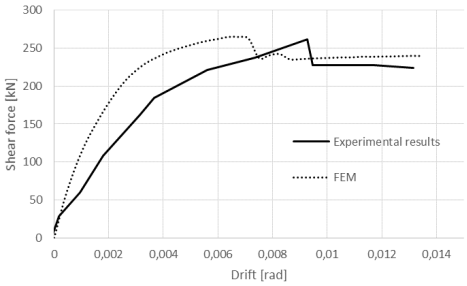

(b) CCB3-80-2-1FS

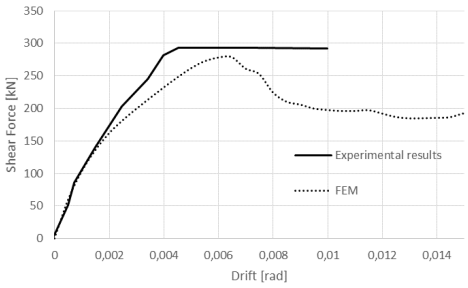

(c) CCB3-40-1.5-1FS

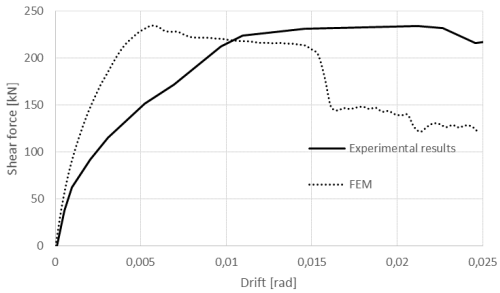

(d) CCB3-50-2-0.5FS

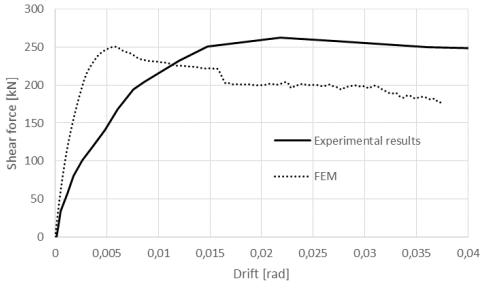

(e) CCB3-50-2-1.5FS

Figure 57: Load-drift curves: FEM Vs Experimental data

5.6.2 Kuang and Baczkowski's series

Kuang and Backowski tested two parameters apart from the effect of fibre volume ratio which are the span-to-depth ratio (frist series) and the transverse reinforcement ratio (second series). Specimens from the first series had a span-to-depth ratio ranging from 1.11 to 2.22, a compressive strength of about 38 MPa and a transverse reinforcement ratio of 1 %. Specimens from the second series had a span-to-depth ratio of 1.67, a transverse reinforcement ratio ranging from 0 % to 2 % and a compressive strength of about 45 MPa except for the specimen with a transverse reinforcement ratio which had a compressive strength of 38 MPa.

It can be observed that the FEM analysis does not match closely the results from the experiments as shown in Figure 58a and Figure 58b. Moreover, results are unconservative.

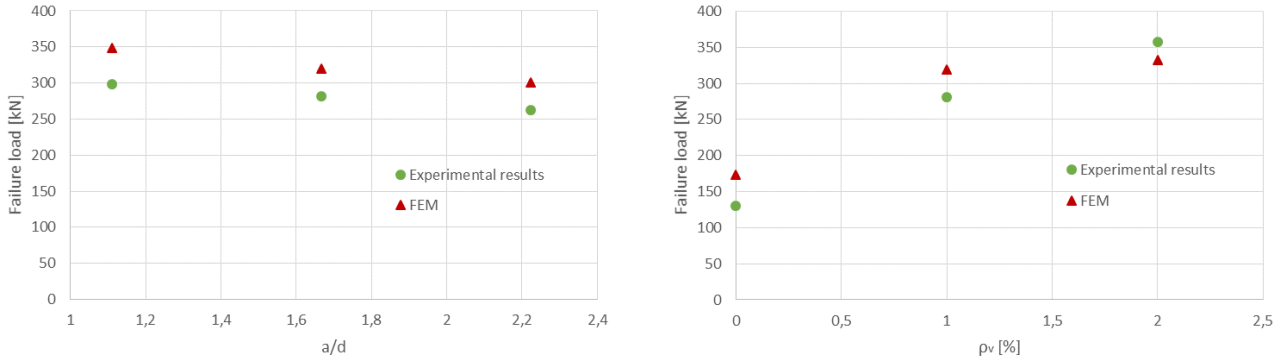

(a) First series

(b) Second series

Figure 58: FEM results for Kuang and Baczkowski's experiments

Tests from Kuang and Baczkowski did not match experimental results also for load-drift curves. As of example, one curve is shown in Figure 59. It can be seen that FEM analysis results are far from reality in terms of stiffness and shear strength. Because of this reason, tests from Kuang and Baczkowski will not be further analysed and they will not be used for validation. Indeed, boundary conditions may have been not correctly estimated and therefore, no comparison can be made with experimental results.

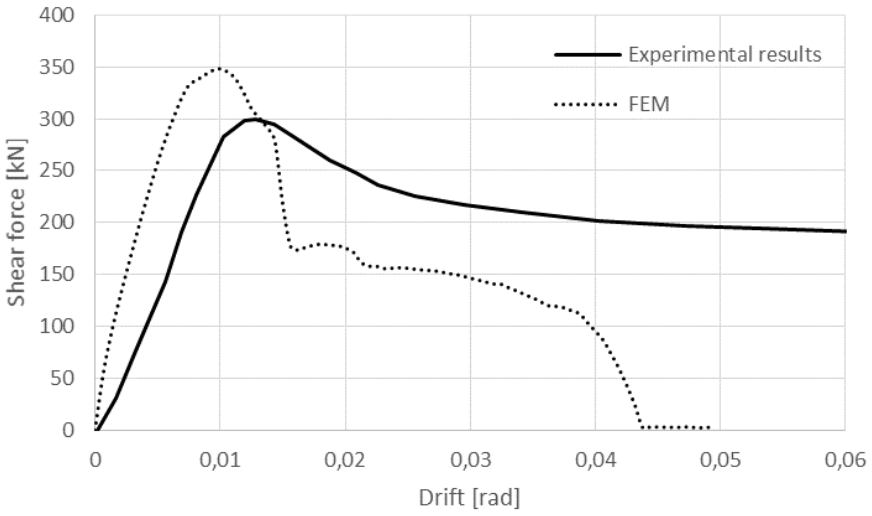

Figure 59: Load-drift curves for test S-10/M by Kuang and Baczkoswki

6 Validation of the extended 3PKT model

The developed model in this thesis is validated against experimental data. One experiment is considered to validate the model which is the one by Gaochuang et al. (2016). In their experiment, they varied the concrete compressive strength, the span-to-depth ratio and the volume of fibres. These three parameters will be studied in this section.

In the end, results of the comparisons are discussed and also compared to results obtained from FEM analysis.

6.1 Sample specimen evaluation

In order to validate the proposed extended 3PKT model, one representative specimen was selected among the 17 tests available from experiments by Gaochuang et al.. In their experiment, they varied the span-to-depth ratio from 1.16 to 2.32. From these specimens, CCB3-40-2-1FS was selected. This specimen has a span-to-depth ratio of 2.32, a fibre volume ratio of 1% and a compressive strength of 43.1 MPa. It has a width of 150 mm, a length of 800 mm and a height of 400 mm. The transverse reinforcement is composed of 8 mm diameter bars spaced by 120 mm. The longitudinal reinforcement is composed of 3 layers. The top layer located at a depth of 345 mm is composed of 2 bars with a 20 mm diameter while the middle layer is located at the mid-height of the section and is composed of 2 bars with a 10 mm diameter. The bottom layer is the same as the top layer but located at the other end of the section. The transverse reinforcement ratio is equal to 0.56 % while the longitudinal reinforcement ratio is equal to 1.21 %. Fibres used in this experiment are straight and have a length of 32 mm and a diameter of 0.76 mm. Their ultimate tensile strength is equal to 380 MPa. The two end blocks are composed of conventional reinforced concrete. Their width is equal to 150 mm as well. Results from experimental data, FEM analysis and experimental data are depicted in Figure 60.

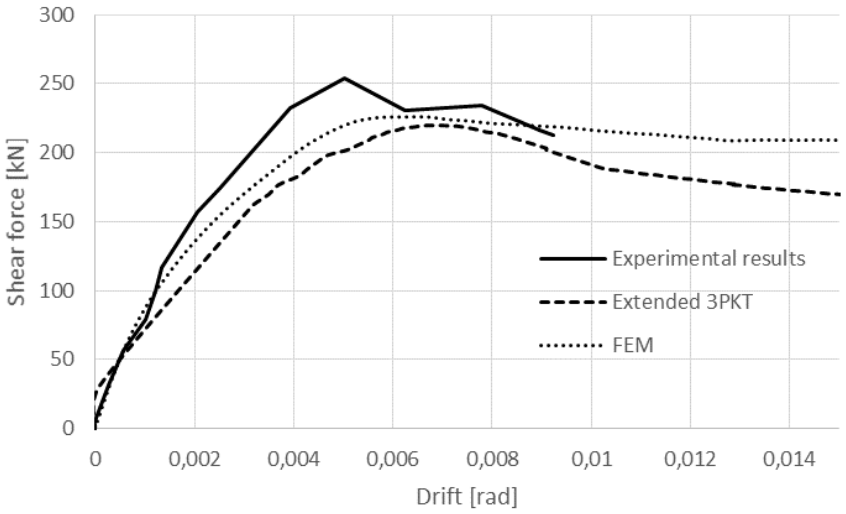

Figure 60: Comparison of load-drift curves for beam CCB3-40-2-1FS from extended 3PKT model, FEM model and experimental data from Gaochuang et al. (2016)

It can be observed in Figure 60 that the shear strength calculated from the extended 3PKT model is a little bit more conservative than the shear strength obtained from the experiment. The finite element method gives here a result than matches a bit more closely the reality in term of strength even though the position of the peak is not the same as for the experiment. The extended 3PKT model finds the peak strength for a higher drift than the FEM model but the drift at peak found from FEM analysis is still

bigger than in the experiment. Therefore, it is plausible that there has been additional deformation during the experiment such as settlement of supports due to high compression forces applied to the beam.

6.2 Effect of the span-to-depth ratio

In the experiment, Gaochuang et al. (2016) tested 6 specimens with different span-to-depth ratio. Out of these 6 specimens, three only are selected because the other three tests have a span-to-depth ratio greater than 2.5 which are not considered in this thesis. The sample specimen is considered to have the properties of beam CCB3-40-2-1FS listed in Table 9.

a/d	b [mm]	d [mm]	h [mm]	m	ρ_l [%]	ϕ_l [mm]	*No. bars*	f_y [MPa]	a_g [mm]	f'_c [MPa]	f_{yv} [MPa]	ρ_v [%]	ϕ_v [mm]	f_{uf} [MPa]	V_f [%]	l_f [mm]	d_f [mm]
2.32	150	345	400	0.5	1.21	20	2	363.4	10	43.1	295.6	0.56	8	380	1.0	32	0.76

Table 9: Sample specimen properties for validation of the model

The validation is performed by changing the a/d ratio of the sample beam. Results from extended 3PKT analysis are shown in Figure 61. The horizontal axis describes the a/d ratio which varies from 1.0 to 2.5 with an increment step of 0.1. The vertical axis is the maximum shear force estimated by the model for the considered span-to-depth ratio. On the same graph are plotted results from the experimental program and FEM analysis. Analysis performed by the proposed model agrees very well with experimental results. It is also more conservative than results obtained from FEM analysis which provides also accurate results except for the lowest a/d ratio. It can be seen from Figure 61 that the effect of span-to-depth ratio mostly influences the shear strength provided by the critical loading zone (CLZ). Moreover, the aggregate interlock is also affected by the span-to-depth ratio but in a less significant way. Similarly to the effect of the CLZ, as a/d increases, the shear resistance provided by the aggregate interlock decreases. The inclusion of fibres increases the shear strength by a rather constant value for all a/d ratios.

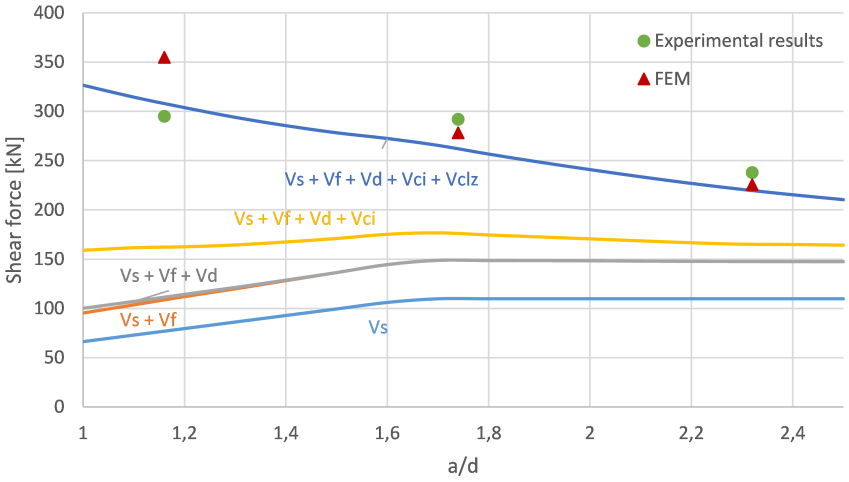

Figure 61: Effect of span-to-depth ratio on the ultimate shear strength

In conclusion, the total shear resistance of the coupling beam increases as the span-to-depth ratio decreases thanks to the additional shear resistance provided by the CLZ and the aggregate interlock.

6.3 Effect of fibre volume ratio

The effect of fibre volume ratio is validated based on specimen CCB3-50-2-0.5FS performed by Gaochuang et al. (2016). They performed a test series which comprised 6 specimens with a fibre volume ratio going from 0 to 2.5 %. The last specimen (with 2 %) fibre volume ratio is not considered in this analysis. All the specimens have the same properties as specimen CCB3-40-2-1FS (Table 9) except for the fibre volume ratio and the concrete compressive strength which was about 55 MPa for all specimens. From the experiments, it was concluded that an increased fibre content resulted in increased ultimate and cracking strengths of the coupling beams. These tests are verified with the extended 3PKT analysis and FEM analysis depicted in Figure 62. It shows the ultimate shear strength of members with a fibre volume content from 0 % to 2% with an increment step of 0.1 % and compares the results to the experiments and FEM models.

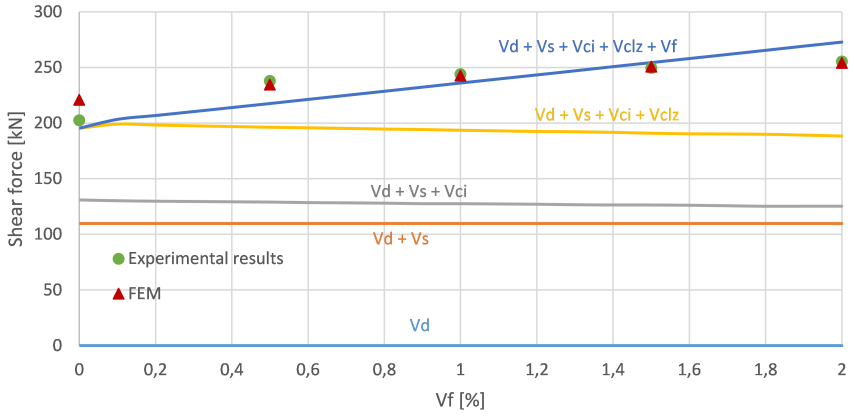

Figure 62: Effect of fibre volume ratio on the ultimate shear strength

It can be observed that the shear strength of coupling beams increases as the fibre volume ratio increases. This effect provided by the component V_F is linear. The addition of fibres has no effect on the other components except for the CLZ component which is slightly lower for higher fibre volume ratios but its effect is negligible. Based on the experiments, the extended 3PKT model provides more conservative values than the FEM analysis especially for fibre volume ratios lower or equal than 1 %. For higher fibre volume ratios, the FEM model seems more accurate and also more conservative. It can be concluded that in general, the extended 3PKT model captures quite well the effect of the fibres on the shear strength of coupling beams.

6.4 Effect of concrete compressive strength

The last parameter that Gaochuang et al. (2016) tested is the compressive strength of concrete. They tested 6 different specimens with a compressive strength ranging from 40.5 MPa to 80.7 MPa. All their other properties are the same as for the sample beam taken for the evaluation of the effect of span-to-depth ratio (Table 9). Therefore, the effect of compressive strength of concrete is also based on the sample specimen from Table 9. Gaochuang et al. (2016) concluded that an increased compressive strength of concrete (which results in an increased tensile strength of concrete) resulted in an increased ultimate strength of coupling beams. Figure 63 illustrates the effect of the compressive strength on the ultimate shear strength of coupling beams. The ultimate shear strength is calculated based on the extended 3PKT model for a varying concrete compressive strength ranging from 35 MPa to 85 MPa with an increment step of 5 MPa. Finally, results are compared to experimental results and FEM analysis.

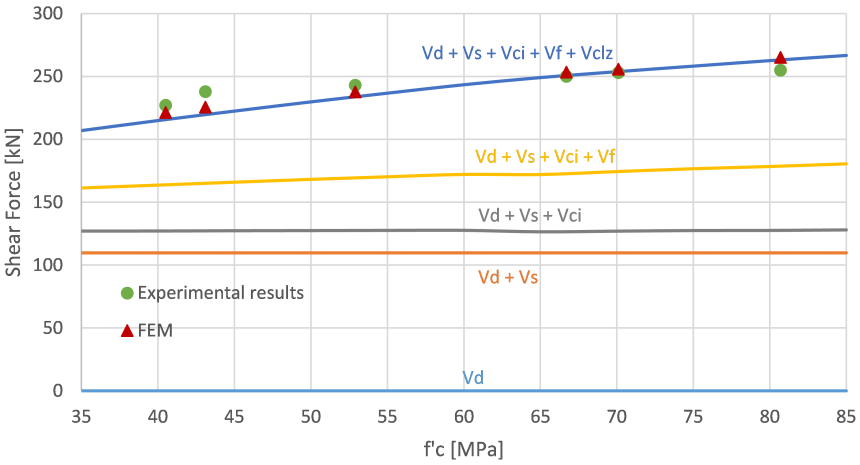

Figure 63: Effect of concrete compressive strength on ultimate shear strength

It can be seen that the increase in concrete compressive strength results in an increased shear strength as predicted. This effect is mainly due to the shear resistance provided by the critical loading zone which increases as f'_c increases. In this study, results from FEM analysis and extended 3PKT are very close to the experimental results. Again, the extended 3PKT model captures well the effect of the concrete compressive strength on the ultimate shear provided by coupling beams.

6.5 Summary of validation studies

Failure load

Table 10 summarises the results from the extended 3PKT analysis and FEM analysis. It can be seen that both methods provide very good estimation of the failure load. Indeed, a coefficient of variation of 5.29 % or 6.02 % is very low when determining a failure load, especially for a shear failure. Moreover, the extended 3PKT method provided more conservative results than the FEM analysis although it is much faster to use.

Beam name	a/d	ρ_l [%]	f_y [MPa]	ρ_v [%]	f_{yv} [MPa]	f'_c [MPa]	Fibre type	f_{uf} [MPa]	V_f [%]	l_f [mm]	d_f [mm]	V_{exp} [kN]	$\frac{V_{exp}}{V_{3PKT}}$	$\frac{V_{exp}}{V_{FEM}}$
CCB3-30-2-1FS	2.32	1.21	363.4	0.56	295.6	40.5	Straight	380	1.0	32	0.76	227	1.05	1.03
CCB3-40-2-1FS						43.1						238	1.05	1.05
CCB3-50-2-1FS						52.9						243	1.04	1.02
CCB3-60-2-1FS						66.7						250	1.00	0.99
CCB3-70-2-1FS						70.1						253	1.00	0.99
CCB3-80-2-1FS						80.7						255	0.97	0.96
CCB3-40-1-1FS	1.16	1.21	363.4	0.56	295.6	43.1	Straight	380	1.0	32	0.76	295	0.96	0.83
CCB3-40-1.5-1FS	1.74											292	1.11	1.05
CCB3-50-2-0FS	2.32	1.21	363.4	0.56	295.6	55.63	Straight	380	0	32	0.76	202.5	1.03	0.92
CCB3-50-2-0.5FS						54.49			0.5			238	1.09	1.01
CCB3-50-2-1FS						54.8			1.0			244	1.03	1.01
CCB3-50-2-1.5FS						55.92			1.5			249.5	0.97	0.99
CCB3-50-2-2FS						55.31			2.0			255.5	0.93	1.01
												Average	1.02	0.99
												COV [%]	5.29	6.02

Table 10: Results from extended 3PKT and FEM analysis

Load-drift curve

Load-drift curves from the same experiments as for the finite element model analysis are represented in Figure 64. It can be observed that the load-drift curves match very well the results found from FEM analysis. Therefore, similar conclusions to what had been observed from FEM analysis can be made. The post-peak behaviour found from extended 3PKT analysis however is a bit more brittle. In the case of beam CCB3-80-2-1-FS, a typical shear failure can be observed from extended 3PKT analysis as from FEM analysis, a ductile behaviour is observed.

Moreover, for beams CCB3-50-2-0.5FS and CCB3-50-2-1.5-FS, the initial stiffness seems to be overestimated as it has been observed from FEM analysis. This confirms that there may have been additional displacement or error in displacements measurements by the researchers.

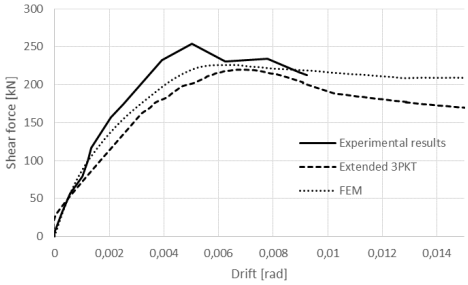

(a) CCB3-40-2-1FS

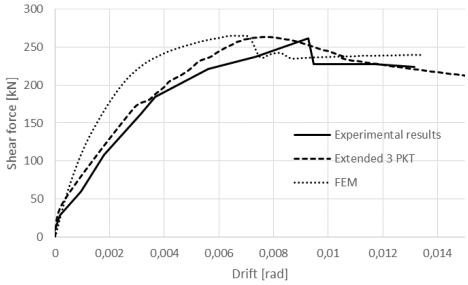

(b) CCB3-80-2-1FS

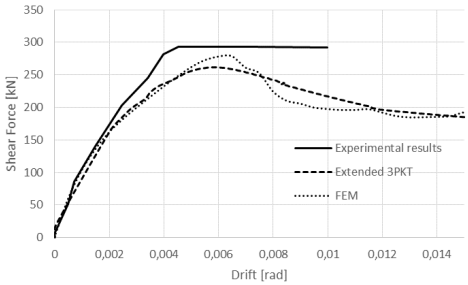

(c) CCB3-40-1.5-1FS

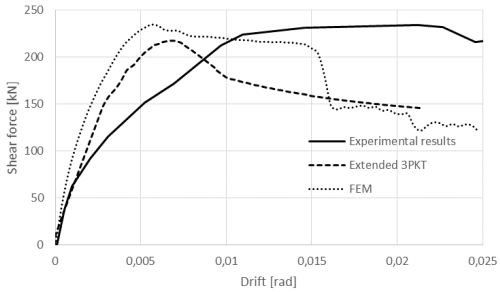

(d) CCB3-50-2-0.5FS

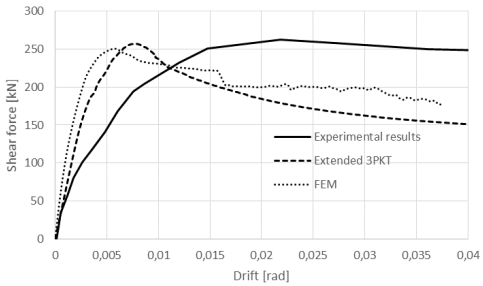

(e) CCB3-50-2-1.5FS

Figure 64: Load-drift curves: FEM Vs Experimental data

6.6 Parametric study

In order to study the effect of several parameters influencing the extended 3PKT model, a parametric study was carried out. First, a sample beam was created. The beam properties are based on the experimental program from Gaochuang et al. (2016) with some changes. The sample beam properties are shown in Table 11.

a/d	b [mm]	d [mm]	h [mm]	m	ρ_l [%]	ϕ_l [mm]	$No.$ $bars$	f_y [MPa]	a_g [mm]	f'_c [MPa]	f_{yv} [MPa]	ρ_v [%]	f_{uf} [MPa]	V_f [%]	l_f [mm]	d_f [mm]
2	150	350	400	0.5	1.20	20	2	400	10	40	400	0.5	380	1.0	30	0.7

Table 11: Sample specimen properties for the parametric study

Variables investigated are the span-to-depth ratio, effect of longitudinal reinforcement, concrete compressive strength, fibre volume ratio, transverse reinforcement ratio and size effect. Each parametric study was performed by changing one or several variables of the sample beam while all the others remained identical to the properties described in Table 11. In some cases, the parametric study was performed for three different fibre volume ratios which are 0 %, 1 % and 2 %.

6.6.1 Span-to-depth ratio

First, the effect of a/d ratio is investigated. It ranges from 1.0 to 2.5 with an increment step of 0.1. At each step, the shear strength of the member is plotted. This effect is studied for three different fibre volume ratios: 0 %, 1 % and 2 %. In order to study adequately the effect of the fibres on the shear strength of the member, no transverse steel reinforcement is considered.

Results from this analysis are shown in Figure 65. The horizontal axis describes the a/d ratio and the vertical axis describes maximum values of shear resistance provided by the extended 3PKT model for each value of a/d. For all cases of fibre volume ratio, a gradual decrease in shear strength can be observed as a/d increases and thus, the most resistant member is in all cases the one with the smallest a/d ratio. The least resistant member is the one with the largest a/d ratio and it drops by 54 % for the coupling beam without fibres, 52.5 % for 1 % of fibres and 49 % for 2 % of fibres. Therefore, with higher fibre inclusion comes a slightly lower impact of the span-to-depth ratio.

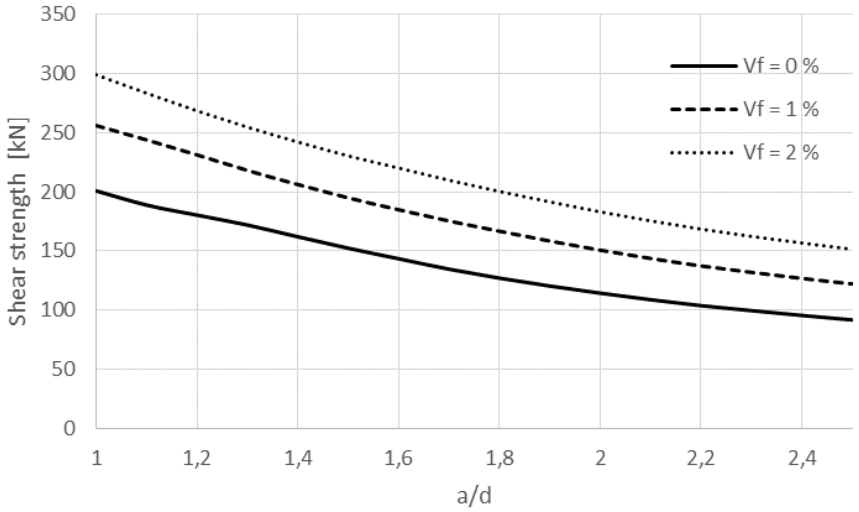

Figure 65: Effect of span-to-depth ratio for different fibre volume ratios

The effect of fibre volume ratio on the shear strength can also be evaluated. Figure 65 proves that the inclusion of fibres leads to an increase in shear strength of the coupling beam. For $a/d = 0.5$, the shear strength increases by 28 % for 1 % of fibres when compared to the case without fibres, and by 49 % for 2 % fibre volume ratio. Moreover, the difference becomes more significant when the span-to-depth ratio is higher. Indeed, for $a/d = 2.5$, the shear strength increases by 33 % when compared to the case without fibres, and by 66 % for 2 % of fibres.

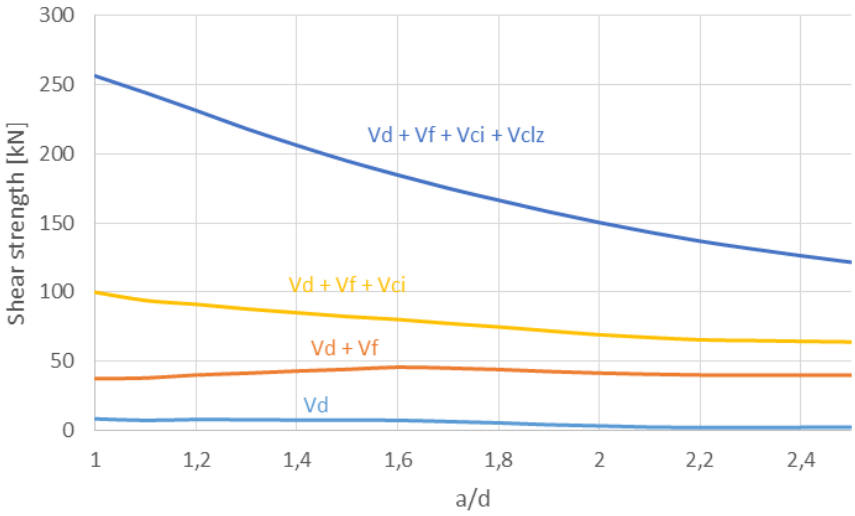

Figure 66: Breakdown of the effect of a/d for $V_f = 1$ %

Figure 66 illustrates the breakdown of the forces contributing to the total shear resistance of the member for a fibre volume ratio of 1 %. It can be observed that the decreasing tendency of the shear resistance with an increasing span-to-depth ratio is mainly due to the contribution of the critical loading zone (CLZ). This decreasing tendency is due to the fact that, as a/d increases, the size of the CLZ decreases. The smaller size of the CLZ with increasing a/d can be explained with the equation of the CLZ from the original 3PKT model. In this model, V_{CLZ} is proportional to the characteristic length l_{b1e} and $\sin^2\alpha$. As a/d increases, l_{b1e} increases but $\sin^2\alpha$ decreases. Overall, the effect of $\sin^2\alpha$ is dominant and the size of the CLZ decreases as well as the vertical component of the shear force in the CLZ. Additionally, the aggregate interlock is also affected by the a/d ratio as its contribution also decreases with increasing a/d ratio. The effect of fibres remains overall constant for all span-to-depth ratios. Therefore, its effect is more significant for cases where a/d is high because the total strength is reduced by the aggregate interlock and the CLZ. The fibres thus, reduce slightly the decreasing tendency of the curve.

6.6.2 Longitudinal reinforcement

The next parameter investigated in this parametric study is the longitudinal reinforcement ratio. Because the Matlab code has been developed considering a symmetry of geometry and a symmetry of applied forces, the bottom longitudinal reinforcement ratio is always equal to the top one. Reinforcement ratios are taken from 0.5 % to 2.5 % with an increment step of 0.1 %. The effect is investigated for three different fibre volume ratios: 0 %, 1 % and 2 %. In order to focus mainly on the effect of fibres, no transverse reinforcement is considered in this study.

Results from the extended 3PKT analysis can be observed in Figure 67. It is clear from that figure that an increase of the longitudinal reinforcement ratio results in an increase of the ultimate shear strength of the coupling beam. The increasing tendency is almost linear and it has the same slope for the three fibre volume ratios considered in this study. The increase of fibre volume ratio also results in an increase of the total shear strength. It goes up by 33 % for a longitudinal reinforcement ratio of 0.5 % for 1 % of fibres as compared to the case without fibres and by 66 % for 2 % of fibres. However, this effect is slightly less significant for a higher longitudinal reinforcement ratio as the increase in shear strength for $\rho_l = 2.5\%$ is equal to 31 % for 1 % of fibres as compared to the case without fibres and 59 % for 2 % of fibres.

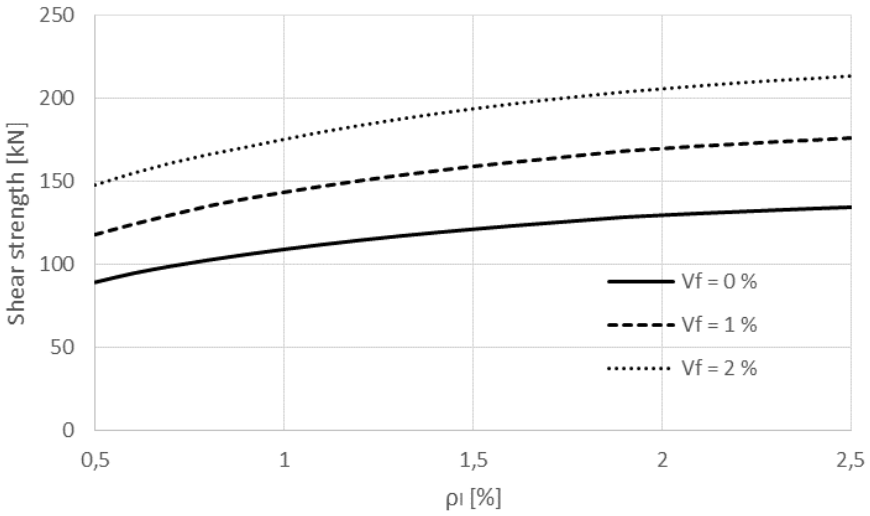

Figure 67: Effect of the longitudinal reinforcement ratio for different fibre volume ratios

The breakdown of this effect for a fibre volume ratio of 1 % is depicted in Figure 68. It can be seen that in this case, the fibres are not influenced by the longitudinal reinforcement. However, the critical loading zone and the dowel effect are both rather well influenced by this parameter. Concerning the dowel effect, higher reinforcement ratio leads to stiffer bars and therefore an increased effect of the dowels.

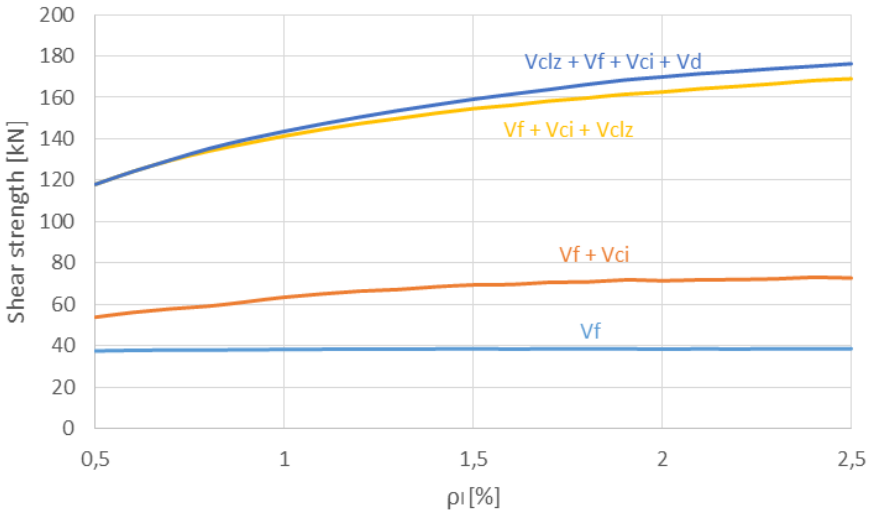

Figure 68: Breakdown of the effect of the longitudinal reinforcement ratio for $V_f = 1$ %

The effect of the CLZ is more complex as it is influenced by the top longitudinal reinforcement. Indeed, the increase of the shear resistance provided by the CLZ due to the increase in the longitudinal reinforcement can be explained by the softening effect. Figure 69 illustrates the effect of the longitudinal reinforcement ratio on the tensile strain in the top layer of steel reinforcement attained at peak resistance of the member. As the longitudinal reinforcement ratio increases, the strains in the top layer reinforcement are smaller for equivalent values of shear resistance. This leads to a decreased softening of the critical loading zone and therefore, concrete in this zone is able to withstand higher shear forces.

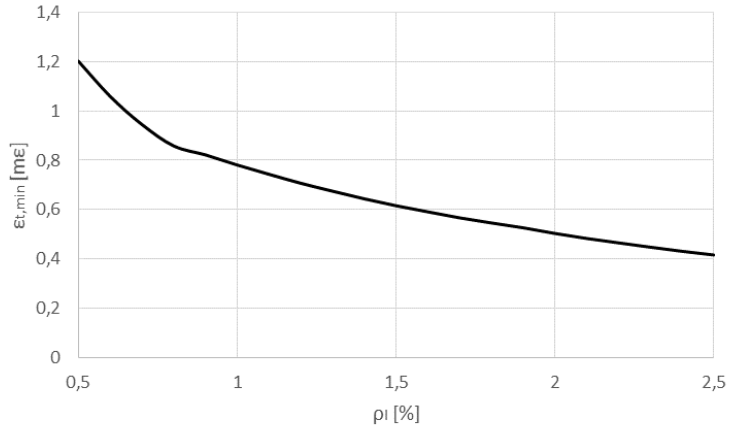

Figure 69: Effect of the longitudinal reinforcement ratio on the tensile strain in the top reinforcement at peak resistance

6.6.3 Fibre volume ratio

Next parameter investigated is the fibre volume ratio in the concrete matrix. It has been observed in the validation section that the fibre volume has an impact on the shear strength of coupling beams. However, a separate analysis is carried out to focus on the effect of the fibres. The shear resistance of the sample beam is tested for a fibre volume ratio ranging from 0 % to 2 % with an increment step of 0.1 %. Calculations are also performed for three different transverse reinforcement ratios: 0 %, 0.5 % and 1 %.

Figure 70 shows the shear strength provided by coupling beams with the above-mentioned properties. The horizontal axis represents the fibre volume ratio while the vertical axis represents the ultimate shear resistance of the members. Moreover, three different lines representing the three different transverse reinforcement ratios are depicted.

Figure 70 shows the results of the analysis. The vertical axis represents the shear strength of the members and the horizontal axis represents the fibre volume ratios. The three depicted lines represent the three different situations of transverse reinforcement. It can be seen that as the fibre volume ratio increases, the shear strength increases linearly regardless of the transverse reinforcement ratio. The increase of shear strength between fibre volume ratios of 0 % and 2 % are 60 % for $\rho_v = 0\%$, 33 % for $\rho_v = 0.5\%$, and 22 % for $\rho_v = 1\%$.

The transverse reinforcement adds a constant resisting component to the shear forces. The increase in strength from $\rho_v = 0\%$ to $\rho_v = 0.5\%$ is equal to about 105 kN which represents 91 % of the shear strength of a member without fibres and without transverse reinforcement. This increase of 105 kN represents 58 % of the shear strength for a member with 2 % of fibres and without transverse reinforcement. Similarly, the increase in strength from $\rho_v = 0\%$ to $\rho_v = 1\%$ is equal to about 220 kN which represents 191 % of the shear strength for a member without fibres and without shear reinforcement. This increase of 220 kN represents 122 % of the shear strength a member with 2 % of fibres and no transverse reinforcement.

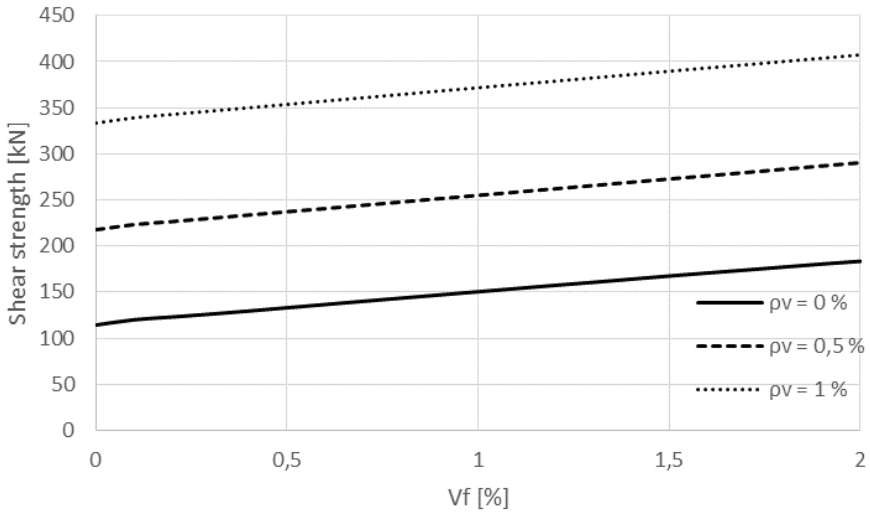

Figure 70: Effect of fibre volume ratio for different transverse reinforcement ratios

The breakdown of internal forces for the case with a transverse reinforcement ratio of 0.5 % is depicted in Figure 71. It can be seen that the only parameter affected by the inclusion of fibres is the contribution of the fibres in the shear strength which is linear. All other components are not affected by the inclusion of fibres and remain therefore constant. The contribution of stirrups however, remains more significant than the fibres for any fibre volume content.

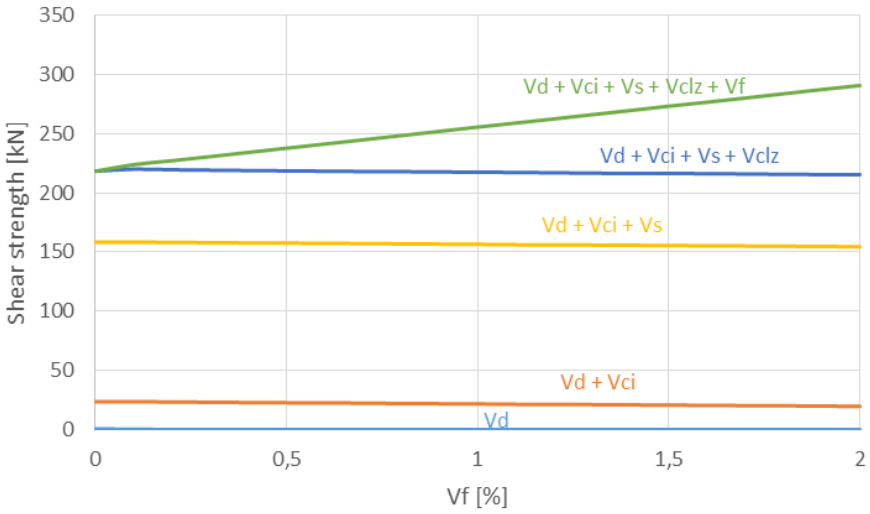

Figure 71: Breakdown of effect of fibre volume ratio for $\rho_v = 0.5\%$

6.6.4 Concrete compressive strength

The concrete compressive strength effect on the shear strength of coupling beams was investigated by Gaochuang et al. (2016) in their experiments. In this section, a sample beam with a compressive strength ranging from 35 MPa to 85 MPa is carried out. The increment step used for this analysis is equal to 5 MPa. In order to focus on the effect of the fibres, no transverse reinforcement is considered. Calculations are performed for three different fibre volume ratios: 0 %, 1 % and 2 %.

Figure 72 shows the effect of concrete compressive strength on the shear strength of the members for the three different volume of fibres considered here. It can be seen that an increasing f'_c leads to an increase in shear strength and that this effect is even more important when fibres are added into the mixture. Indeed, the increase in shear strength from $f'_c = 35\ MPa$ to $f'_c = 85\ MPa$ for a member without fibres is equal to 58 %, whereas it is about 54 % for 1 % or 2 % of fibres.

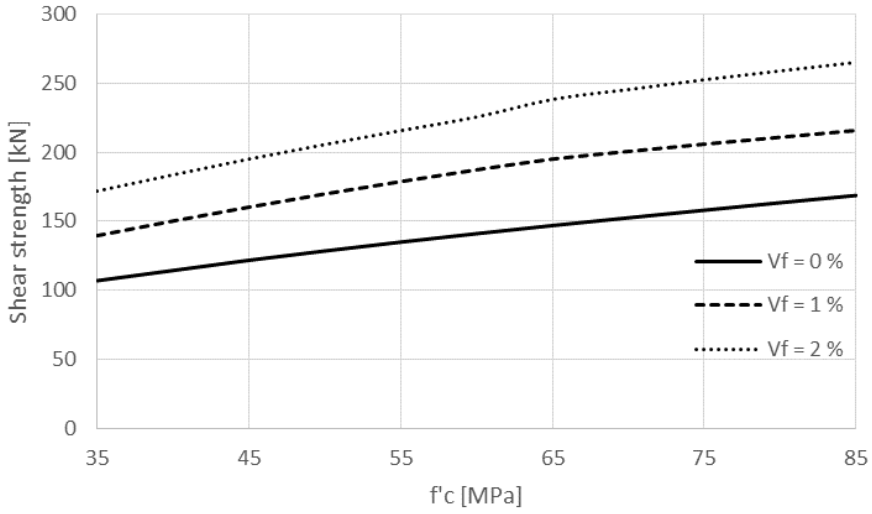

Figure 72: Effect of fibre volume ratio for different fibre volume ratios

The increase in shear strength attained with the inclusion of fibres for a coupling beam with a compressive strength of 35 MPa is equal to 31 % for a beam with 1 % of fibres compared to a beam without fibres and 61 % for 2 % of fibres compared to a beam with 0 % of fibres. This effect is less important for high strength concrete since in the case where $f'_c = 85\ MPa$, the increase in shear strength for a beam with 1 % of fibres compared to a beam without fibres is equal to 28 %, while for 2 % of fibres compared to 0 % of fibres, this increase is equal to 57 %.

Figure 73 shows a breakdown of all internal forces in coupling beams for a fibre volume ratio of 1 % and a compressive strength ranging from 35 MPa to 85 MPa. It can be seen that for an increasing concrete compressive strength, a slight increase of the contribution of fibres is observed. This is due to the bond between fibres and concrete which is enhanced by the use of higher strength concrete. Moreover, the main contribution of the resistance is the shear force provided by the CLZ which increases as f'_c increases as well. This can be easily explained as higher strength concrete is able to withstand higher stresses.

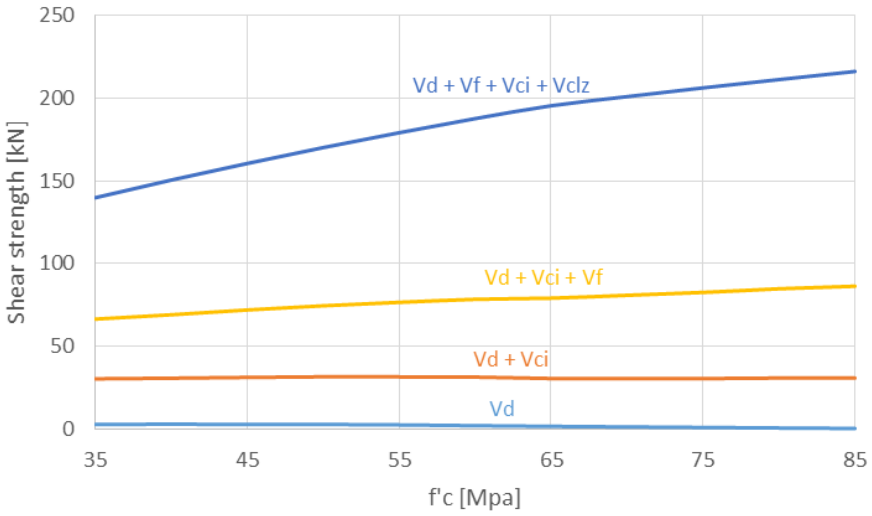

Figure 73: Breakdown of effect of concrete compressive strength for $V_f = 1\%$

6.6.5 Transverse reinforcement

As seen in the previous section, the transverse reinforcement is one of the main contributions to the shear strength of coupling beams. This parameter is analysed for three different fibre volume ratios: 0 %, 1 % and 2 %. The sample specimen tested in this section has a transverse reinforcement ratio ranging from 0 % to 1 % with an increment step of 0.1 %.

Figure 74 shows the results from the analysis where the horizontal axis represents the transverse reinforcement ratio and the vertical axis represents the shear strength of the coupling beams. The three lines depicted in the graph represent the three fibre volume ratios considered in this study. It can be observed that, regardless of the fibre volume ratio, the shear strength increases linearly with the same slope. This is similar to what had been found from the parametric study of the fibre volume ratio. The increase in shear strength from $\rho_v = 0\%$ to $\rho_v = 1\%$ is equal to 191 % for 0 % of fibres, 147 % for 1 % of fibres and 122 % for 2 % of fibres.

The effect of fibre inclusion results in a constant increase of strength. For members without fibres to members with 1 % of fibres, the increase is equal to about 37 kN which represents 32 % of the shear strength for the case with no transverse reinforcement and 11 % for the case with $\rho_v = 1\%$. Similarly, the increase in strength from 0 % of fibres to 2 % of fibres is equal to about 72 kN which represents 61 % of the shear strength for the case with no transverse reinforcement and 22 % for the case with $\rho_v = 1\%$. Even though the tendency of the curve is linear, it is not infinite as adding more transverse reinforcement increases the shear strength of the member until the member does not undergo a diagonal tension failure. If there is enough transverse reinforcement to avoid that type of failure, the type of failure becomes a sliding shear failure which the extended 3PKT model is not able to consider since it cannot take into account the yielding of longitudinal reinforcement which occurs in case of a sliding shear failure.

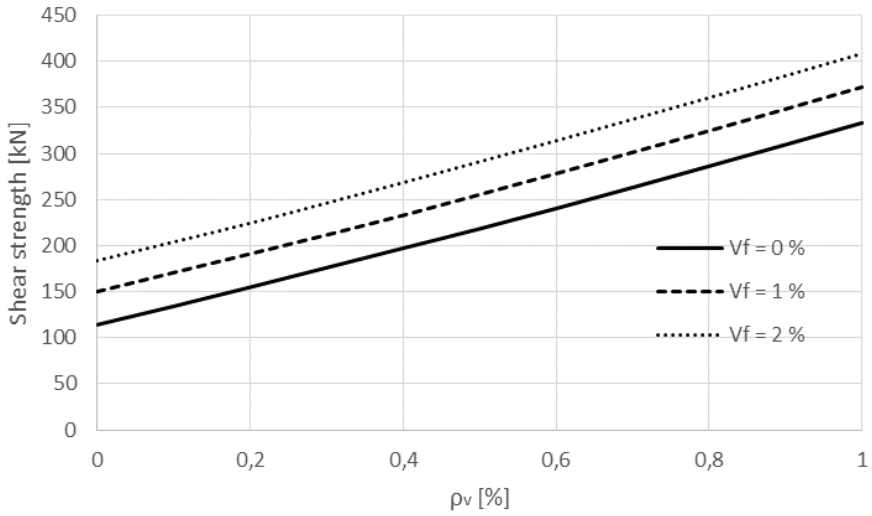

Figure 74: Effect of transverse reinforcement ratio for different fibre volume ratios

A breakdown of all internal forces is shown in Figure 75 for coupling beams with 1 % of fibres. It can be seen that the main contribution to the shear strength of coupling beams is the shear resistance provided by the stirrups which increases as the transverse reinforcement ratio increases, as expected. There is also a small linear decrease in shear provided by the CLZ but overall, the stirrups overcome this reduction of strength. This reduction of shear resistance provided by the CLZ with increasing transverse reinforcement ratio can be explained by the softening effect. Indeed, with more transverse reinforcement comes a more resistant member. Therefore, the bending moment increases and thus the strains in the longitudinal reinforcement are higher. This results in a more significant softening effect.

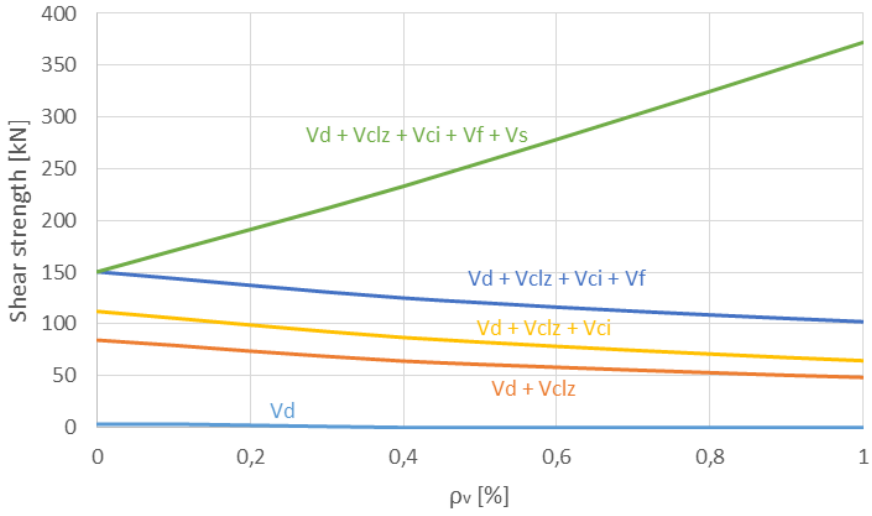

Figure 75: Breakdown of effect of transverse reinforcement ratio for $V_f = 1\%$

6.6.6 Size effect

The last parameter investigated is the size effect. The size effect is examined for a depth ranging from 350 mm to 1350 mm. In order to focus on the effect of fibres, no transverse reinforcement is considered in this study. Three different fibre volume ratios are analysed: 0 %, 1 % and 2 %. Figure 76 shows the results from the extended 3PKT analysis where the horizontal axis shows the depth and the vertical axis

shows the shear stress in the member. It can be observed that the three curves have a decreasing tendency for an increasing depth and that this tendency is slightly more important for a higher fibre volume ratio. Concerning the member with no fibre reinforcement, the decrease in strength between the minimum depth and the maximum depth is equal to 15 %. For 1 % of fibre reinforcement, the effect is slightly more significant and reaches 16.7 %, and it is equal to 17.3 % for 2 % of fibres. Thus, it can be concluded that the inclusion of fibres increases slightly the size effect.

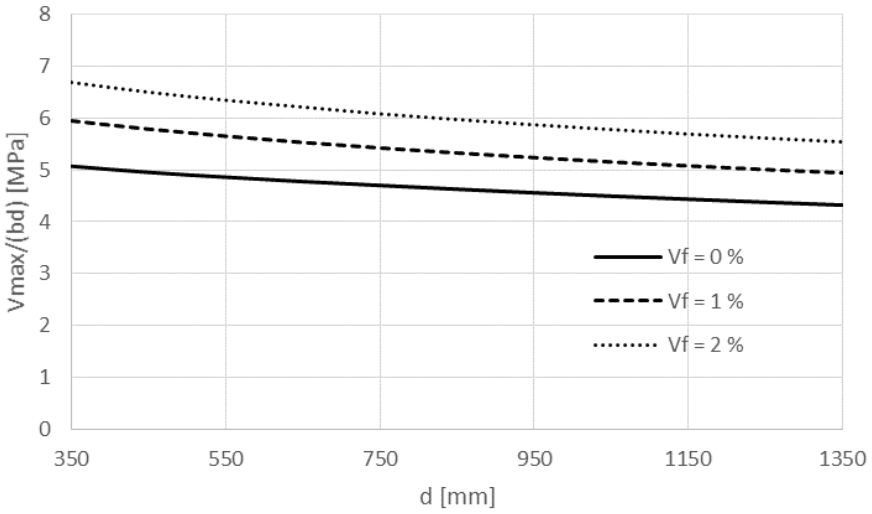

Figure 76: Size effect for different fibre volume ratios

Figure 77 represents a breakdown of the size effect for members with 0 % of fibres where all internal forces are shown. It can be seen that the decreasing tendency of shear resistance with increasing depth is due to the shear resistance provided by the aggregate interlock (V_{ci}). All other forces remain overall constant for all different depths. The decrease of V_{ci} with increasing d can be explained by the modification of the critical loading zone. Indeed, for a greater depth, the size of the member increases and so does the critical loading zone. Because of this effect, the transverse vertical displacement of the CLZ, Δ_c, increases as well. Since the crack width of the diagonal crack is mainly influenced by Δ_c, the crack width increases with the size of the member. However, the aggregate size remains the same and with a wider crack, the aggregate interlock contributes less to the shear resistance of the coupling beam.

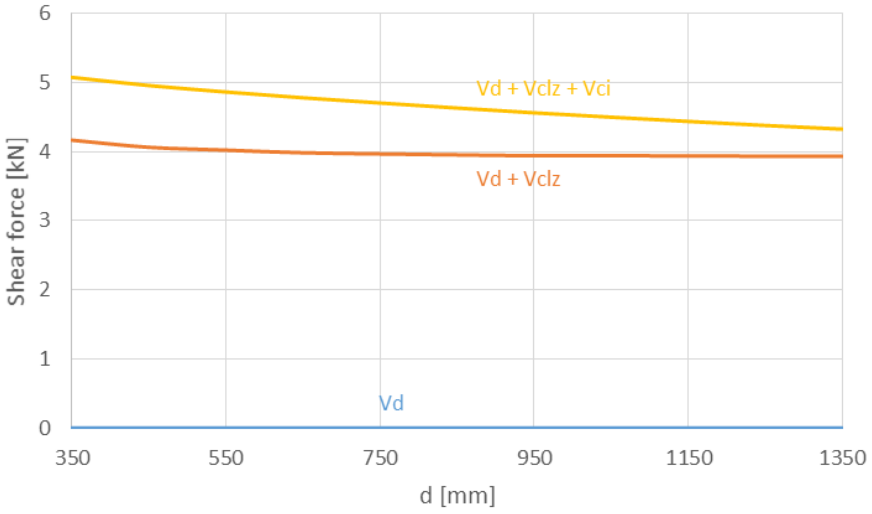

Figure 77: Size effect breakdown for 0 % fibre volume ratio

Since fibres are also influenced by this crack width, and that based on the SDEM, it was observed that after a critical crack opening, stresses in the fibers decreased, the addition of fibres results in an even more decreased shear resistance. However, because of the averaging of the crack, this effect is not very significant and thus, there is not a big difference between members with fibre inclusion and without fibre inclusion as it has been observed. This effect can be seen in Figure 78 which shows a breakdown of internal forces in the coupling beams with 1 % of fibres.

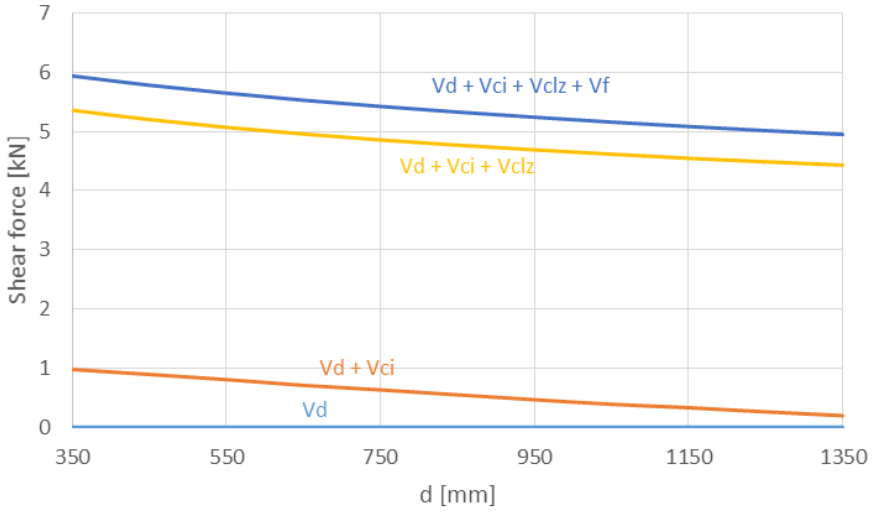

Figure 78: Size effect breakdown for 1 % fibre volume ratio

6.7 Discussion

Based on the results of the parametric study, several conclusions can be made. Concerning the span-to-depth ratio, it was observed that for increasing a/d, the shear strength decreased. This was caused mainly by the reduction of the size of the critical loading zone which proved to have a great impact on the shear strength of the members. The longitudinal reinforcement ratio was proved to have an impact on the shear strength as for increasing longitudinal reinforcement ratio, the shear strength increased. This effect was due to two effects which are the increase of the dowel effect and the reduced softening of the critical loading

zone. The effect of fibre volume ratio was also evaluated separately from transverse reinforcement. It was shown that fibres provided additional shear strength to the coupling beams and that for an increasing fibre content, this effect became more significant. The compressive strength of concrete also seemed to have an impact on the shear strength. It was shown that for increasing compressive strength, the shear strength of coupling beams also increased.

Transverse reinforcement was also studied. As expected, it was proved that for increasing transverse reinforcement ratio, the shear strength increased. In this study, the increasing tendency was linear regardless of the fibre content. Finally, the size effect was studied. It was concluded that for increasing size of members, the resistance was decreasing and that the addition of fibres slightly increased this effect.

7 Summary and conclusions

First, all data available on tests performed on fibre reinforced concrete coupling beams was selected. Based on a literature review, only one experimental study was found to match the selection criteria. This study was performed by Gaochuang et al. (2016). One additional study performed by Kuang and Baczkowski (2006, 2009) was selected even though it did not match one of the selection criteria in order to have more tests to analyse. All tests showed that the addition of fibres increased the shear resistance of coupling beams. Gaochuang et al. studied the effect of concrete compressive strength, span-to-depth ratio and fibre volume ratio on the shear strength of coupling beams. It was observed that for increasing fibre volume ratio, the shear strength increased as well. Same conlusions were drawn for the concrete compressive strength. Concerning the span-to-depth ratio, it was shown to decrease significantly the shear strength of coupling beams if the former increased. Kuang and Baczkowski studied another parameter which is the transverse reinforcement ratio. It was observed that the increase of transverse reinforcement ratio resulted in a great increase of the shear strength of coupling beams.

The main goal of the thesis was to propose an extension of the 3PKT model developed by Mihaylov et al. (2015). This model was able to predict the shear strength of conventional reinforced concrete deep beams under double curvature. By combining this model with the extended 2PKT for FRC proposed by Trvznikova (2017) which allowed to predict the full behaviour of simply supported fibre reinforced concrete deep beams, an extension for coupling beams was developed in this thesis. These two theories were described and analysed in detail.

The extension of the 3PKT model accounted for several parameters caused by the effect of the top layer of reinforcement which was not accounted for in the extended 2PKT for FRC, and the effect of fibres which is not accounted for in the original 3PKT. In order to consider the effect of the top layer of reinforcement into the extended 2PKT, equations from the 3PKT were used for the analysis of the critical loading zone which is a zone of the coupling beams subjected to high compression stresses and a softening of concrete due to the top layer of reinforcement. The effect of fibres in the 3PKT was implemented the same way as Tvrznikova (2017) did. However, a small modification was introduced. In the model by Tvrznikova, the crack width was considered to remain constant along the main diagonal crack which led to failure of the member. In the proposed model, an averaging of the crack width was proposed and analysed. Moreover, an additional extension of the model was proposed in order to account for the pull-out behaviour of the bars. This effect was introduced to optimise the deflections of the members. Finally, a simple idea was proposed to analyse members with axial restraint.

For comparison of results, another method was used to analyse fibre reinforced concrete coupling beams. This method was a finite element method analysis performed with the software VecTor2 developed at the university of Toronto (Canada). This program is capable of predicting the full behaviour of fibre reinforce concrete specimens. General assumptions were made in order to proceed to calculations. After testing, it was discovered that FEM results matched very well the results from the experimental study performed by Gaichuang et al. (2016) but it was time consuming.

The proposed extended 3PKT model was validated against the collected experimental data. The model showed excellent agreement regarding the shear strength of the tests specimens by Gaochuang et al.(2016). However, the third test series of their experiments was found to have a very low initial stiffness compared to the predicted results while all other tests' initial stiffness was accurately predicted. A possible explanation for such a difference was considered to be additional displacements that happened in the test setup during the experiments. This hypothesis was confirmed with the FEM analysis which predicted an initial stiffness very close to the one found from the extended 3PKT model. The validation process was performed for the three different test series and it was found that the average strength experimental-to-predicted ratio

was equal to 1.02 with a coefficient of variation of 5.29 %. Concerning FEM analysis, the an average experimental-to-predicted ratio of 0.99 and a coefficient of variation of 6.02 % were found. These results proved that the extended 3PKT model was able to provide as good results (or even better) as the a finite element method analysis for a smaller time of computation and modelling.

With the validated model, a parametric study was carried out to study the effect of span-to-depth ratio, longitudinal reinforcement, fibre volume ratio, concrete compressive strength, transverse reinforcement and size effect. As it was previously observed by Gaochuang et al. (2016), the proposed model showed that the shear strength decreased with increasing span-to-depth ratio. The longitudinal reinforcement ratio also had an impact on the shear strength as for increasing longitudinal reinforcement ratio, the shear strength was greater. Concerning the fibre volume ratio and concrete compressive strength, same conclusions as by Gaochuang et al. (2016) were drawn. Indeed, it was observed that for increasing fibre volume ratio and concrete strength, the shear strength of coupling beams increased. Transverse reinforcement was also analysed and it was found that an increase in transverse shear reinforcement resulted in a great increase in shear strength. Last parameter investigated was the size effect. This effect was studied for three different fibre volume ratios. It was found that the size effect was almost equal for any amount of fibres event though a slight increase of the size effect was observed with an increase in fibre volume ratio.

Finally, it should be stated that there are limitations to the proposed extended 3PKT model which should be considered for further research. The first limitation is the model considered for the estimation of tensile stresses in fibres calculated with the SDEM model which is not able to account for fibre rupture which could happen with low strength fibres. Moreover, there are some limitations on the model such as the rupture of the stirrups which is not considered here. This effect results in a more ductile post-peak behaviour as it can sometimes be observed from experiments. Moreover, the lack of experimental data did not allow an extensive validation of the model. For example, only three specimens were tested to study the effect of the span-to-depth ratio. Data from other authors should be used for more validation. However, results from this thesis are promising and the model proposes a more simple and faster alternative of analysis than a non-linear finite element method. Further research could study more adequately the effect of restraint or the use of ultra-high fibre reinforced concrete for coupling beams. The effect of sliding shear failure could also be studied and implemented in the model by accounting for the yielding of longitudinal reinforcement for members with heavy transverse reinforcement. An analysis of cost and performance could also be performed in order to compare FRC coupling beams with RC coupling beams and determine which solution suits better tomorrow's challenges.

References

ACI Committee 318, 2011. "Building Code Requirements for Structural Concrete (ACI 318-11) and Commentary", American Concrete Institute, Farmington Hills, MI, 503 pp.

ACI Committee 544, 1982. "Guide for Specifying, Proportioning, Mixing, Placing, and Finishing Steel Fiber Reinforced Concrete", *ACI Materials Journal*, Vol. 90, No. 1, pp. 94-101.

ACI Committee 318, 1999a. "Building code requirements for structural concrete (ACI 318-99)", Detroit.

ACI Committee 318, 1999b. "Commentary (ACI 318R-99)", Detroit.

Azizinamini, A., Stark, M., Roller, J., Ghosh, S., 1993. "Bond performance of reinforcing bars embedded in high-strength concrete", *ACI Structural Journal*, Vol. 90, No. 5, pp. 554-561.

Barbachyn, S., Kurama, Y. C., Novak, L. C., 2011. "Analytical Evaluation of Diagonally Reinforced Concrete Coupling Beams under Lateral Loads", *ACI Structural Journal*, Vol. 109, No. 4, pp. 497-508.

Bentur, A., Mindess, S., 1990. "Fibre Reinforced Cementitious Composites", *UK: Elsevier*.

Bentz, E. C., 2005. "Explaining the Riddle of Tension Stiffening Models for Shear Panel Experiments", *Journal of Structural Engineering*, ASCE, Vol. 131, No. 9, pp. 1422-1425.

Bischoff, P. H., 2003. "Tension Stiffening and Cracking of Steel Fiber-Reinforced Concrete", *Journal of Materials in Civil Engineering*, ASCE, Vol. 15, No. 2, pp. 174-182.

Casanova, P., Rossi, P., Schaller, I., 1997. "Can steel fibres replace transverse reinforcement in reinforced concrete beams?", *ACI Material Journal*, Vol. 94, pp. 341-354.

CEB-FIP Model Code 1990, 1993. "Design Code", Thomas Telford, London, 437 p.

Challal, O., Thobodeau, S., Lescelleur, J., Malenfant, P. 1996. "Steel fibre or conventional reinforcement for concrete shear walls", Concrete Institute, Vol. 18, No. 6, pp. 39-42.

CSA A23.3-04, 2004. "Design of Concrete Structures", *Canadian Standards Association*, Mississauga, ON, Canada, 214 p.

Deluce, J. R., Vecchio, F. J., 2013. "Cracking of SFRC Members Containing Conventional Reinforcement", *ACI Structural Journal*, Vol. 110, No. 3, pp. 481-490.

Di Prisco, M., Colombo, M., Dozio, D., 2013. "Fibre-reinforced concrete in fib Model Code 2010: principles, models and test validation", *Structural Concrete*, Vol. 14, No. 4, pp. 342-361.

European Committee for Standardization: EN 1992-1-1 Eurocode 2, 2004. "Design of Concrete Structures - Part 1-1: General Rules and Rules for Buildings", CEN, Brussels.

Franssen, R., 2016. "Kinematic Modelling of the Shear Behaviour of Coupling Beams in Wall Structures", *Master's Thesis* Faculty of Applied Sciences, University of Liège, Liège, Belgium, 61 p.

Gaochuang, C., Jun, Z., Degée, H., Vandoren, B., 2016. "Shear capacity of steel fibre reinforced concrete coupling beams using conventional reinforcements", *Engineering Structures*, Vol. 128, pp. 428-440.

Harajli, M. H., 2004. "Comparison of Bond Strength of Steel Bars in Normal and High-Strength Concrete", *Journal of Materials in Civil Engineering*, ASCE, Vol. 16, No. 4 pp. 365-374.

Harajli, M. H., Hout, M., Jalkh, W., 1995. "Local bond stress-slip relationship of reinforcing bars embedded in fiber reinforced concrete", *ACI Materials Journal*, Vol. 92, No. 4 pp. 343-354.

Jang, S.-K., Hong, S.-G., 2004. "Shear Strength Prediction for Reinforced Concrete Coupling Beams using Deformation Based Strut-and-Tie Models", *Architectural Research*, Architectural Institute of Korea, Vol. 6, No. 2, pp. 33-40.

Johnston, C. D., 2010. "Fiber-Reinforced Cements and Concretes", *Gordon and Breach Science Publishers*, Ottawa, Canada, 372 p.

Kuang, J. S., Baczkowski, B. J., 2006. "Shear capacity of steel fibre reinforced concrete coupling beams",International Conference on Computing and Decision Making in Civil and Building Engineering, Montréal, Canada, 2006.

Kuang, J. S., Baczkowski, B. J., 2009. "Steel-fibre-reinforced concrete coupling beams subjected to monotonic loading",*Magazine of Concrete Research*, Vol. 61, No. 1, pp. 35-41.

Lee, S.-C., Cho, J.-Y., Vecchio, F.J., 2011. "Diverse Embedment Model for Steel Fiber-Reinforced Concrete in Tension: Model Development", *ACI Materials Journal*, Vol. 108, No.5, pp. 516-525.

Lee, S.-C., Cho, J.-Y., Vecchio, F.J., 2011. "Diverse Embedment Model for Steel Fiber-Reinforced Concrete in Tension: Model Verification", *ACI Materials Journal*, Vol. 108, No.5, pp. 526-535.

Lee, S.-C., Cho, J.-Y., Vecchio, F.J., 2013. "Tension-Stiffening Model for Steel Fiber-Reinforced Concrete Containing Conventional Reinforcement", *ACI Structural Journal*, Vol. 110, No.4, pp. 403-412.

Lehman, D. E., Turgeon, J. A., Birely, A.C., Hart, C. R., Marley, K. P., Kuchma D. A., Lowes, L. N., 2013. "Seismic Behavior of a Modern Concrete Coupled Wall", *Journal of Structural Engineering*, Vol. 139, No. 8 pp. 1371-1381.

Lequesne, R. D., Parra-Montesinos, G. J., Wight, J. K., 2012. "Seismic behavior and detailing of high-performance fibre-reinforced concrete coupling beams and coupled wall systems", *Journal of Structural Engineering*, Vol. 139, No. 8, pp. 1362-1370.

Lim, T. Y., Paramasivam, P., Lee, S. L., 1987. "Analytical Model for Tensile Behavior of Steel-Fiber Concrete", *ACI Materials Journal*, Vol. 84, No. 4, pp. 286-298.

Mansur, M. A., Alwist, W. A. M., 1999. "Reinforced Fiber Concrete Deep Beams with Web Openings", *ACI Materials Journal*, Vol. 84, No. 4, pp. 286-298.

Matamoros, A. B., Wong, K. H., 2003. "Design of Simply Supported Deep Beams Using Strut-and-Tie Models", *ACI Structural Journal*, Vol. 100, No. 6, pp. 429-437.

Mihaylov, B. I., Bentz, E.C., Collins, M.P., 2010. "Two-Parameter Kinematic Theory for Shear Behavior of Deep Beams", *The International Journal of Cement Composites and Lightweight Concrete*, Vol. 6, No.4, pp. 263-271.

Mihaylov, B. I., Bentz, E.C., Collins, M.P., 2013. "Two-Parameter Kinematic Theory for Shear Behavior of Deep Beams", *ACI Structural Journal*, Vol. 110, No. 3, pp. 447-455.

Mihaylov, B. I., 2015. "Five-Spring Model for Complete Shear Behavior of Deep Beams", *Structural concrete*, Vol. 16, No. 1, pp. 71-83.

Mihaylov, B. I., Hunt, B., Bentz, E.C., Collins, M.P., 2015. "Three-Parameter Kinematic Theory for Shear Behavior of Continuous Deep Beams", *ACI Structural Journal*, Vol. 112, No. 1, pp. 47-57.

Mihaylov, B. I., Hannewald, P., Beyer, K., 2016. "Three-Parameter Kinematic Theory for Shear-Dominated Reinforced Concrete Walls", *Journal of Structural Engineering*, ASCE, Vol. 142, No. 7.

Naaman, A. E., Najm, H., 1991. "Bond-Slip Mechanisms of Steel Fibers in Concrete", *ACI Materials Journal*, Vol. 88, No. 2, pp. 135-145.

Newman, J., Choo, B. S., 2003. "Advanced Concrete Technology 3: Processes", *Elsevier Ltd.*, Oxford, Great Britain, 704 p.

Ou, Y.-C., Tsai, M.-S., Liu, K.-Y. 2012. "Compressive Behavior of Steel-Fiber-Reinforced Concrete with a High Reinforcing Index", *Journal of Materials in Civil Engineering*, ASCE, Vol. 24, No. 2, pp. 207-215.

Park, H., Eom, T., 2007. "Truss Model for Nonlinear Analysis of RC Members Subject to Cyclic Loading", *Journal of Structural Engineering*, Vol. 133, No. 10, pp. 1351-1363.

Paulay, T., Binney, J. R., 1974. "Diagonally reinforced coupling beams of shear walls", *Shear in Reinforced Concrete, ACI Special Publication SP42*, American Concrete Institute, Farmington Hills, Mich., pp. 579-598.

Popovics, S., 1970. "A Review of Stress-Strain Relationships for Concrete", *ACI Journal*, Vol. 67, No. 3, pp. 243-248.

Ramaswamy, A., Barzegar, F., Voyiadjis, G. Z., 1994. "Post-cracking Formulation for Analysis of RC Structures Based on Secant Stiffness", *Journal of Engineering Mechanics*, ASCE, Vol. 120, No. 12, pp. 2621-2640.

Sahoo, R. D., Maran, K., Kumar A., 2015. "Effect of steel and synthetic fibers on shear strength of RC beams without shear stirrups", *Construction and Building Materials*, 83, pp. 150-158.

Shah, D. U., Schubel, P. J., Licence, P., Clifford, M. J., 2012. "Determining the Minimum, Critical and Maximum Fiber Content for Twisted Yarn Reinforced Plant Fiber Composites", *Composites Science and Technology*, Vol. 72, No.15, pp. 1909-1917.

Shah, S. P., Rangan, B. V., 1971. "Fiber reinforced concrete properties", *ACI Journal*, Vol. 68, No.2, pp. 126-135.

Shiu, N. K., Barney, G. B., Fiorato, A. E., Corley, W.G. 1978. "Revering load tests of reinforced concrete coupling beams", Proceedings of the central american conference on earthquake engineering, El Salvador, pp. 239-49.

Susetyo, J., 2009. "Fiber Reinforcement for Shrinkage Crack Control in Pre-stressed, Precast Segmental Bridges", *Doctoral Thesis*, Department of Civil Engineering, University of Toronto, Toronto, ON, Canada, 307 p.

Tvrznikova, K., 2017. "Two-Parameter Kinematic Approach for the Shear Behavior of Deep Beams Made of Fibre-Reinforced Concrete", *Master's Thesis* Faculty of Applied Sciences, University of Liège, Liège, Belgium, 100 p.

Van Chanh, N., 2004. "Steel fiber reinforced concrete", Faculty of Civil Eng Ho Chi Min City, University of Technology, 108-16.

Vecchio, F. J., Collins, M. P. 1997. "The modified compression field theory for reinforced concrete elements subjected to shear", *ACI Journal*, Vol. 83, No. 2, pp. 219-231.

Voo, J. Y. L., Foster, S. J. 2003. "Variable Engagement Model for Fiber-Reinforced Concrete in Tension", *Uniciv Report No. R-420*, University of New South Wales, School of Civil and Environmental Engineering, 86 p.

Zollo, R. F., 1997. "Fiber-reinforced Concrete: An overview after 30 Years of Development", *Cement and Concrete Composites*, Vol. 19, pp. 107-122.

Appendix A: SDEM - Matlab Code

```
function [ff,feh,Keh,Kehi,ffavg,index]=SDEM(wj,fc,Vf,lf,lh,li,df)

wcr = [0:0.01:15];
taufmax = 0.396*sqrt(fc);
tauehmax = 0.429*sqrt(fc);

betaf = 0.67;
betaeh = 0.76;


 Kst =zeros(size(wcr));
 Keh =zeros(size(wcr));

sf = 0.01;
seh = 0.1;

Kehi = 1+(7*betaeh/15-1)*sqrt(seh/((lf-li)/2))-2*((sqrt((lf-li)/2))-sqrt(seh
    ))^2/(lf-li);

 for i=1:length(wcr)
    if wcr(i) < sf
        Kst(i) = betaf*wcr(i)/3/sf;
    else
        Kst(i) = 1-sqrt(sf/wcr(i))+betaf/3*sqrt(sf/wcr(i));
    end
 end

 for i=1:length(wcr)
    if wcr(i) < seh
        Keh(i) = betaeh*(2*wcr(i)/3/seh-1/5*(wcr(i)/seh)^2);
    elseif (wcr(i)>=seh && wcr(i)<(lf-li)/2)
        Keh(i) = 1+(7*betaeh/15-1)*sqrt(seh/wcr(i))-(2*(sqrt(wcr(i))-sqrt(
            seh))^2)/(lf-li);
    elseif (wcr(i)>=(lf-li)/2 && wcr(i) <li/2)
        Keh(i) = ((li-2*wcr(i))/(2*li-lf))^2*Kehi;
    else
        Keh(i) = 0;
    end
 end

alphaf = 0.5;

for i=1:length(wcr)
    fst(i) = alphaf*Vf*Kst(i)*taufmax*lf/df*(1-2*wcr(i)/lf)^2;
    if lh >= 1
        feh(i) = alphaf*Vf*Keh(i)*tauehmax*2*(li-2*wcr(i))/df;
    else
        feh(i) = 0;
```

```
    end
end

ff = feh+fst;
[c index] = min(abs(wcr-wj));

Om = 0;
for i=2:index
    Om = Om+(ff(i-1)+ff(i))*(wcr(i)-wcr(i-1))/2;
end

ffavg = Om/wj;

end
```

Appendix B: Pull-out - Matlab Code

```
function [D_bond,F_bond] = pullout(fc,lb,nb,db)

% Input
N = round(lb/db*2);
k1 = 1000;
Es = 2e5;

alpha = 0.3;
s1 = 1.5;
s2 = 3.5;
s3 = 10;
u1 = 2.57*sqrt(fc);
uf = 0.35*u1;

% Solution
dx = lb/N;
n = N+1;

As = nb*pi*db^2/4;
Abond = nb*pi*db*dx;

% Initialisation of the factors
Kel = zeros(n);
kel = Es*As/dx;

for i=2:n-1
    for j=2:n-1
        if i==j &&(i~=1 && i ~=n)
                Kel(i,j) = 2*kel;
                Kel(i+1,j) = -kel;
                Kel(i,j+1) = -kel;
        end
    end
end

Kel(1,1) = kel;
Kel(n,n) = kel;
Kel(1,2) = -kel;
Kel(2,1) = -kel;
Kel(n-1,n) = -kel;
Kel(n,n-1) = -kel;

% Calculation of the initial stiffness
kb0 = Abond*u1*(1/k1)^alpha/(s1/k1);
Kb0 = diag(ones(1,n)*kb0);
Kb0(1,1) = Kb0(1,1)/2;
Kb0(n,n) = Kb0(n,n)/2;
```

```
K0 = Kel + Kb0;
Kmax = K0(n,n)*10^6;
K0(n,n) = Kmax;

Kbj = Kb0;
Kj = K0;
Ft = zeros(n,1);
Dj = zeros(n,1);
Dt = 0:0.05:15;

for t=1:length(Dt)
    Ft(n,1) = Kmax*Dt(t);
    for j=1:100
        Dj = Kj\Ft;
        Kbj_prev = Kbj;

        for i=1:n
            if Dj(i) <= s1
                ri = u1*(Dj(i)/s1)^alpha;
            elseif Dj(i)>s1 && Dj(i) <= s2
                ri = u1;
            elseif Dj(i)>s2 && Dj(i) < s3
                ri = (u1-uf)/(s2-s3)*(Dj(i)-s2) + u1;
            else
                ri = uf;
            end

            if i==1 || i==n
                Ri = Abond/2*ri;
            else
                Ri = Abond*ri;
            end

            % Secant stiffness
            if Dj(i) > s1/k1
                Kbj(i,i) = Ri/Dj(i);
            end
        end

        errorj=100*sum(abs(diag(Kbj_prev)-diag(Kbj))./diag(Kbj));

        if errorj<0.01%
            break
        end

        % Update stiffness matrix
        Kj=Kel+Kbj;
        Kj(n,n) = Kmax;
    end
    Fr(:,t)=(Kel+Kbj)*Dj;
```

```
    D(t,1) = Dj(n);
    error(t,1)=errorj;
end
F_bond = Fr(n,:);
D_bond = D;
end
```

Appendix C: Extended 3PKT model - Matlab Code

```
clear all
clc
close all
%% Input
kci=0.18;
Dc=(0:0.1:30)';


prompt = {'Enter Beam name:','Show deformed shape? (y=yes/n=no)'};
dlg_title = 'Beam information';
num_lines = 1;
defaultans = {'CCB3402','n'};
answer = inputdlg(prompt,dlg_title,num_lines,defaultans);
BN = char(answer);
[fc, h, d, a, b, As, rs, sb, fy, Er, Vf, lf, lh, li, df, fyf, nb, db, ag, rv
    , fyv, Ev, VoP, Id, Vexp,PDfem, PDexp1] = BeamData(BN(1,:));

lb = 575;
[D_bond, F_bond] = pullout(fc,lb,nb,db);


for i=2:length(F_bond)
    if F_bond(i)<=F_bond(i-1)
        break
    end
end

F_bond = F_bond(1:i-1);
D_bond = D_bond(1:i-1);


%% Geometry
lb1e=0.11*sqrt(a^2+h^2);
alfa=atan(h/a);
alfa1=max(alfa,35*pi/180);

rl=100*As/b/d;
scr=0.28*db*2.5*(h-d)/(rl/100)/d;
l0=max(scr,1.5*(h-d)/tan(alfa1));
l0=min(l0,d/tan(alfa1)/2);
lk=l0+min(l0,d*(1/tan(alfa)-1/tan(alfa1)));
lt=d/tan(alfa1)+(lk-l0);

Av=min(rv/100,0.15*fc/fyv)*b*0.9*d/tan(alfa1);

Aceff=b*min(2.5*(h-d),h/2);

z=0.9*d;
```

```
m = 0.5;
if m>=0.3 && m<=0.6
    kclz=1;
else
    kclz = min(max(1-2*(cot(alfa)-2),0),1);
end

%% CLZ
[favg,Ec,Dcenv]=FAVG(Vf,lf,df,fc,alfa,lb1e);
favg(1)=0;
Vclzenv=favg*b*lb1e*sin(alfa)^2;
[Vclzmax, row]=max(Vclzenv);
Dcmax=Dcenv(row);
Kclz0=Vclzenv(2)/Dcenv(2);

%% Bottom reinforcement
kt=0.75;

%% Solution
LS=size(Dc,1);

kcj = zeros(LS,1);
S=0;
counter = 0;
for i=1:LS
    etl=0;
    etr=20/100;

    for j=1:100
        etj=(etl+etr)/2;
        etminj=kt*etj;
        etmaxj=(etj*lt-etminj*lk)/(lt-lk);
        Dtj=etj*lt/d*a;

        % CLZ
        if S==0
            eps1 = (1+1/tan(alfa)^2)*etminj;
            kc = min(1/(0.8+170*eps1),1);
        else
            kc = kcj(i);
        end
        Vclzj=interp1(Dcenv,Vclzenv*kc*kclz,Dc(i),'linear');

        % Stirrups
        evj=(Dc(i)+0.25*etj*d/(tan(alfa1))^2)/(0.5*z);
        fvj=min(Ev*evj,fyv);
        Vsj=Av*fvj;

        % Shear derived from moment equilibrium - flexural spring force
        [N]=TS_R_FRC_S(Aceff,Ec,etmaxj,ag,Vf,lf,df,db,sb,fc,nb,lh,li,Er,As);
```

```
        Vtj=N*z/(a*m);

        etminj=N/Er/As;

        % Dowel action
        fyej=fy*max((1-(Er*etminj/fy)^2),0);
        Vdj=min(12*Er*Id/lk^3*Dc(i),nb*fyej*db^3/3/lk);

        % Aggregate interlock
        sj=Dc(i)*sin(alfa1);
        wj=Dc(i)*cos(alfa1)+0.5*etminj*lk/sin(alfa1);
        [ncij,vcij]=CDMfunc(fc,ag,sj,wj);
        Vcij=kci*vcij*b*d;

        % Fiber action
        [ff,feh,Keh,Kehi,ffavg,index]=SDEM(wj,fc,Vf,lf,lh,li,df);
        beta=0;
        VFj=ffavg*b*d/sin(alfa1);

        % Shear resistance across diagonal crack
        Vccj=Vclzj+Vcij+Vsj+Vdj+VFj;

        % Error in equilibrium condition Vtj=Vccj
        erj=100*abs((Vtj-Vccj)/Vccj);
        if erj<0.01
            break
        end

        % Adjustment of boundaries for bisection method
        if Vtj<Vccj
            etl=etj;
        else
            etr=etj;
        end

    end

    er(i,1)=erj;
    V(i,1)=Vtj/1000;
    Vclz(i,1)=Vclzj/1000;
    VF(i,1)=VFj/1000;
    Vci(i,1)=Vcij/1000;
    Vs(i,1)=Vsj/1000;
    Vd(i,1)=Vdj/1000;
    Dt(i,1)=Dtj;
    w(i,1)=wj;
    s(i,1)=sj;
    et(i,1)=etj;
    vci(i,1)=vcij;
    nci(i,1)=ncij;
```

```
    Vcc(i,1)=Vccj/1000;
    etmin(i,1)=etminj;
    fib(i,1)=ffavg;
    Nx(i,1)=N;

    if Vtj<0;
        LS=i;
        break
    end

    kcj(i)=kc;
    if counter>=1
        if kcj(i)>kcj(i-1)
        kcj(i:end)=kcj(i-1);
        S=1;
        end
    end
    counter = counter+1;
end
etmax=et*(lt-kt*lk)/(lt-lk);
Dc=Dc(1:i);

F_pullout = zeros(LS,1);
D_pullout = zeros(LS,1);
alpha_p = zeros(LS,1);
lp = 0.8*d;
for i=1:LS
    [FF numel] = min(abs(F_bond-Nx(i,1)));
    F_pullout(i,1) = F_bond(numel)/1000;
    D_pullout(i,1) = D_bond(numel);
    alpha_p(i,1) = asin(D_bond(numel)/lp);
end

D=Dt+Dc;
[Vmax, rvmax]=max(V);
VFmax=VF(rvmax);
Vcimax=Vci(rvmax);
Vclzmax=Vclz(rvmax);
Vsmax=Vs(rvmax);
Vdmax=Vd(rvmax);
Dcu=Dc(rvmax);

% max error
max(abs(er))

%% Figures
D2 = [0; D];
V = [0; V];
D_pullout = [0;D_pullout];
Theta = D./a + alpha_p;
```

```
Theta2 = [0; Theta];

figure
plot(Theta,Vclz,'b')
hold on
plot(Theta,Vci,'r')
hold on
plot(Theta,VF,'m')
hold on
plot(Theta,Vs,'g')
hold on
plot(Theta,Vd,'c')
hold on
plot(Theta2,V,'k','Linewidth',2)
hold on
plot(PDexp1(:,1)./a,PDexp1(:,2),'-k','Color',[1 0.6 0],'LineWidth',2)
hold on
plot(PDfem(:,1)./a,PDfem(:,2),'-k','Color',[0.5 0 0.5],'LineWidth',2)
hold on
plot(Theta2,V-V+Vexp,'-k','Color',[0.7 0 0], 'LineWidth',2)
title('Shear behaviour of the coupling beam')
xlabel('\Theta [rad]')
ylabel('V [kN]')
legend('V_{clz}','V_{ci}','V_F','V_s','V_d','V','Exp','VecTor2')
xlim([0 Theta(end)])
print -r600 -dmeta -painters
```